

Confined Polymers in Biophysical Contexts

by

Kamal Tripathi

PHYS10201404006

The Institute of Mathematical Sciences, Chennai

A thesis submitted to the

Board of Studies in Physics

in partial fulfillment of requirements

for the Degree of

DOCTOR OF PHILOSOPHY

of

HOMI BHABHA NATIONAL INSTITUTE



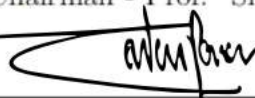
March, 2021


Homi Bhabha National Institute

Recommendations of the Viva Voce Board

As members of the Viva Voce Committee, we certify that we have read the dissertation prepared by Kamal Tripathi entitled "Confined Polymers in Biophysical Contexts" and recommend that it may be accepted as fulfilling the dissertation requirement for the Degree of Doctor of Philosophy.



Date: 08 July 2021
Chairman - Prof. Sitabhra Sinha


Date: 08 July 2021
Guide/Convener - Prof. Gautam I. Menon


Date: 08 July 2021
Co-guide - Prof. Satyavani Vemparala


Date: 08 July 2021
Examiner - Prof. Ranjith Padinhateeri (IIT Bombay, India)


Date: 08 July 2021
Member 1 - Prof. R. Shankar


Date: 08 July 2021
Member 2 - Prof. Shrihari Gopalakrishna


Date: 08 July 2021
Member 3 - Prof. Pinaki Chaudhuri

Final approval and acceptance of this dissertation is contingent upon the candidate's submission of the final copies of the dissertation to HBNI.

I hereby certify that I have read this thesis prepared under my direction and recommend that it may be accepted as fulfilling the thesis requirement.

Date: July 8 2021

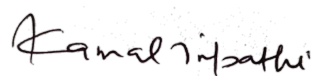
Place: IMSc, Chennai

 Co-guide
 Guide

STATEMENT BY AUTHOR

This dissertation has been submitted in partial fulfillment of requirements for an advanced degree at Homi Bhabha National Institute (HBNI) and is deposited in the Library to be made available to borrowers under rules of the HBNI.

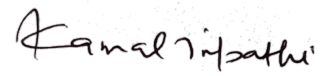
Brief quotations from this dissertation are allowable without special permission, provided that accurate acknowledgement of source is made. Requests for permission for extended quotation from, or reproduction of this manuscript in whole or in part, may be granted by the Competent Authority of HBNI when in his or her judgement the proposed use of the material is in the interests of scholarship. In all other instances, however, permission must be obtained from the author.



Kamal Tripathi

DECLARATION

I hereby declare that the investigation presented in the thesis has been carried out by me. The work is original and has not been submitted earlier as a whole or in part for a degree/diploma at this or any other Institution/University.



Kamal Tripathi

List of Publications arising from the thesis

Journal

1. **Chromatin Compaction, Auxeticity and the Epigenetic Landscape of Stem Cells**
Kamal Tripathi and Gautam I. Menon
[Physical Review X 9.4 \(2019\): 041020](#)
2. **Confined crowded polymers near attractive surfaces**
Kamal Tripathi, Gautam I. Menon and Satyavani Vemparala
[J. Chem. Phys. 151, 244901 \(2019\)](#)

In Preparation

1. **Diffusion in Crowded and Grafted Cylindrical Tube**
Kamal Tripathi, Gautam I. Menon and Satyavani Vemparala

Kamal Tripathi

List of presentation and participation in conferences

1. **2019 IMB Conference: Chromosome Territories & Nuclear Architecture**
IMB Mainz, October 2019 | **POSTER:** The auxetic phenotype in mouse embryonic stem cells exiting pluripotency
2. **Institute Seminar Day**
IMSc Chennai, March 2019 | **TALK:** Polymer Conformations in confined and crowded environment near attractive surfaces
3. **Mechano-Developmental Biology 2019**
Coorg, February 2019
4. **7th Indian Statistical Physics Community Meeting**
ICTS Bangalore, February 2019
5. **One day symposium on Soft Matter**
IIT Madras, January 2019
6. **Computational Biology Group Annual Talk**
IMSc Chennai, March 2018 | **TALK:** The auxetic phenotype in mouse embryonic stem cells exiting pluripotency
7. **6th Indian Statistical Physics Community Meeting**
ICTS Bangalore, February 2018
8. **Complex Fluids - CompFlu - 2017**
IIT Madras, December 2017
9. **VIIIth Bangalore School of Statistical Physics**
ICTS Bangalore, July 2017
10. **EMBO - Experimental and Theoretical approaches to cell mechanics**
RRI and NCBS Bangalore, April 2017
11. **Complex Fluids - CompFlu - 2016**
IIIT Hyderabad, December 2016
12. **VIIth Bangalore School of Statistical Physics**
ICTS Bangalore, July 2016

To my beloved mother

Acknowledgements

The success and final outcome of this thesis required a lot of guidance, assistance and motivation from many people and I am extremely fortunate that I got these throughout my Ph.D. duration. Firstly, I would like to express my sincere gratitude to my advisor Prof. Gautam I. Menon and co-advisor Prof. Satyavani Vemparala for their continuous support and for establishing an excellent research environment at IMSc. Both my advisors motivated me through their vast experience, immense knowledge, and patience in such a way that in future I can work as an independent researcher. Their consistent guidance helped me throughout my research and right up to the writing of this thesis.

I would like to thank the rest of my doctoral committee members: Prof. Sitabhra Sinha, Prof. R. Shankar, Prof. Shrihari Gopalakrishna and Prof. Pinaki Chaudhuri, for their insightful comments and encouragement which enabled me to widen my research perspectives. I would also like to thank my thesis examiners Prof. Ranjith Padinhateeri and Prof. Aparna Baskaran for their comments so that the thesis can be viewed in this current form. This acknowledgment would not be complete without thanking all my friends, especially, Dhruba for her continuous support throughout my Ph.D.

Contents

Synopsis	v
List of Figures	xvii
List of Tables	xxv
1 Introduction	1
1.1 Polymer Models	2
1.2 Flexible Polymer	3
1.2.1 The ideal chain on a lattice	3
1.2.2 The Gaussian Chain Model	6
1.3 Semi-flexible Polymers	7
1.3.1 Worm-like Chain	7
1.4 Non-ideal Chains	10
1.4.1 The Self-avoiding Chain	10
1.4.2 Flory Theory	10
1.5 Polymers in Solvent: Flory-Huggins Mean-field Theory	12
1.5.1 Effect of Solvent Quality	16
1.6 Polymers Under Confinement	16
1.6.1 Analytical Approach to Confinement	17
1.6.2 Scaling Approach to Confinement	19
1.6.3 Thermodynamic Approach to Confinement	20
1.7 The Stem Cell	22
1.8 Summary	24

2	Methods	27
2.1	Molecular Dynamics: The Basic Idea	27
2.1.1	Force Field and Equations of Motion	28
2.1.2	Bonded Interaction	29
2.1.3	Non-Bonded Interaction	30
2.1.4	Solution of Equation of Motion	32
2.2	Ensembles	35
2.3	Thermostats and Barostats	36
2.4	Ergodic Hypothesis	40
2.5	All Atom vs Coarse Grained Model	40
2.6	Software Packages	41
3	Chromatin Compaction, Auxeticity and the Epigenetic Landscape of Stem Cells	43
3.1	Introduction	43
3.2	Materials and Methods	48
3.2.1	Model Description	49
3.2.2	Derivation of model equations: R equation	51
3.2.3	Derivation of model equations: Ψ equation	53
3.2.4	Estimation of parameters	54
3.2.5	Mapping to the experimental system	55
3.2.6	Numerical simulations	56
3.3	Results	56
3.3.1	Auxetic and normal mechanical behaviour in a model description of nuclear indentation	56
3.3.2	Describing nuclear shape changes in micro-channel flow	58
3.3.3	Autocorrelations and cross-correlations of chromatin compaction and nuclear dimensions in the auxetic regime	61
3.3.4	Correlations across the auxetic-nonauxetic boundary as probes of the transition	64
3.3.5	Physical argument for the transition between auxetic and non-auxetic behaviour	66

3.3.6	Inferring $V(\delta\Psi)$ from experimental data	68
3.4	Discussion	71
3.5	Conclusions	74
4	Crowding and Confinement influence polymer conformations and single particle diffusion	77
4.1	Confined Crowded Polymers near Attractive Surfaces	78
4.1.1	Methods	82
4.1.2	Results	86
4.1.3	Discussion and Conclusion	101
4.2	Diffusion in Crowded and Grafted Cylindrical Tube	105
4.2.1	Methods	106
4.2.2	Results	109
4.2.3	Discussion and Conclusion	114
5	Conclusion	117
	Appendix	123
A.1	Exact solution of the anisotropic case for a harmonic epigenetic potential in the absence of noise	123
A.2	Correlation functions for the case of a harmonic chromatin compaction potential	125
A.3	Long time behaviour of cross-correlation functions	128
A.4	Periodic Force	130
	Bibliography	133

SYNOPSIS

Polymers are long molecules, composed of smaller units called monomers. From plastics to coatings, many kinds of synthetic polymers are used in everyday life. A large number of biological polymers are constituents of the cells and tissues which make up living organisms [[Phillips et al., 2012](#), [Boal and Boal, 2012](#)].

A number of experimental situations involve understanding the reduction of polymer entropy due to confinement and unusual phase behaviour that can arise as a consequence. For example, DNA in living cells is a polymer confined within a nucleus and a number of biological macromolecules are wrapped in a membrane prior to being transported to their destination [[Alberts et al., 2013](#)]. Chromatin, the term describing DNA complexed with packaging proteins in living cells, is folded and compacted on several length scales and the modulation of this folding by biophysical and biochemical processes controls DNA accessibility [[Van Holde and Zlatanova, 1996](#), [Butler and Crothers, 1983](#)]. The term euchromatin refers to a more loosely packed, gene-rich region of DNA while heterochromatin is more tightly packed and typically gene-poor [[Alberts et al., 2013](#)].

This thesis studies aspects of the behaviour of polymers under confinement. It describes three problems: the first concerns a novel mechanical property of the mouse embryonic stem cell nucleus exiting pluripotency, the property of auxeticity. This is studied using a combined biophysical and dynamical systems approach. The second describes a general computational approach to understanding confined polymers.

Here, tuning both the interaction of the polymer with the walls of the confinement and the density of crowder particles provides a way of altering polymer conformations within the confining region. This is studied using large-scale coarse-grained molecular dynamics simulations. In the third problem, using the coarse-grained molecular dynamics simulation, diffusive behaviour of a particle in a cylinder with its inner surface grafted with polymers is studied.

This thesis is comprised of 5 chapters. In Chapter 1, the Introduction, we describe the necessary theoretical background and terminology required to describe the results presented in this thesis. We discuss different polymer models and the properties of polymers in solution and also summarize arguments concerning the behaviour of polymers under confinement. Chapter 2 describes the basic principles and techniques of molecular dynamics simulations. Chapter 3 illustrates how the observation of auxeticity in mouse embryonic stem cells can be modelled. It extends the predictions of the theoretical framework to Waddington's ideas concerning the epigenetic landscape in stem cells. In Chapter 4, we present results from the simulation of a long polymer chain and crowder particles under confinement with different wall interactions and solvent quality. It also presents the results from large-scale coarse-grained molecular dynamics simulations of a particle in a infinitely long cylinder with its inner surface grafted with polymers. Finally, Chapter 5 provides conclusions from this thesis and perspectives for future work.

Auxetic phenotype in mouse embryonic stem cell nuclei

Stem cells are cells that can both self-renew as well as differentiate into specific cell types upon receiving specific biochemical and mechanical cues [Alberts et al., 2013]. Cells which can differentiate into multiple cell types are *pluripotent* stem cells. The biophysical properties of stem cells are very different from those of differentiated cells. Experiments [Talwar et al., 2013] show that embryonic stem (ES) cells show

larger nuclear area fluctuations as compared to differentiated fibroblasts. ES cells have more open and fluid chromatin, also exhibiting hyperdynamic binding and unbinding [Meshorer et al., 2006] of histone proteins [Efroni et al., 2008]. The differentiation of ES cells into various lineages results in stiffer nuclei and condensed chromatin.

ES cells lack specific structural proteins that border the nuclear envelope, leading to softer nuclei that are more sensitive to internal chromatin dynamics. The dynamics of chromatin thus plays a more significant role in controlling the rheological properties of the nucleus, and thus nuclear mechanics, in ESCs. Generally, materials have a positive Poisson's ratio i.e., if we stretch/compress the material, it shrinks/elongates in the other two perpendicular dimensions. However, there are some materials which elongate/shrink upon stretching/compressing them. These materials are called auxetic. Recent experiments [Pagliara et al., 2014] show that the nucleus of mouse embryonic stem cells, en-route to differentiation, exhibit auxetic behavior i.e., they have a negative Poisson's ratio. In the intermediate transition state, the cross-sectional nuclear area of stem cells becomes 5 – 10% smaller when compressed by $2\mu m$. In a similar experiment performed on naive pluripotent stem cells, as well as on differentiated stem cells, the nuclear area expands, indicating a positive Poisson's ratio.

The model [Tripathi and Menon, 2019] we develop explains this phenomenon as well as provides a broader biophysical perspective. It assumes that the nucleus is compressible and that the chromatin in the nucleus can be described as an active polymeric fluid. The response of the nucleus to the uniaxial external force is assumed to be anisotropic. We show that auxeticity arises from the coupling of a variable describing chromatin compaction with variables describing nuclear dimensions.

The variables entering the model are the chromatin compaction variable Ψ , governed by the fraction of bound histones, as well as the nuclear dimensions parallel R_{\parallel} and

perpendicular R_{\perp} to the external applied force f . We derive a de-dimensionalized, coupled, dynamical system for the variables $\delta\Psi$, δR_{\parallel} and δR_{\perp} and use it to derive the principal results summarized below.

Results

- The mechanical behaviour of the nucleus depends upon a parameter B that represents the lowest order coupling between chromatin compaction and nuclear dimensions. For $B < 0$, the system shows auxetic behavior while for $B > 0$, the system behaves as a conventional material with a positive Poisson's ratio (see Figure S.1).

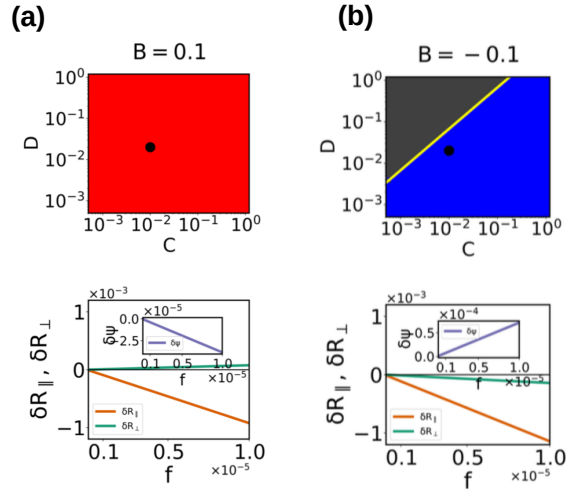


Figure S.1: The mechanical behaviour of dynamical variables of the model with the force for (a) positive parameter B (b) for negative B . C and D are the other parameters of the model. Red and blue show the regions where a stable solution is obtained (red = normal, blue = auxetic), while grey shows where solutions become unstable.

- The auxetic-nonauxetic boundary must be crossed twice as ES cells transit the transitional state as they differentiate. We propose that one useful way of monitoring this is to study the behavior of specific time correlation functions. In Figure S.2, the $\langle \delta R_{\perp}(0)\delta\Psi(t) \rangle$ changes the sign of its slope when the parameter B changes sign. This change of sign can be used to determine the

transition state between the stem cell and differentiated prime.

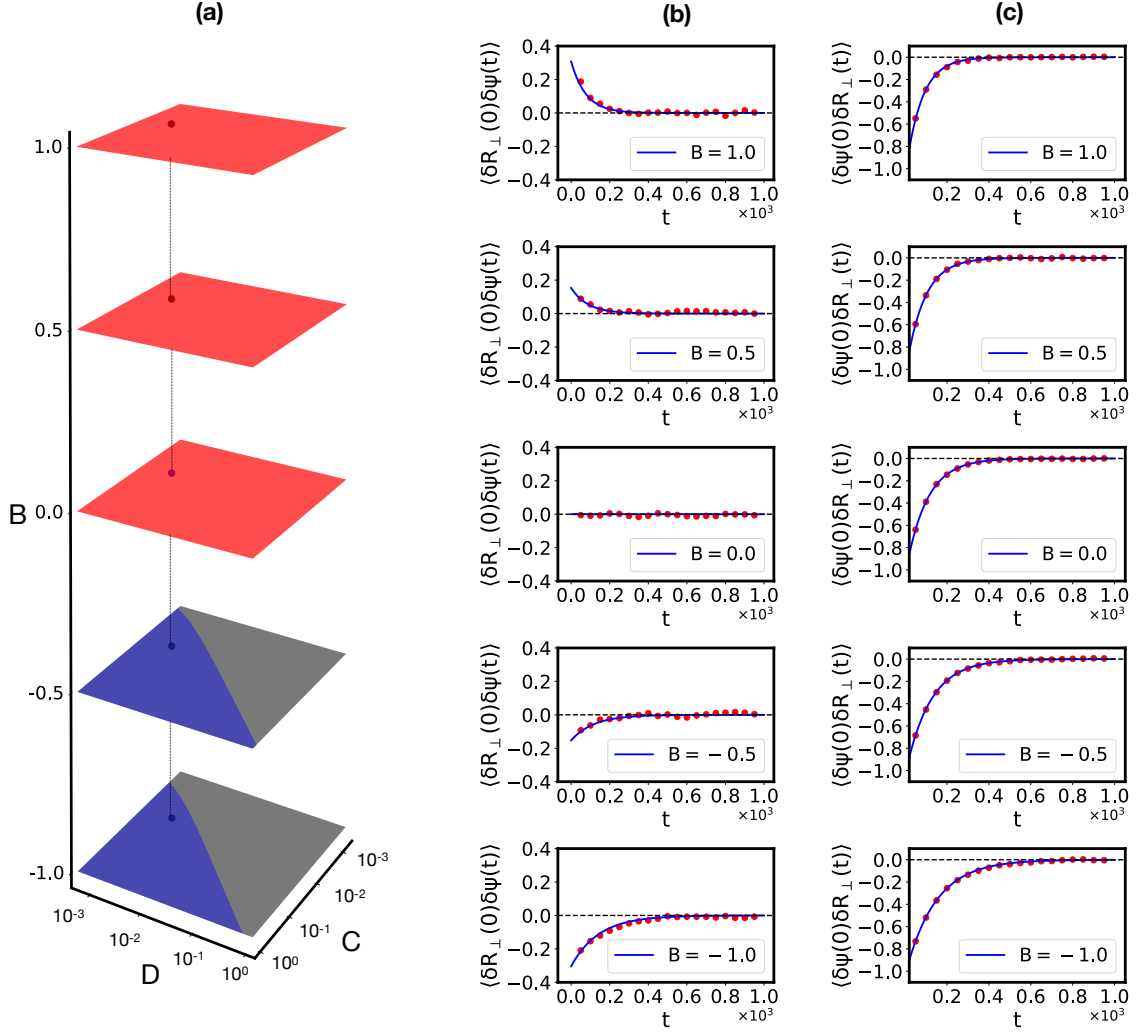


Figure S.2: (a) Choice of parameters in (B,C,D) parameter space, B showing on vertical axis (B,C and D are the parameters appearing in the model). Column (b) and (c) show the correlation functions $\langle \delta R_{\perp}(0) \delta \Psi(t) \rangle$ and $\langle \delta \Psi(0) \delta R_{\perp}(t) \rangle$ respectively.

- Our model describes the dynamics of the chromatin compaction variable Ψ . This fluctuates about a constant value but is constrained by a chromatin compaction potential $V(\delta\Psi)$. Different minima of this compaction potential $V(\delta\Psi)$ reflect the local stability of different compaction states of chromatin. It is known that one distinction between different classes of cell types arises from their different levels of chromatin compaction. Waddington originally described cell differentiation in terms of a ball rolling down a slope to different valleys at the bottom, using the idea of an epigenetic landscape [Wadding-

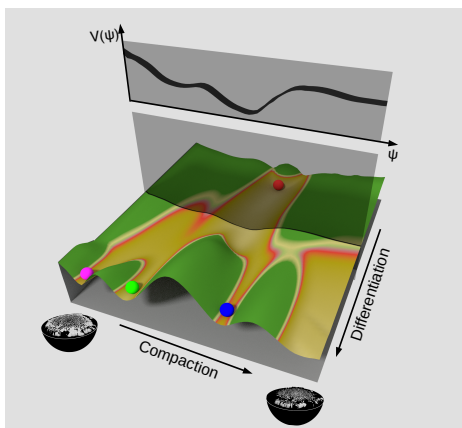


Figure S.3: A pictorial representation of epigenetic landscape, projected onto a single compaction variable Ψ .

ton, 1947]. The biophysical interpretation of this landscape been unclear. We suggest that projecting the complex spatial-temporal distribution of chromatin compaction in cells onto an overall compaction variable Ψ (see Figure S.3) provides a specific way of connecting the landscape picture to our mathematical formulation. Thus, we interpret the time dependence of Ψ in terms of motion in a one dimensional potential described through our equations, as shown in the figure. This approach provides specific biophysical insights into the epigenetic landscape, also suggesting how it might be experimentally probed in coarse-grained biophysical measurements.

Conformations of crowded polymers under confinement within interactive surfaces

The shape of the polymer depends upon factors such as solvent condition, presence of other particles, concentrations, temperature etc. [de Gennes, 1979, Doi, 1996]. Biological polymers, in addition to being confined, are also crowded. For example, within the cell, the heterogenous mixture of proteins, organelles, water and different ions can lead to the loss of conformational entropy, yielding effects which are hard to predict. The degree of confinement, as well as the presence of crowders, affects

the conformation and other properties of the polymer. The interaction of polymers with surfaces has relevance in applications such as the coating of surfaces, aspects of interfacial macromolecular recognition, adhesion, wetting, etc. [Ionov et al., 2010, Haraguchi et al., 2014].

We study the conformations of the polymer under crowded and confined conditions [Tripathi et al., 2019]. Conformations of the polymer are expected to depend upon the interplay between monomer-monomer interactions, monomer-surface interactions and the degree of confinement. Earlier studies [Bachmann and Janke, 2005, Arkin and Janke, 2012b] have shown that, in the absence of crowder particles, the polymer assumes four main phases depending upon these factors: these are desorbed extended (DE), desorbed collapsed (DC), adsorbed extended (AE) and adsorbed collapsed (AC) phases. In this study, we take this problem one step further, adding a new dimension of crowder density to the problem which makes it closer to a real scenario.

We simulate a coarse-grained model of a 400-monomer-long neutral polymer and crowder particles in spherical confinement. The size of the monomers and the crowder particles are kept the same for simplicity. To understand the effect of crowder density, the number of crowder particles N_c is changed such that the crowder density (ϕ_c) of the system varies from 0.035 to 0.435, where ϕ_c is defined as $\phi_c = N_c v_c / V$, $v_c = \frac{4}{3} \pi r_c^3$, r_c is the radius of the crowder particle, V is the volume of the confinement region. The solvent quality is implemented by an implicit solvent condition.

A pair of non-bonded particles interact via a Weeks-Chandler-Andersen potential which is a truncated and shifted Lennard-Jones (LJ) potential with a cutoff. The bonded monomers interact via a harmonic spring potential. The interaction of the wall with the monomers as well as the crows is given by the LJ potential. The cutoff for LJ interaction, in this case, depends upon whether the polymer is attracted or repelled from the confining wall.

Results

- To understand the effect of confinement, we simulated the polymer under confinement with good solvent parameters along with the crowder particles and compared the results with the simulation of polymer under periodic boundary condition keeping the other parameters same. The polymer assumes a desorbed extended conformation in both the cases, however, the radius of gyration R_g is significantly smaller in case of confinement compared to that in the unconfined case.
- Further, to understand the role of crowder density ϕ_c on the conformation of the polymer, simulations of a polymer in both good and poor solvent conditions are performed with different numbers of crowder particles. In Figure S.4 (c) and (d), it can be seen that in the case of a good solvent, the polymer is adsorbed almost completely onto the wall and varying the crowder density does not make any difference to the conformation of the polymer. However, for a poor solvent, the polymer makes a transition from an open conformation to a collapsed one for moderate values of ϵ_{mw} . Increasing the number of crowder particles compacts the polymer, reflecting in the order parameter q which represents the average number of neighbours for a monomer (see Figure S.4).
- In order to understand the effect of monomer-wall interaction strength ϵ_{mw} , we simulated the polymer in a good solvent condition under confinement with different ϵ_{mw} . It is observed that the polymer gets adsorbed onto the confining surface. The degree of adsorption depends upon the attractive wall strength. The higher the attractive wall strength, the larger the number of monomers that re adsorbed onto the surface. However, in poor solvent conditions, there is a transition from an adsorbed collapsed conformation to an adsorbed extended state as we increase ϵ_{mw} . Increasing the number of crowder particles, however, further changes the conformation of the polymer. The monomers tend to take

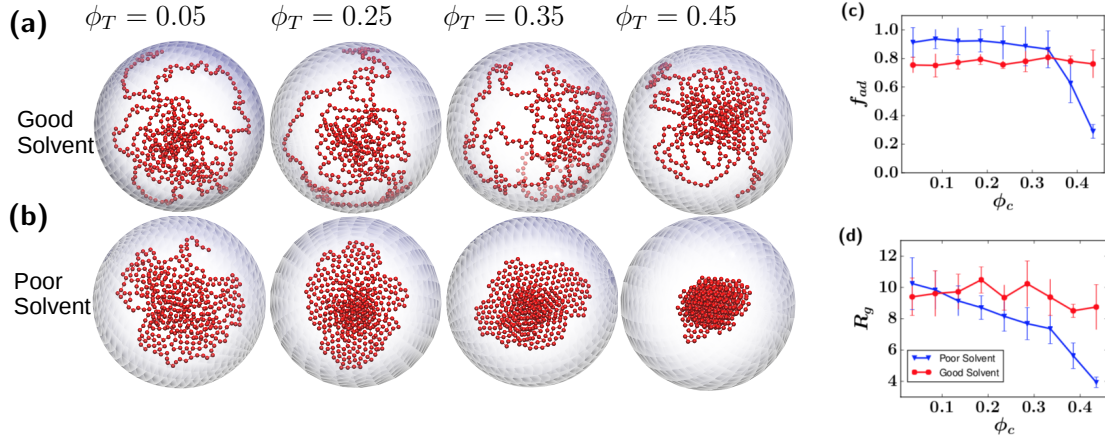


Figure S.4: The snapshots of polymer for (a) good solvent condition, (b) poor solvent condition for different ϕ_c values for fixed $\epsilon_{mw} = 10.0$, (c) the fraction of adsorbed monomers (f_{ad}) and (d) R_g as a function of ϕ_c .

a more structured form for higher ϕ_c values (see Figure S.5).

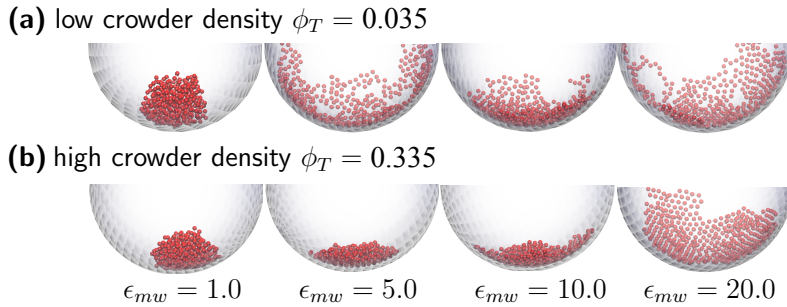


Figure S.5: The snapshots of the polymer for (a) low crowder density $\phi_c = 0.035$ and for (b) high density $\phi_c = 0.335$ for different wall attractive strengths.

Our results show that the problem of polymer confinement changes significantly when the additional parameter of crowder density ϕ_c is added to it. ϕ_c plays an important role in changing the conformations significantly, while the addition of crowder particles adds an additional level of biological realism.

Diffusion in Crowded and Grafted Cylindrical Tube

The diffusion of molecules in confined compartments is an important phenomenon in many biological processes. In this third problem, results from large-scale molecular dynamics simulations of a particle in an infinitely long cylinder grafted with neutral polymers are presented. Additionally, crowding agents are added to the system, and we study the diffusivity of the particle and conformations of the polymers as a function of the confining potential, solvent quality and the density of crowders.

We simulate a particle confined in an infinitely long cylinder of radius 20 units which has its inner surface grafted with 20-monomer-long neutral polymers. The size of the tracer particle, monomers and the crowder particles are kept the same, for simplicity. To understand the effect of crowder density, the number of crowder particles N_c is added such that the crowder density (ϕ_c) of the system varies from 0.035 to 0.435, where ϕ_c is defined as $\phi_c = N_c v_c / V$, $v_c = \frac{4}{3}\pi r_c^3$, r_c is the radius of the crowder particle, V is the volume of the confinement region. The solvent quality is implemented by an implicit solvent condition. A pair of non-bonded particles interact via a WCA potential. The bonded monomers interact via a harmonic potential. The interaction of the wall with the monomers as well as the crowders is given by the LJ potential. The cutoff for LJ interaction, in this case, depends upon whether the polymer is attracted or repelled from the confining wall.

Results

- In good solvent conditions, the radius of gyration R_g decreases with the crowder density ϕ_c for attractive as well as repulsive wall cases. In case of poor solvent conditions, the radius of gyration of the graft polymers does not change significantly with the crowder density except for the highest density case.

- For both solvent conditions and different monomer-wall interactions, as the crowder density increases, the behaviour of the particle shifts from super-diffusive behaviour to normal Brownian motion.
- The distribution of crowder particles is uniform near the axis of the cylinder, while near the wall of the cylinder, these particles form layered structures across a range of solvent conditions and different monomer-wall interactions. On the other hand, the monomers are adsorbed to the wall in a layered fashion under poor solvent conditions with the degree of adsorption and the number of layers depending upon the monomer-wall interaction. In good solvent conditions, the polymers tend to assume an extended structure for repulsive walls while they adsorb to the cylindrical wall and form a layered structure for high attractive interaction.

We studied the diffusion of tracer particle in a cylindrical geometry with walls coated by polymers. We concluded that tracer particles in such a geometry were slowed down as more crowder particles were introduced to the cylindrical confinement. This slow down occurs regardless of solvent condition and wall interaction.

List of Figures

S.1	The mechanical behaviour of dynamical variables of the model with the force for (a) positive parameter B (b) for negative B . C and D are the other parameters of the model. Red and blue show the regions where a stable solution is obtained (red = normal, blue = auxetic), while grey shows where solutions become unstable.	viii
S.2	(a) Choice of parameters in (B,C,D) parameter space, B showing on vertical axis (B,C and D are the parameters appearing in the model). Column (b) and (c) show the correlation functions $\langle \delta R_{\perp}(0)\delta\Psi(t) \rangle$ and $\langle \delta\Psi(0)\delta R_{\perp}(t) \rangle$ respectively.	ix
S.3	A pictorial representation of epigenetic landscape, projected onto a single compaction variable Ψ	x
S.4	The snapshots of polymer for (a) good solvent condition, (b) poor solvent condition for different ϕ_c values for fixed $\epsilon_{mw} = 10.0$, (c) the fraction of adsorbed monomers (f_{ad}) and (d) R_g as a function of ϕ_c	xiii
S.5	The snapshots of the polymer for (a) low crowder density $\phi_c = 0.035$ and for (b) high density $\phi_c = 0.335$ for different wall attractive strengths.	xiii
1.1	Schematic representation of a polymer in different approaches. A Polymer can be viewed as a sequence of small segments or as a continuous chain.	3
1.2	The random walk model of the polymer with N segments. The black spheres represent the monomers and the thick lines are the bonds between the monomers.	5
1.3	The worm-like chain model. The $\mathbf{r}(s)$ is the position vector of a point on the polymer chain parameterized by parameter s and $\hat{\mathbf{t}}(s)$ is the tangent at the point.	8
1.4	The mixture of polymer and solvent on a lattice. The black spheres represent the monomers while the white spheres represent the solvent particles.	13
1.5	The polymer conformations in (a) good and (b) poor solvents.	16

1.6	A polymer chain confined in a sphere of radius R_c with one end at \mathbf{r}_0 and other at \mathbf{r}	18
1.7	A polymer chain confined in a cylindrical pore of diameter D	19
2.1	Schematic description of different bonded interactions and the parameters involved.	30
2.2	LJ interaction potential (blue) is a combination of a repulsive ($1/r^{12}$) (red) and an attractive $-(1/r^6)$ part (green).	31
3.1	(a) Schematic of the AFM experiment of Ref. [Pagliara et al., 2014] (b) Fluctuations in chromatin compaction arising from the fast on-off dynamics of nucleosomes in the stem cell state, where histones are hyperdynamic (c) Definitions of the variables Ψ , R_{\parallel} , and R_{\perp} in the AFM-based indentation experiment, including the applied force f arising from the indentation (d) Illustration of normal <i>i.e.</i> non-auxetic behaviour in the experiments, showing how the nucleus expands in the direction perpendicular to the applied force f , while the nuclear dimension in the direction parallel to the force contracts. (e) Illustration of auxetic behaviour, showing how the nucleus contracts both in the direction perpendicular to the applied force as well as in the direction parallel to it. The schematic plots in (f) for the non-auxetic case and (g) for the auxetic case show how the variables Ψ , R_{\parallel} , and R_{\perp} behave in both limits as f is increased from zero. The unperturbed nucleus is taken to be spherical.	47
3.2	Parameter choices for C and D and : (a) $B = 10.0$, (b) $B = 2.0$ (c) $B = 0.17$ (d) $B = 0.1$, all in the regime of non-auxetic (regular) behavior . The behaviour of the dynamical variable with the increase in force for the parameter values (e) $C = 0.01, D = 0.02, B = 10.0$. (f) $C = 0.01, D = 0.02, B = 2.0$. (g) $C = 0.01, D = 0.02, B = 0.17$. (h) $C = 0.01, D = 0.02, B = 0.1$. Parameter choices for C and D, in the auxetic regime with (i) $B = -0.1$, (j) $B = -0.17$ (k) $B = -2.0$ (l) $B = -10.0$. The line separating blue and gray regions marks the stable-unstable boundary. The behaviour of the dynamical variable with the increase in force for the parameter values (m) $C = 0.01, D = 0.02, B = -0.1$. (n) $C = 0.01, D = 0.02, B = -0.17$. (o) $C = 0.01, D = 0.02, B = -2.0$. (p) $C = 0.1, D = 0.02, B = -10.0$. (Red and blue colours in the colour plots show the regions where a stable solution is obtained (red = normal, blue = auxetic) while the grey colour shows where solutions become unstable).	57

3.3	<p>(a): Schematic of a cell confined to a microchannel with width comparable to cell dimensions, (b) schematic of the effects of the combination of longitudinal and transverse forces applied to cells of different sizes. These follow from our calculations and are consistent with the results of Ref. [Pagliara et al., 2014], (c) Plots of S_{\parallel} and S_{\perp} extracted from experiments, for the transitional, primed and naive ES cell states. The arrow connects the two terminal points. (d) Contour plots for $\delta\Psi$, δR_{\perp} and δR_{\parallel}, against $(f_{\parallel}, f_{\perp})$, with solid lines showing loci of constant strain (e) Predictions for transitional, primed and naive ES cell states, of S_{\parallel} and S_{\perp}. The straight line represents experimental predictions for intermediate cell sizes. Experimental data are digitized from the scatter plot of Figure S10 of Ref. [Pagliara et al., 2014] and shown on the same figure</p>	59
3.4	<p>Computations of autocorrelations and cross-correlations in the simplified 2-component model, in the auxetic regime, with $C = 0.01$, $D = 0.02$ and $B = -0.17$. We illustrate the calculation of the following correlation functions: (a) The autocorrelation of the $\delta\Psi$ variable $\langle\delta\Psi(0)\delta\Psi(t)\rangle$, (b) The autocorrelation of the δR variable, $\langle\delta R(0)\delta R(t)\rangle$, (c) The cross-correlation between $\delta\Psi$ and δR, $\langle\delta\Psi(0)\delta R(t)\rangle$, (d) The cross-correlation of δR and $\delta\Psi$, $\langle\delta R(0)\delta\Psi(t)\rangle$. The insets show the behaviour close to the origin in two special cases where there is a competition between the two time-scales for relaxation. Points represent the numerical solution of the Langevin equations while lines represent the analytic formulae.</p>	62
3.5	<p>The left columns (a) shows our choice of parameters in (B,C,D) space, with B, shown on the vertical axis, varied so as to cross the auxetic to non-auxetic boundary. The two columns on the right, columns (b) and (c) illustrate the correlation function $\langle\delta R(0)\delta\Psi(t)\rangle$ and $\langle\delta\Psi(0)\delta R(t)\rangle$. Across the auxetic to non-auxetic boundary, where the sign of B changes, the Ψ variable decouples, at lowest order, from the δR variable, leading to a flat behaviour of the correlation $\langle\delta R(0)\delta\Psi(t)\rangle$. In contrast, while Ψ is not influenced by δR, fluctuations in Ψ do couple to δR, leading to a non-trivial relaxation of the correlation function $\langle\delta\Psi(0)\delta R(t)\rangle$. This change of sign of $d\langle\delta R(0)\delta\Psi(t)\rangle/dt$ indicates that the auxetic to non-auxetic boundary has been crossed.</p>	65
3.6	<p>(a) Pictorial representation of values of Ψ_0 for N-ESC, T-ESC and P-cells and (b) pictorial representation of changes in chromatin compaction.</p>	67
3.7	<p>Reconstruction of the potential landscape $V(\delta\Psi)$ in the simplified 2-component model: (a) Assuming a quadratic potential, (b) Assuming a sixth-order potential, and (c) Assuming a quadratic potential with a superimposed sinusoid: $V(\delta\Psi) = a\delta\Psi^2 + b^2\text{Sin}^2(c\delta\Psi)$, for $B = 0.0$ (blue), $B = 1.0$ (red) and $B = -1.0$ (green).</p>	68

3.8	Schematic of an epigenetic landscape in the compaction variable. A pictorial representation of the epigenetic landscape, projected onto a single variable describing overall compaction. Points towards the back of the figure represented the ES cell state while points in the valleys towards the foreground represent differentiated states. As one moves from back to front, the figure describes how the effective potential governing overall compaction can be described via a cut through the landscape as shown.	72
4.1	(a) The radius of gyration of the polymer in a good solvent condition under confinement with repulsive walls (blue) and in the absence of confinement (red) at different crowder densities. Each data point for unconfined and confined polymer is averaged over 10 and 5 simulations respectively. The corresponding error bars are also shown in the figure which represent standard deviation of the data. (b,c) Snapshots of the polymer at the highest crowder density are shown for periodic boundary conditions and spherical confinement.	87
4.2	Relative change in the R_g values, as a function of crowder density, for the unconfined (red) and confined (blue) cases. The values are computed relative to the case of lowest crowder density considered in the study ($\phi_c^{min} = 0.035$). Each data point is averaged over 10 different initial conditions.	88
4.3	Good solvent condition: The snapshots of the polymer conformation for (a) the wall attraction $\epsilon_{mw} = 1.0$, the crowder density $\phi_c = 0.035$, (b) $\epsilon_{mw} = 10.0$, $\phi_c = 0.035$, (c) $\epsilon_{mw} = 10.0$, $\phi_c = 0.435$. The variation of (d) radius of gyration R_g , (e) asphericity b and (f) the fraction of adsorbed monomers f_{ad} with ϕ_c for different ϵ_{mw}	90
4.4	Poor solvent: The snapshots of the polymer for low crowder density $\phi_c = 0.035$ and for high density $\phi_c = 0.435$ for different wall attractive strengths.	91
4.5	Poor solvent: (a,b,c) Different shape parameters of the polymer for various attractive wall strengths as a function of crowder density. The pair radial distribution functions for (d) low crowder density $\phi_c = 0.035$ and (e) high density $\phi_c = 0.335$ for different wall attractive strength ϵ_{mw}	93
4.6	The snapshots of the polymer (a) for good solvent condition (b) for poor solvent condition at different crowder densities $\phi_c = 0.035, 0.235, 0.335, 0.435$ for attractive wall strength $\epsilon_{mw} = 10.0$, (c) Fraction of adsorbed monomers on the surface of confinement as a function of crowder density in good and poor solvent conditions. (d) The radius of gyration of polymer as a function of crowder density for $\epsilon_{mw} = 10.0$	95

4.7	For poor solvent condition and $\epsilon_{mw} = 10.0$ (a) the radial distribution function $g(r)$, (b) the density function $\rho(r')$ for $\phi_c = 0.035, 0.085, 0.185, 0.285, 0.385$.	96
4.8	For poor solvent condition and $\epsilon_{mw} = 20.0$: (a) Snapshots of the system for different values of ϕ_c , and (b) Corresponding contact maps averaged over the final 5×10^6 time steps.	98
4.9	(a) The maximum height of the polymer stack along the radial direction. The height of the stack decreases as the strength of the attraction increases and more and more monomers are recruited along the wall of the confinement. (b) The snapshots of the polymer conformation in poor solvent condition for the different crowder densities.	100
4.10	Snapshots of the system in a poor solvent for (a) $\epsilon_{mw} = 1.0, \phi_c = 0.035$, (b) $\epsilon_{mw} = 20.0, \phi_c = 0.435$ and (c) the pair radial distribution function of polymer for parameters of (a) and (b) . For lower wall attraction ϵ_{mw} and lower density value $\phi_c = 0.035$, the plot suggests less order while for the higher wall attraction $\epsilon_{mw} = 20.0$ and higher crowder density $\phi_c = 0.435$, $g(r)$ shows many peaks indicating more order in the system.	101
4.11	Average number of neighbours for (a) $\epsilon_{mw} = 1.0, \phi_c = 0.035$ and (b) $\epsilon_{mw} = 20.0, \phi_c = 0.435$. The average number of neighbours for higher density ($\phi_c = 0.435$) and higher wall attraction ($\epsilon_{mw} = 20.0$) system is about 9 which is higher than that for lower wall attraction ($\epsilon_{mw} = 1.0$) and lower crowder density ($\phi_c = 0.035$) system. This suggests that polymer is more ordered in the higher crowder density system than for the lower density system.	101
4.12	The density function of the monomers in poor solvent condition confined within attractive walls (a) for the sphere of radius $R = 15.0$ (b) for the sphere of radius $R = 30.0$.	103
4.13	Conformations of polymer under different crowder densities and attractive wall strengths for the poor and good solvent condition in $\phi_c - \epsilon_{mw}$ space.	104
4.14	Model representation of the simulated system. (a) The lateral view and (b) the cross-sectional view of the system. The blue color particles represent the anchor monomers, red color particles are the monomers which are not fixed to the cylindrical wall, the crowder particles and the tracer particle are shown in grey and yellow respectively. (Note that tracer particle is shown bigger than the original size for better visualization.)	107
4.15	The radius of gyration of polymer grafts for poor and good solvent conditions and different monomer-wall interactions. The symbols are abbreviations for, GS: good solvent, PS: poor solvent, AW: attractive wall, RW: repulsive wall.	110

4.16	The plot shows $\langle(z(t + \tau) - z(t))^2\rangle$ vs τ for poor and good solvent condition and different wall interactions. Super-diffusive behaviour is seen for $\phi_c = 0$, while behaviour shifts to normal Brownian motion for $\phi_c > 0$	111
4.17	The plot shows the diffusion coefficient D vs crowder density ϕ_c for good and poor solvent conditions with different wall-monomer interactions. The diffusion coefficient decreases as more number of crowder particles are added to the system regardless of solvent condition and monomer-wall interaction.	111
4.18	The average monomer distribution in the cylindrical confinement for different solvent conditions and monomer-wall interactions. Monomers largely avoid the contact with the wall except for the high attractive interaction strength $\epsilon_{mw} = 10$	112
4.19	The crowder particle distributions for different solvent conditions and monomer-wall interactions. The crows are uniformly distributed in the middle of the tube while show layering for higher crowder density neat the wall of the tube.	113
4.20	The pair distribution function for monomer-monomer pairs. Enhanced ordering is seen in poor solvent conditions whereas for good solvent conditions, this order reduces.	113
4.21	The pair distribution function for monomer-crowder pairs. The monomer-crowder pairs are less ordered for poor solvent conditions as compared in the good solvent conditions.	114
A.1	Computations of autocorrelations and cross-correlations, in the auxetic regime, with $C = 0.01$, $D = 0.02$ and $B = -0.17$. (a) the autocorrelation function for $\delta\Psi$, $\langle\delta\Psi(0)\delta\Psi(t)\rangle$, (b) the autocorrelation function for δR_{\parallel} , $\langle\delta R_{\parallel}(0)\delta R_{\parallel}(t)\rangle$, (c) the autocorrelation function for δR_{\perp} , $\langle\delta R_{\perp}(0)\delta R_{\perp}(t)\rangle$, (d) the cross-correlation function for $\delta\Psi$ and δR_{\parallel} , $\langle\delta\Psi(0)\delta R_{\parallel}(t)\rangle$, (e) he cross-correlation function for δR_{\parallel} and δR_{\perp} , $\langle\delta R_{\parallel}(0)\delta R_{\perp}(t)\rangle$ and (f) he cross-correlation function for δR_{\perp} and $\delta\Psi$, $\langle\delta R_{\perp}(0)\delta\Psi(t)\rangle$. The insets show the behaviour close to the origin in two special cases where there is a competition between the two time-scales for relaxation. Points represent the numerical solution of the Langevin equations while lines represent the analytic formulae.	127
A.2	The figure shows the long time cross-correlation function $\langle\delta R_{\perp}(0)\delta\Psi(t)\rangle_{t\gg 0}$ with the various values of B from $B = -1.0$ to $B = 1.0$ including the $B = 0$ case. We see that the slope of the correlation function changes as the sign of the parameter B changes from negative to positive. . .	128

A.3	The correlation functions: (a) the cross-correlation function for δR_{\perp} and $\delta\Psi$, $\langle\delta R_{\perp}(0)\delta\Psi(t)\rangle$ (b) the cross-correlation function for $\delta\Psi$ and δR_{\perp} , $\langle\delta\Psi(0)\delta R_{\perp}(t)\rangle$ (c) the cross-correlation function for δR_{\parallel} and $\delta\Psi$, $\langle\delta R_{\parallel}(0)\delta\Psi(t)\rangle$ (d) the cross-correlation function for $\delta\Psi$ and δR_{\parallel} , $\langle\delta\Psi(0)\delta R_{\parallel}(t)\rangle$ with different values of parameter B . We see that the correlation functions $\langle\delta R_{\perp}(0)\delta\Psi(t)\rangle$ and $\langle\delta R_{\parallel}(0)\delta\Psi(t)\rangle$ change the slope with the parameter B while there is no such effect on $\langle\delta\Psi(0)\delta R_{\perp}(t)\rangle$ and $\langle\delta\Psi(0)\delta R_{\parallel}(t)\rangle$	130
A.4	The behaviour of the systems under periodic force: The figure (a) shows that how an auxetic system (b) a normal system behaves under a periodic force. It can be seen that in auxetic case, both radii δR_{\parallel} and δR_{\perp} simultaneously increase or decrease while in normal case, if one increases, the other decreases and vice-versa.	131

List of Tables

4.1	Table of parameters for LJ potential for good and poor solvent conditions. Different values of r_c determine the solvent condition. To delineate the effect of poor solvent conditions, a higher value of ϵ_{ij} was used between monomers and crowder particles, though the potential is soft-core repulsion for good and bad solvent cases.	84
4.2	Table of parameters for interaction potential for good and poor solvent conditions. Different values of r_c determine the solvent condition of the system.	108

Chapter 1

Introduction

Polymers are long molecules made up of smaller chemical units called monomers linked together via covalent bonds [de Gennes, 1979, Doi, 1996]. As extended structures, they constitute the main physical components of biological cells. Filaments of the cytoskeleton (microtubules, intermediate filaments and actin) which provide architectural stability as well as a network for intracellular transport, double-helical DNA which encodes RNA sequence, and proteins synthesized using the information in RNA, are all biological polymers [Alberts et al., 2013, Boal and Boal, 2012, Phillips et al., 2012]. Non-biological (synthetic) polymers exist as well. An example is polyethylene ($-CH_2 - CH_2 - CH_2-$), composed of the identical repeating unit ethylene ($CH_2 = CH_2$).

Understanding how confinement constraints the configurations of long molecules is important in many biological processes. An example is DNA inside a nucleus. If the DNA was straightened out, it would be orders of magnitude larger than the nuclear radius. Even in non-extended form, the radius of gyration of an equivalent length of DNA would exceed nuclear dimensions. The entropy of polymers decreases when they are confined. Confinement thus affects other properties as well, including diffusivity, elastic modulus etc [Vogt, 2018]. Confined polymers are relevant not only

in biological processes but also in nanofabrication and in the passage of polymers through narrow pores in industrial contexts [Tegenfeldt et al., 2004, Chen et al., 2004, Reisner et al., 2005, Jo et al., 2007, Balducci et al., 2006, Reisner et al., 2007].

In this chapter, various models for confined and unconfined polymers used in polymer physics are discussed. We first motivate why using simple, minimal models is often sufficient to understand the behaviour of polymers on relatively larger time and length scales.

1.1 Polymer Models

A polymer is a long chain molecule that can be up to 10^8 monomers long. It has a backbone which is generally a carbon atom chain, with other atoms attached to it (e.g. N, H, O). Atomic-scale simulations are computationally very expensive. Such simulations are generally done for a small number of particles. However, with advancements in high-performance computing, simulations for 10^6 particles are now routine [Hospital et al., 2015]. One might have naively expected that a considerable degree of molecular detail would be required to make a sensible prediction about the physical behavior of a polymer, but this is neither necessary nor indeed always feasible. Indeed, the degree of detail we need depends upon the time and length scales that are natural to the problem we are interested in investigating.

What are useful models of polymers that do not incorporate atomistic detail? This depends upon the problem we are interested in and the method we want to employ to solve the problem. In some cases, where computer simulations are employed, a polymer can be thought of as a sequence of N segments of length b with appropriate interactions (see Figure 1.1(a)). On the theoretical side, a polymer can be modelled as a continuous chain where the position at every point in real space is parametrized by a single one-dimensional coordinate, usually the arc-length (see Figure 1.1(b)).

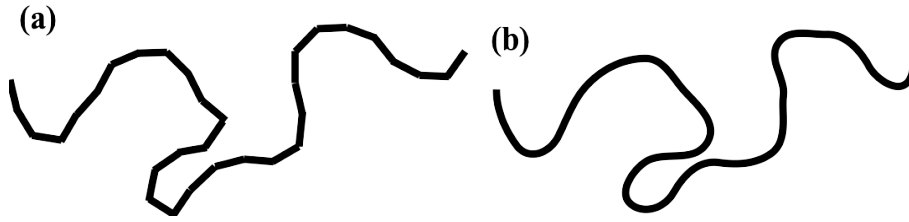


Figure 1.1: Schematic representation of a polymer in different approaches. A Polymer can be viewed as a sequence of small segments or as a continuous chain.

A polymer has a large number of internal degrees of freedom and can take many different conformations. To study such a system, we first study a simple coarse-grained model where monomers follow a regular lattice and nearest neighbours are connected with a bond.

First, we discuss an ideal chain model. This is useful in describing flexible polymers. The end-to-end distance follows a Gaussian distribution. We also discuss briefly the Gaussian chain model in which the distribution of individual bond sizes is modeled as Gaussians. We further discuss the worm-like chain model where stiffness is introduced in the chain through interaction energy between the neighboring segments. We also discuss two extreme limits of this model.

1.2 Flexible Polymer

1.2.1 The ideal chain on a lattice

This is a basic model describing the properties of a large class of flexible polymers. In this model, a polymer chain is composed of N segments of size b , where the segments can cross each other. In this freely jointed chain (FJC) model, the polymer configuration is a sequence of N steps of a random walk with step length b (see

Figure 1.2). Let $\mathbf{a}_1, \mathbf{a}_2, \dots, \mathbf{a}_N$ be the steps of the random walk. The monomers have no excluded volume and repulsion among them, hence the correlation between the direction of steps of the random walk is zero, giving rise to,

$$\begin{aligned}\langle \mathbf{R} \rangle &= \sum_{i=1}^N \langle \mathbf{a}_i \rangle, \\ &= 0,\end{aligned}\tag{1.1}$$

where \mathbf{R} is the end-to-end distance vector and $\langle \cdot \rangle$ refers to the mean value of the variable.

The mean square end-to-end distance $\langle \mathbf{R}^2 \rangle$ can be computed as,

$$\langle \mathbf{R}^2 \rangle = \sum_{i=1}^N \sum_{j=1}^N \langle a_i a_j \rangle.$$

Since $\langle a_i a_j \rangle$ is zero for $i \neq j$,

$$\begin{aligned}\langle \mathbf{R}^2 \rangle &= \sum_{i=1}^N \sum_{i=1}^N \langle a_i^2 \rangle, \\ &= Nb^2.\end{aligned}\tag{1.2}$$

Since vectors $\mathbf{a}_1, \mathbf{a}_2, \dots, \mathbf{a}_N$ are independent, we invoke the central limit theorem, according to which the sum of these vectors $\mathbf{R} = \sum_{i=1}^N \mathbf{a}_i$ is distributed according to a Gaussian distribution and the distribution $P(\mathbf{R})$ is given by the same expression as for the random walk model,

$$P(\mathbf{R}) = \left(\frac{3}{2\pi Nb^2} \right)^{-3/2} \exp \left(-\frac{3\mathbf{R}^2}{2Nb^2} \right),\tag{1.3}$$

with zero mean and variance $\langle \mathbf{R}^2 \rangle = Nb^2$. The quantity $\langle \mathbf{R}^2 \rangle$ typically gives the

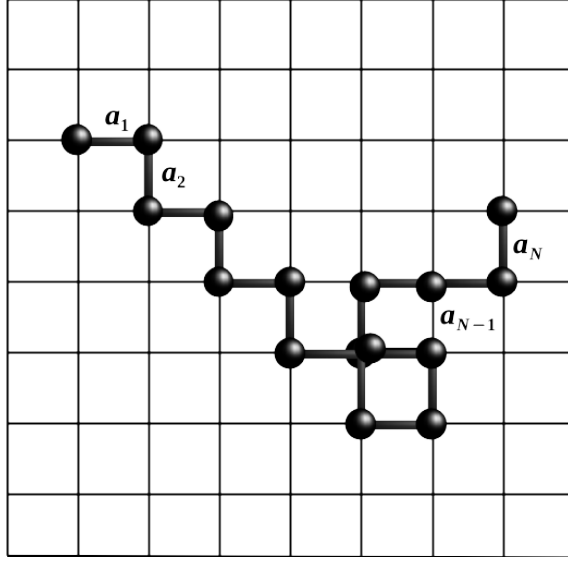


Figure 1.2: The random walk model of the polymer with N segments. The black spheres represent the monomers and the thick lines are the bonds between the monomers.

idea about the extent of the polymer as opposed to its contour length Nb . From Eq. 1.2,

$$R \sim bN^{1/2}. \quad (1.4)$$

The end-to-end distance of an ideal chain polymer scales in the number of segments with an exponent $\nu = 1/2$.

The radius of gyration R_g is also used for describing the polymer size as in many cases such as branched polymers where end-to-end distance R is not useful. R_g^2 is defined as the mean square distance between all the monomers and the center of mass to all the monomers,

$$R_g^2 = \frac{1}{N} \sum_{i=1}^N (\mathbf{r}_i - \mathbf{R}_{CM})^2, \quad (1.5)$$

$$= \frac{1}{2N^2} \sum_{i=1}^N \sum_{j=1}^N (\mathbf{r}_i - \mathbf{r}_j)^2, \quad (1.6)$$

where $\mathbf{R}_{CM} = \frac{1}{N} \sum_{i=1}^N \mathbf{r}_i$ is the center of mass and \mathbf{r}_i is the position vector of the i^{th}

segment.

We now calculate R_g for the ideal chain model. From Eq. 1.2, $\langle (r_n - r_m)^2 \rangle = |n - m| b^2$ for large $|n - m|$. Using definition 1.6,

$$R_g^2 = \frac{1}{2N^2} \sum_{n=1}^N \sum_{m=1}^N |n - m| b^2.$$

For large N , the summation can be replaced by integration,

$$\begin{aligned} R_g^2 &= \frac{1}{2N^2} \int_1^N dn \int_1^N dm |n - m| b^2, \\ &= \left(\frac{N}{6} \right) b^2. \end{aligned} \tag{1.7}$$

Both the end-to-end distance R and radius of gyration R_g scale as $N^{1/2}$. This model can be used to describe a flexible polymer, as the correlation between the segments decay on a smaller length scale than the length of the polymer.

1.2.2 The Gaussian Chain Model

In this model, the polymer chain is considered to be made of randomly oriented (freely jointed) segments. The length of a segment is not a constant but has a Gaussian probability distribution given by,

$$P(a) = \left(\frac{3}{2\pi b^2} \right)^{-3/2} \exp\left(-\frac{3a^2}{2b^2}\right), \tag{1.8}$$

with the expectation value of the segment length given by,

$$\langle a^2 \rangle = b^2. \tag{1.9}$$

This way, the Gaussian behavior is embedded at every length scale in this model

rather than just in the end-to-end distance. Using this, the probability distribution of the end-to-end vector \mathbf{R} is given by the product,

$$P(\mathbf{R}) = \prod_{i=1}^N \left(\frac{3}{2\pi b^2} \right)^{-3/2} \exp \left(-\frac{3a_i^2}{2b^2} \right). \quad (1.10)$$

1.3 Semi-flexible Polymers

1.3.1 Worm-like Chain

The models discussed so far have neglected self-avoidance as well as bending rigidity i.e. there is no energy cost to bend the polymer chain. In reality, all polymers are not completely flexible. Biological polymers are typically stiff at a length scale comparable to the size of several monomers. The worm-like chain model is used to describe a stiff polymer, where the stiffness is incorporated by requiring that two successive segments reduce their energy when aligned. This model for a semi-flexible polymer is sometimes referred to as the Kratky-Porod model [Kratky and Porod, 1949, Saitô et al., 1967].

Let's consider a chain of maximum length L . A point on the polymer is parametrized by a variable s . A tangent on this point along the polymer is $\hat{\mathbf{t}}(s)$ and $\mathbf{r}(s)$ is the position vector of the point (see Figure 1.3). The tangent vector is given by,

$$\hat{\mathbf{t}}(s) = \frac{\partial \mathbf{r}}{\partial s}. \quad (1.11)$$

The energy associated with bending the polymer can be written as,

$$E = \frac{1}{2} k_B T \int_0^L ds l_p \left(\frac{\partial^2 \mathbf{r}(s)}{\partial s^2} \right)^2, \quad (1.12)$$

where l_p is persistence length for the polymer, k_B the Boltzmann constant and T is

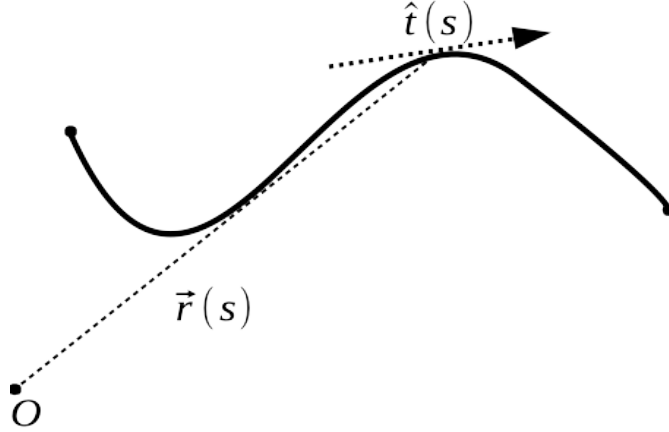


Figure 1.3: The worm-like chain model. The $\mathbf{r}(s)$ is the position vector of a point on the polymer chain parameterized by parameter s and $\hat{\mathbf{t}}(s)$ is the tangent at the point.

the absolute temperature. The persistence length l_p is a length scale related to the bending stiffness of the polymer. The physical meaning of the persistence length is the following: Chain segments are roughly aligned on length scales smaller than l_p while they are decorrelated at length scales much larger than l_p [Khokhlov et al., 2011].

The tangent-tangent correlation function can be solved exactly. It decays exponentially with distance along the chain.

$$\langle \hat{\mathbf{t}}(s) \cdot \hat{\mathbf{t}}(0) \rangle = \exp(-s/l_p). \quad (1.13)$$

The mean square end-to-end distance of the polymer can be calculated as,

$$\begin{aligned} \langle R^2 \rangle &= \langle \mathbf{R} \cdot \mathbf{R} \rangle, \\ &= \left\langle \left(\int_0^L ds \hat{\mathbf{t}}(s) \right) \cdot \left(\int_0^L ds' \hat{\mathbf{t}}(s') \right) \right\rangle, \\ &= \int_0^L ds \int_0^L ds' \langle \hat{\mathbf{t}}(s) \cdot \hat{\mathbf{t}}(s') \rangle. \end{aligned} \quad (1.14)$$

Using Eq. 1.13 and integrating Eq. 1.14,

$$\langle R^2 \rangle = 2l_p L \left[1 - \frac{l_p}{L} (1 - e^{-l_p/L}) \right].$$

There are two limits,

$$\langle R^2 \rangle = \begin{cases} 2l_p L, & \text{for } L \gg l_p \\ L^2, & \text{for } L \ll l_p \end{cases}$$

In the first limit, where the chain persistence length l_p is much smaller than chain length L , the model behaves as an FJC and the chain follows Gaussian statistics.

In the second limit, where $l_p \gg L$, the chain behaves like a stiff rod.

In this model, the radius of gyration can be calculated as following,

$$\langle R_g^2 \rangle = \frac{1}{2L^2} \int_0^L ds \int_0^L ds' \langle (r(s) - r(s'))^2 \rangle.$$

Using $r(s) - r(s') = \int_s^{s'} d\tau \hat{\mathbf{t}}(\tau)$

$$\begin{aligned} \langle R_g^2 \rangle &= l_p^2 \left(f_D \left(\frac{L}{l_p} \right) - 1 + \frac{L}{3l_p} \right), \\ &= \begin{cases} \frac{2l_p L}{6}, & \text{for } L \gg l_p \\ \frac{L^2}{12}, & \text{for } L \ll l_p \end{cases} \end{aligned} \quad (1.15)$$

where f_D is the Debye function and is given by [Doi and Edwards, 1988],

$$f_D(x) = \frac{2}{x^2} (e^{-x} - 1 + x).$$

1.4 Non-ideal Chains

1.4.1 The Self-avoiding Chain

In the ideal chain model, the chain can overlap itself. In real polymers, monomers interact with the solvent as well as amongst themselves. In good solvent conditions, they tend to adopt swollen conformations, which can be modeled as an effective repulsion between monomers. In a poor solvent where the monomer-monomer interaction outweighs the monomer-solvent interaction, the polymer conformations are compact. This can be modelled as an effective attractive interaction between monomers. In computational models, the tendency of the polymer not to cross itself in physical space can be modelled as an excluded volume effect. To include this effect into the model, a steep repulsive interaction potential is introduced which prohibits the interpenetration of polymer segments.

Self-avoidance changes the size exponent ν in the relation $R \sim N^\nu$ [Doi, 1996]. The size of the polymer increases when the self-avoidance is introduced. The exponent depends upon the dimensionality of the system because the effect of self-avoidance reduces in a higher dimension. For dimension $d = 1$, $\nu = 1$. Also, for $d \rightarrow \infty$, $R \sim N^{1/2}$ must be recovered.

1.4.2 Flory Theory

Flory tried to estimate the size of the self-avoiding chain [Flory, 1965, Flory, 1970] by balancing the excluded volume interaction energy which tends to swell the chain and the entropic interaction which tend to restore Gaussian behavior. The mean density of monomers in the chain of size R is N/R^d , where d is the dimension of the space in which the chain is embedded. The excluded volume of a monomer is a^d , where a represents monomer size. Hence the excluded volume interaction energy for

a single chain is given by,

$$F_{excl} \sim k_B T \frac{a^d N^2}{R^d}. \quad (1.16)$$

The entropic contribution to the free energy is given by,

$$F_{ent} \sim k_B T \frac{R^2}{N b^2}. \quad (1.17)$$

The equilibrium size of the coil is calculated by minimizing the total energy function

$$F = F_{excl} + F_{ent}.$$

$$\begin{aligned} F &\sim k_B T \frac{a^d N^2}{R^d} + k_B T \frac{R^2}{N b^2}, \\ \frac{\partial F}{\partial R} &\sim 0, \\ R &\sim N^{\frac{3}{d+2}}. \end{aligned}$$

Comparing it with $R \sim N^\nu$, we get $\nu = \frac{3}{d+2}$. This relation is called the Flory formula. For

- $d = 1$, $R \sim N$, which is exact,
- $d = 2$, $R \sim N^{3/4}$, which is exact,
- $d = 3$, $R \sim N^{3/5}$, the more accurate value $\nu \approx 0.588$ comes from simulation,
- $d = 4$, $R \sim N^{1/2}$, this is again an exact. In this dimension, chain behaves as an ideal chain.

It is important to note that the success of Flory theory is due to the cancellation of two errors [de Gennes, 1979]. Flory's method is used for its simplicity in many cases such as linear chains with stiffness and polymers in confined spaces.

1.5 Polymers in Solvent: Flory-Huggins Mean-field Theory

In biological systems, polymers are usually found in solutions [Alberts et al., 2013]. Polymers in a solution behave very differently in different concentration regimes. The overlap concentration c^* of the polymer above which polymers begin to overlap and entangle with each other is defined as [Doi, 1996, de Gennes, 1979],

$$c^* \sim N/R_g^3, \quad (1.18)$$

where, N is the degree of polymerization.

Now assuming ideal solution and using $R_g \sim N^{1/2}$ leads to,

$$c^* \sim N^{-1/2}, \quad (1.19)$$

$$\phi^* \sim vN^{-1/2}, \quad (1.20)$$

where, ϕ^* is the overlap volume fraction and v is the volume of a monomer. We see that for large N , the overlap volume fraction ϕ^* is very small implying that even for very low volume fraction ($\phi \ll 1$), the polymers are overlapped. The solutions with $\phi < \phi^*$ are called dilute solution and with $\phi > \phi^*$ and $\phi \ll 1$ are dubbed as semi-dilute solution. The semi-dilute regime is a specific feature of the polymer solution. When $\phi \gg \phi^*$ and $\phi < 1$, the polymer solution is concentrated and highly entangled.

The Flory-Huggins theory is a lattice-based mean-field theory used to describe polymer solutions [Flory, 1965, Huggins, 1964]. It is an extension of lattice mean-field theory which describes the dissolution of two low molecular weight liquids. The dissolution of a polymer into a solvent changes the free energy of the polymer-solvent system. The Flory-Huggins mean-field theory compares the free energy of the system

of polymer and solvent before and after mixing. Figure 1.4 shows a two-dimensional

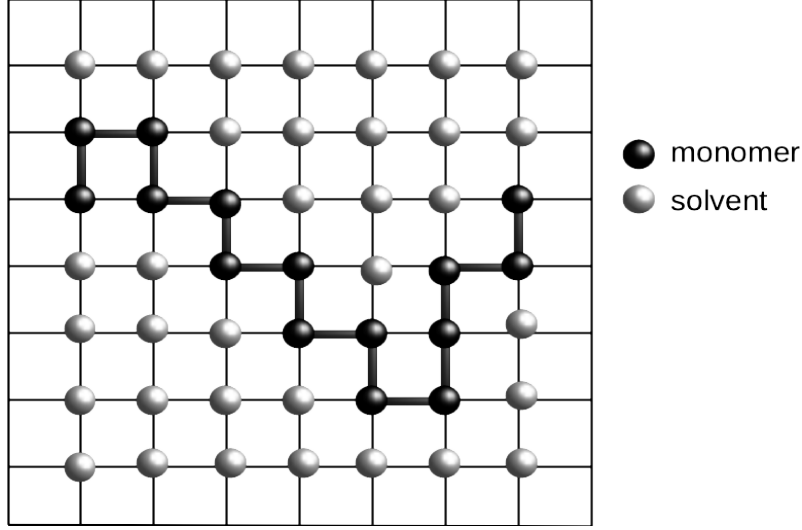


Figure 1.4: The mixture of polymer and solvent on a lattice. The black spheres represent the monomers while the white spheres represent the solvent particles.

version of a polymer-solvent system which has total n_{tot} number of lattice sites and each site is occupied by either a monomer or a solvent particle. Let N_s be the number of solvent particles, N_p be the number of polymers and N be the degree of polymerization, then,

$$n_{tot} = N_s + NN_p. \quad (1.21)$$

The polymer volume fraction ϕ is defined as,

$$\phi = \frac{NN_p}{n_{tot}}. \quad (1.22)$$

The entropy of mixing per lattice-site for the polymer-solvent system can be written as the following,

$$\frac{\Delta S}{k_B T n_{tot}} = - \left(\frac{\phi}{N} \ln \phi + (1 - \phi) \ln (1 - \phi) \right), \quad (1.23)$$

where $(1 - \phi)$ is the volume fraction of solvent particles. This expression is somewhat similar in form to the expression for the entropy of mixing for two liquids [Hill, 1986] but for a few crucial differences. The first difference is that the volume fraction

appears in place of the mole fraction and the second one is that the degree of polymerization N appears explicitly. This is because the monomers are connected, which reduces the number of conformations of the polymer by a factor of $1/N$.

Since the entropy of mixing is small especially at low concentration, the miscibility of polymer in the solvent is governed by the change in interaction energy (enthalpy change) upon mixing. We take ϵ_{pp} , ϵ_{ss} and ϵ_{ps} to be the interaction energy associated with polymer-polymer, solvent-solvent and polymer-solvent contacts respectively. Then the change in interaction energy per lattice site before and after mixing χ will be given by,

$$\chi = z(\epsilon_{ps} - (\epsilon_{pp} + \epsilon_{ss})/2)/k_B T, \quad (1.24)$$

where z is the lattice co-ordination number and χ is called the Flory-Huggins parameter. A positive value of χ indicates that the polymer-solvent contacts are preferred and the polymer prefers to dissolve in solvent. A negative value indicates that the polymer-solvent contacts are less favored. The enthalpy of mixing ΔH is given by the change in number of contacts before and after mixing times the change in interaction energy per lattice site,

$$\begin{aligned} \frac{\Delta H}{k_B T n_{tot}} &= z(\epsilon_{ps} - (\epsilon_{pp} + \epsilon_{ss})/2)\phi(1 - \phi), \\ &= \chi\phi(1 - \phi) \end{aligned} \quad (1.25)$$

From Eq. 1.23 and Eq. 1.25, the free energy of mixing per lattice site is given by,

$$\frac{\Delta F}{k_B T n_{tot}} = \frac{\phi}{N} \ln \phi + (1 - \phi) \ln (1 - \phi) + \chi\phi(1 - \phi). \quad (1.26)$$

Various quantities can be calculated from the free energy. If P is the pressure and $V = n_{tot}v_c$ is the volume of the system, the Gibbs free energy G can be written as,

$$G(N_p, N_s, P, T) = F + PV = F + P(N_p N + N_s)v_c \quad (1.27)$$

The chemical potential of the polymer is given by the change in the Gibb's free energy when a polymer is added to the system keeping other variables N_s, T, P constant.

$$\begin{aligned}\mu_p(\phi, P, T) &= \frac{1}{N} (G(N_p + 1, N_s, P, T) - G(N_p, N_s, P, T)) \\ &= \mu_p^0(T) + k_B T \left(\Delta F + (1 - \phi) \frac{\partial \Delta F}{\partial \phi} \right) + P v_c\end{aligned}\quad (1.28)$$

Similarly, the chemical potential of the solvent is given by,

$$\mu_s(\phi, P, T) = \mu_s^0(T) + k_B T \left(\Delta F - \phi \frac{\partial \Delta F}{\partial \phi} \right) + P v_c \quad (1.29)$$

Since the polymers are dispersed in the solvent, the osmotic pressure Π of the solution can also be calculated. The osmotic pressure is the extra pressure that must be applied across a semi-permeable membrane to maintain the equilibrium of solvent particles. Hence,

$$\mu_s(\phi, P + \Pi, T) = \mu_s(0, P, T). \quad (1.30)$$

Using Eq. 1.29 in Eq. 1.30, we get,

$$\Pi = \frac{k_B T}{v_c} \left(\phi \frac{\partial \Delta F}{\partial \phi} - \Delta F \right) \quad (1.31)$$

Using Eq. 1.26 in Eq. 1.31 yields,

$$\Pi = \frac{k_B T}{v_c} \left(\frac{\phi}{N} - \ln(1 - \phi) - \phi - \chi \phi^2 \right) \quad (1.32)$$

This expression of osmotic pressure is also used in chapter 3.

1.5.1 Effect of Solvent Quality

The size and shape of the polymer depends strongly upon the quality of the solvent in the polymer solution. In good solvent conditions, the polymer takes on an expanded conformation to increase polymer-solvent contacts. In poor solvent, the polymer shrinks to take a compact globular structure to minimize the polymer-solvent contacts and to maximize monomer-monomer contacts (see Figure 1.5). The size of the polymer in poor solvents follows $R_g \sim bN^{1/3}$ while in a good solvent, $R_g \sim N^{3/5}$.



Figure 1.5: The polymer conformations in (a) good and (b) poor solvents.

1.6 Polymers Under Confinement

Confinement of the macromolecules is very common in biological systems and drug delivery applications. For example, stretching DNA in nano-channels is an important technique for separating DNA to perform experiments such as genome sequencing, restriction mapping [Reisner et al., 2012, Riehn et al., 2005, Douville et al., 2008]. Also, understanding polymer confined in nano-channels serves as to understand chromosome organization and viral DNA packing. Polymers in dilute solution have many degrees of freedom. Upon confinement, the number of conformations a polymer molecule can assume reduces and this leads to a variety of interesting effects. This entropic penalty associated with confinement has important implications for the behavior and dynamics of the polymer. Confining cavities can be of different

shapes. The interaction between the polymer and cavity wall can also potentially be tuned to give the energy contribution.

In this section, we discuss the behavior of the polymers under confinement. We discuss different approaches to derive the free energy of the polymer under confinement.

1.6.1 Analytical Approach to Confinement

A natural confining geometry is a spherical one. In this section, we consider a Gaussian polymer chain with one end at \mathbf{r}_0 and other end at \mathbf{r} within a sphere of radius R_c (see Figure 1.6). The probability of finding an unconfined chain of size N with its ends at \mathbf{r}_0 and \mathbf{r} is given by,

$$P(\mathbf{r}, \mathbf{r}_0; N) = \left(\frac{3}{2\pi N b^2} \right)^{3/2} \exp \left[-\frac{3(\mathbf{r} - \mathbf{r}_0)^2}{2N b^2} \right]. \quad (1.33)$$

This probability distribution satisfies the following diffusion equation,

$$\left(\frac{\partial}{\partial N} - \frac{b^2}{6} \nabla^2 \right) P(\mathbf{r}, \mathbf{r}_0; N) = 0, \quad (1.34)$$

In order to obtain the free energy of polymer under confinement, we need to solve Eq. 1.34 with the boundary condition that P is zero when the polymer ends \mathbf{r}_0 and \mathbf{r} are at the boundary of the confinement [Muthukumar, 2012a, Muthukumar, 2016].

We neglect the angular dependence. Eq. 1.34 can be written as,

$$\frac{\partial}{\partial N} P(\mathbf{r}, \mathbf{r}_0; N) = \frac{b^2}{6} \frac{1}{r^2} \frac{\partial}{\partial r} \left(r^2 \frac{\partial}{\partial r} P(\mathbf{r}, \mathbf{r}_0; N) \right). \quad (1.35)$$

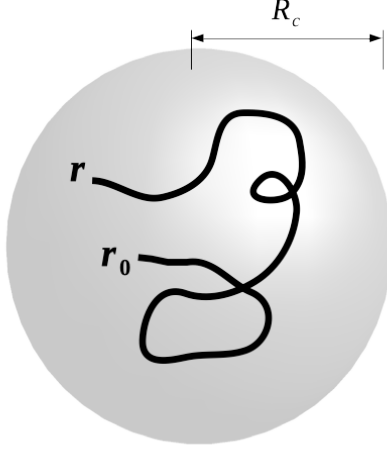


Figure 1.6: A polymer chain confined in a sphere of radius R_c with one end at \mathbf{r}_0 and other at \mathbf{r} .

This equation can be solved by the separation of variable method. The solution is [Muthukumar, 2016],

$$P(\mathbf{r}, \mathbf{r}_0; N) = \frac{1}{2Rr r_0} \sum_{m=1}^{\infty} \sin\left(\frac{m\pi r_0}{R}\right) \sin\left(\frac{m\pi r}{R}\right) \exp\left[-\frac{m^2\pi^2 N b^2}{6R^2}\right]. \quad (1.36)$$

If both the ends of polymers are allowed anywhere in the cavity, the partition function Z is computed by averaging over \mathbf{r}_0 and \mathbf{r} . It is given as,

$$Z = \left(\frac{4\pi R_c^3}{3b^3}\right) \frac{6}{\pi^2} \sum_{m=1}^{\infty} \frac{1}{m^2} \exp\left[-m^2\pi^2 \left(\frac{N b^2}{6R_c^2}\right)\right]. \quad (1.37)$$

The free energy of the polymer can be written using $F = -k_B T \ln Z$. Using Eq. 1.37,

$$\frac{F}{k_B T} = -\ln\left(\frac{4\pi R_c^3}{3b^3}\right) - \ln\left[\frac{6}{\pi^2} \sum_{m=1}^{\infty} \frac{1}{m^2} \exp\left[-m^2\pi^2 \left(\frac{R_g}{R_c}\right)^2\right]\right], \quad (1.38)$$

In Eq. 1.38 the first term is due to translational entropy of the chain and the second is due to the confinement. The radius of gyration R_g for the Gaussian chain is related to N by the expression $R_g^2 = N b^2 / 6$.

1.6.2 Scaling Approach to Confinement

In this section, we derive the free energy expression for a flexible polymer chain in a cylindrical cavity using scaling arguments. Let's consider a polymer chain with N segments confined in an infinitely long cylindrical pore with diameter D . The average polymer dimension along the length of the cylinder is R_{\parallel} (see Figure 1.7). In case of no confinement or very weak confinement, R_{\parallel} is proportional to the radius of gyration R_g of the polymer. Under strong confinement, the size of the polymer along the length of pore will be proportional to N [de Gennes, 1979]. Keeping these arguments in mind,

$$R_{\parallel} \sim R_g f(D/R_g), \quad (1.39)$$

where $f(D/R_g)$ is a scaling function of a dimensionless variable D/R_g .

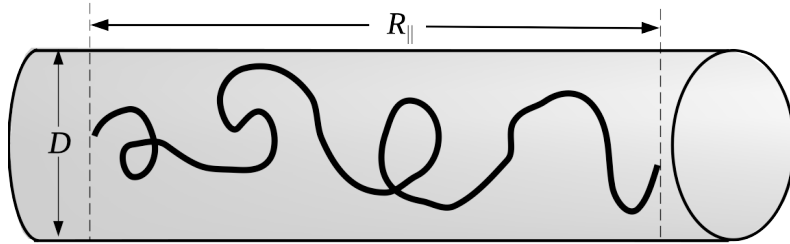


Figure 1.7: A polymer chain confined in a cylindrical pore of diameter D .

When a polymer is placed under strong confinement i.e. $D \ll R_g$, the polymer dimension $R_{\parallel} \sim N$. Since $R_g \sim N^\nu$, this can be the case only when the scaling function is an algebraic function of the variable D/R_g [de Gennes, 1979]. Using this relation, Eq. 1.39 can be written as,

$$R_{\parallel} \sim R_g \left(\frac{D}{R_g} \right)^x. \quad (1.40)$$

Thus, for strong confinement,

$$N \sim N^\nu \left(\frac{D}{N^\nu} \right)^x. \quad (1.41)$$

Comparing the powers of N yields,

$$x = -\frac{1-\nu}{\nu}. \quad (1.42)$$

From Eq. 1.40 and Eq. 1.42,

$$R_{\parallel} = \frac{N}{D^{1/\nu-1}}. \quad (1.43)$$

Hence, under weak confinement where $D \gg R_g$, $R_{\parallel} \sim R_g$ while for strong confinement where $D \ll R_g$, Eq. 1.43 is followed.

$$R_{\parallel} \sim \begin{cases} R_g, & \text{for } D \gg R_g \\ \frac{N}{D^{1/\nu-1}}, & \text{for } D \ll R_g \end{cases}$$

Similarly, using the scaling function, the free energy of confinement can be written in terms of a function of a dimensionless variable D/R_g ,

$$\frac{F}{k_B T} \sim f_s \left(\frac{D}{R_g} \right), \quad (1.44)$$

where f_s is scaling function of variable D/R_g . For strong confinement, the energy must be linear in N , as doubling the N will double the energy. Using similar arguments and calculations as in deriving Eq. 1.43, the expression for the confinement free energy can be written as,

$$\frac{F}{k_B T} \sim \frac{N}{D^{1/\nu}} \quad (1.45)$$

1.6.3 Thermodynamic Approach to Confinement

The polymer under confinement is very similar to the polymer in a solvent with the solvent boundary being the wall of the confinement. Thus, the Flory-Huggins theory of polymer solutions can be used to get the free energy expression [Muthukumar,

2012a]. The free energy of the polymer under confinement has two parts. The first part comes from the translational entropy and the enthalpy contribution of polymer segments and solvent particles (see section 1.5). A dilute and semidilute solution is characterized by large and strongly correlated fluctuations in the monomer density that are absent in the melt. The second part of free energy arises due to monomer density fluctuations and can be given by [Muthukumar, 1986, Muthukumar and Edwards, 1982],

$$\frac{\Delta F_{fluc}}{k_B T \Omega} \sim \frac{1}{24\pi\xi^3}, \quad (1.46)$$

where ξ is the correlation length which depends upon the polymer volume fraction ϕ . The correlation length ξ is proportional to $\phi^{-1/2}$ for concentrated solutions and $\phi^{-3/4}$ for semi-dilute solutions.

The total free energy can be written as the sum of Eq. 1.26 and Eq. 1.46,

$$\frac{\Delta F}{k_B T \Omega} = \frac{\phi}{N} \ln \phi + (1 - \phi) \ln (1 - \phi) + \chi \phi (1 - \phi) + \frac{1}{24\pi\xi^3}. \quad (1.47)$$

Note that the volume of the system Ω is equivalent to the number of total sites n_{tot} in Eq. 1.26. In the mean field theory framework, if the system falls under the concentrated regime, the free energy contribution $1/24\pi\xi^3$ arising due to monomer density fluctuations is of the order of $\phi^{3/2}$ which is smaller in comparison to other terms which are of the order of $\mathcal{O}(\phi^2)$. This contribution can thus be ignored. In this case, the free energy approximately is,

$$\frac{\Delta F}{k_B T} \sim \Omega \phi^2 \sim R_c^3 \left(\frac{N}{R_c^3} \right)^2 \sim \frac{N^2}{R_c^3}, \quad (1.48)$$

where N is the number of polymer segments in the solution and R_c is the size of the confinement. This expression changes if the chain length is such that the segment concentration falls under within semi-dilute regime. The fluctuation term $1/24\pi\xi^3$ then becomes of the order of $\phi^{9/4}$ and contributes significantly in comparison to

other $\mathcal{O}(\phi^2)$ terms and the free energy can be approximated as,

$$\frac{\Delta F}{k_B T} \sim \frac{\Omega}{\xi^3} \sim R_c^3 \left(\frac{N}{R_c^3} \right)^{9/4} \sim \frac{N^{9/4}}{R_c^{15/4}}. \quad (1.49)$$

Hence, the free energy function under confinement given by Eq. 1.47 is a concentration dependent crossover function which has two different limits in the concentrated (Eq. 1.48) and semi-dilute regime (Eq. 1.49).

1.7 The Stem Cell

A cell is the basic structural, functional and biological unit of all known living organisms [Alberts et al., 2013]. Cells can be prokaryotic or eukaryotic. Prokaryotic cells are those in which nuclei are absent. Prokaryotes include two of the three domains of life, bacteria and archaea. Eukaryotic cells possess a nucleus as well as other membrane-bound structures called organelles. These include the endoplasmic reticulum (ER), the golgi complex, lysosomes, mitochondria, microbodies and vacuoles [Alberts et al., 2013]. Plants, animals, fungi, protozoa and algae are all examples of eukaryotes.

Stem cells are undifferentiated cells that can differentiate into specialized cells and can divide while maintaining differentiated state [Alberts et al., 2013]. The definition of stem cell requires the specification of both potency and of the property of self-renewal. The ability to go through numerous cell-cycles while maintaining the undifferentiated state is called self-renewal. The ability of the stem cell to differentiate into various different specialized cells is termed as potency.

Depending upon where they are sourced from, stem cells can be mainly classified into three types: embryonic stem cells, obtained from a 4 to 6 days old embryo, adult stem cells, obtained from tissues in the adult and induced pluripotent stem cells, derived

from an adult cell by introducing a specific set of pluripotency "reprogramming factors" into a given cell type [Takahashi and Yamanaka, 2006]. Stem cells can also be categorized on the basis of their potency. The Zygote and the cells of first few cycles are the most potent stem cells as they can differentiate into all kinds of specific cell types. They are called totipotent stem cells. On the other hand, pluripotent stem cells have the ability to differentiate into almost all kinds of stem cells, but not all possible cell types. Cells which can differentiate into a restricted family of cell types are called multipotent stem cells. For example, a hematopoietic stem cell that could differentiate into a WBC, RBC or platelets, is a multipotent stem cell.

Stem cells differentiate into specific cells, according to the environment and the stimuli they receive. The mechanical properties of stem cells differ from those of a differentiated cell. Experiments [Chowdhury et al., 2010, Pajerowski et al., 2007] show that mechanically undifferentiated cells nuclei are less stiffer than those of differentiated ones. The fact that differentiated and undifferentiated cells have different stiffness and flexibility indicates that the nature of chromatin organization in these cells may play a role in their properties. Experiments [Pagliara et al., 2014] find that the nuclei of mouse embryonic stem cells exiting the pluripotent state have a negative Poisson's ratio, exhibiting an expansion in the lateral direction upon stretching and a lateral contraction upon compression. Materials which exhibit a negative Poisson's ratio are termed as auxetic materials. In chapter 3, we explain this phenomenon by deriving a dynamical systems model in which we couple nuclear dimensions to states of chromatin compaction and make a number of specific predictions for experiments.

The nucleus is a membrane enclosed organelle containing most of the cell's genetic material, organized as multiple long linear DNA molecules complexed with a large variety of proteins including packaging proteins called histones. The combination of DNA with bound histones is called chromatin. It is believed that, in stem cells,

highly active chromatin continually exchanges a fraction of bound histones with an unbound or loosely bound pool of histones and other associated proteins (see Figure 3.1(b)). This is described by saying that chromatin is hyperdynamic [Meshorer et al., 2006].

A section of DNA which encodes the synthesis for protein or RNA is called gene. During the process of gene expression, information from the gene sequence is used in the synthesis of these gene products. This process involves two steps: transcription and translation. The first step in which gene's DNA is copied into messenger RNA (mRNA) using an enzyme called RNA polymerase, is called transcription. During the second step, mRNA is used to synthesize proteins with the help of ribosomes. This process of synthesizing the protein from RNA is called translation. A good fraction of genes are inactive for most of the life time of the cells and their expression is tightly regulated so that they are expressed only when the corresponding gene products are needed [Alberts et al., 2013]. A cell regulates its gene expression depending upon internal and external stimuli and the specific type.

1.8 Summary

In this chapter, we discussed various polymer models. First, we discussed the ideal chain polymer model in which the bond length is constant and more than one monomer can occupy one lattice point. In this model R_g of the polymer scales as $N^{1/2}$. The shortcoming of constant bond length is corrected by embedding the Gaussian behavior to bond length. The self-avoiding chain model is discussed where the overlap of the monomers onto each other is prohibited.

Subsequently, we discussed polymers in confinement. When the polymer is restricted to a confined space, the number of conformations a polymer can assume is reduced. The free energy of confinement depends upon the shape and size of the confinement.

Three different approaches are taken to solve the problem of confinement. In an analytical approach, a polymer chain was confined to the interior of a sphere, the diffusion equation is solved analytically and the corresponding free energy was written down. Second, we used scaling arguments to derive free energy expression for a polymer confined in a cylindrical tube. Finally, in a thermodynamic approach, the Flory-Huggins theory of polymer was used to derive the expression for free energy. At the end, a brief summary of the stem cell and the related biological terms was provided. These terms will be used in chapter [3](#).

Chapter 2

Methods

There are various ways to understand the behaviour of a polymer system. In this thesis, we discuss, two of them; one is through a theoretical approach which we discussed earlier in chapter 1 and the other is through a computational approach, based on molecular dynamics simulations, which we discuss in this chapter. Molecular dynamics (MD) simulations were first introduced by Alder and Wainwright [[Alder and Wainwright, 1957](#), [Alder and Wainwright, 1959](#)] to study the phase transition of a hard sphere system. Today, a number of advancements have been made in terms of techniques and computational power so that we can solve far more complex problems with molecular dynamics.

2.1 Molecular Dynamics: The Basic Idea

Molecular dynamics simulations allow us to determine the motion of constituent particles which interact with each other through an interaction potential. The time evolution of the particles position is obtained by solving Newton's equations of motion. MD simulations provide the microscopic picture of the system from which the macroscopic properties of the system can be measured.

Let's take a system of N particles which interact with each other via a potential $U(r_i)$, where i is the index for each particle. The force (F_i) exerted on i^{th} particle can be written as,

$$F_i = -\nabla U(r_i). \quad (2.1)$$

The above expression can also be written in terms of mass m and acceleration $\frac{d^2r}{dt^2}$ of the particle,

$$m_i \frac{d^2 r_i}{dt^2} = -\nabla U(r_i). \quad (2.2)$$

Solving the above equations along with the appropriate boundary conditions and initial condition yields the trajectory of the particle over a period of time.

2.1.1 Force Field and Equations of Motion

The force field is a collection of equations and parameters which are used to reproduce the molecular geometry and properties of the system. Most force fields are empirical and consist of both bonded potentials which include chemical bonds, bond angles, dihedrals and improper angles, and non-bonded potentials which include van der Waals and electrostatic forces. The parameters are obtained either from ab-initio semi-empirical quantum mechanical calculations or by fitting the experimental data. A typical force field which comprises bonded and non-bonded interactions is,

$$U = U_{bond} + U_{non-bond}, \quad (2.3)$$

$$\begin{aligned}
U = & \sum_{\text{bonds}} \frac{1}{2} k_b (r - r_0)^2 + \sum_{\text{angles}} k_\theta (\theta - \theta_0)^2 + \sum_{\text{dihedrals}} k_\phi [1 + \cos(n\phi + \delta)] \\
& + \sum_{\text{improvers}} k_\psi (\psi - \psi_0)^2 + \sum_i \sum_{j \neq i} 4\epsilon_{ij} \left[\left(\frac{\sigma_{ij}}{r_{ij}} \right)^{12} - \left(\frac{\sigma_{ij}}{r_{ij}} \right)^6 \right] \\
& + \sum_{\text{elec}} \frac{q_i q_j}{4\pi\epsilon_0 \epsilon_r r_{ij}}, \quad (2.4)
\end{aligned}$$

where the first four terms are the contribution from two body interaction potential (bond), three body interaction potential (angle) and four body interaction potentials (dihedral and improper) and the last two term are van der Waals and electrostatic interaction.

2.1.2 Bonded Interaction

The first part in Eq. 2.4 is the bond energy due to the interaction between two adjacent particles which are chemically bonded (see Figure 2.1 (a)). The simplest and most common choice for bonded interaction is the harmonic potential $\frac{k_b}{2}(r-r_0)^2$. The r_0 is the equilibrium bond length and k_b is the force constant. The next term in the equation represents the energy associated with the angle θ_{ijk} made by two adjacent bonds (Figure 2.1 (b)). The θ_0 is the equilibrium angle and k_θ is the force constant associated with the bond angle. The third term in the Eq. 2.4 is associated with the 4 body torsional interaction. The k_ϕ is the torsional force constant and ϕ_{ijkl} is the angle between the planes formed by i, j and k molecules and j, k and l molecules (Figure 2.1 (c)), the integer constant n is non-negative and indicates the periodicity and δ is the phase shift angle. The fourth term in Eq. 2.4 is the improper angle potential which is used to give the system a correct chirality. The improper angle ψ is the angle between the bond lj and the plane formed by ijk (Figure 2.1 (d)), ψ_0 is the equilibrium value of ψ and k_ψ is the stiffness of the potential.

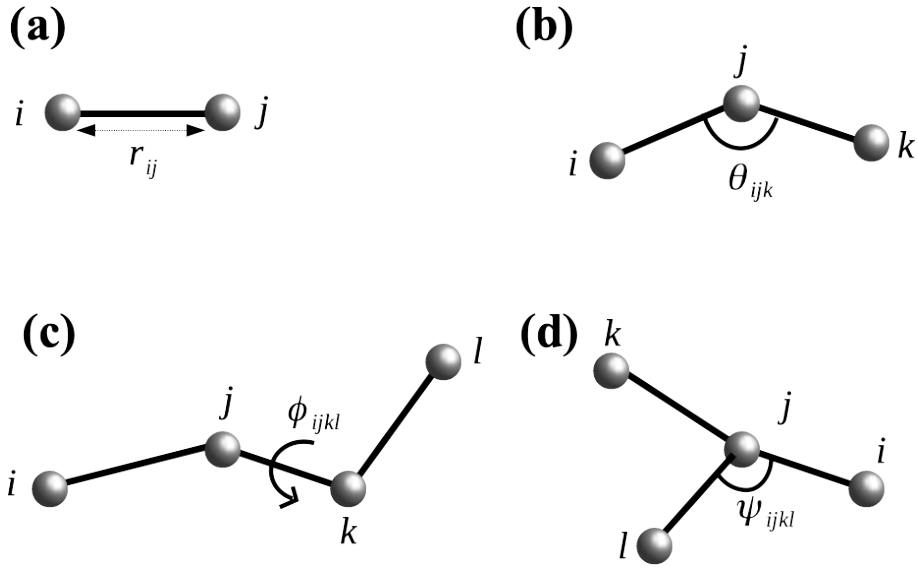


Figure 2.1: Schematic description of different bonded interactions and the parameters involved.

2.1.3 Non-Bonded Interaction

The non-bonded interaction includes Lennard-Jones potential and Coulomb electrostatic potential. The Lennard-Jones potential is an intermolecular pair potential which has been studied extensively. It consists of a repulsive interaction term $1/r^{12}$ which describes the Pauli repulsion due to overlapping of electron orbitals and an attractive interaction term $-1/r^6$ to mimic the attraction at long range (see Figure 2.2). The force due to this potential can be repulsive or attractive depending upon the value of intermolecular separation r_{ij} . To include the strength of the attraction/repulsion a parameter ϵ_{ij} is used while σ_{ij} is related to the molecular size. The $1/r^6$ interaction term is long range in power law but in order to save computing time, it is generally truncated at a cut-off distance $r_c = 2.5\sigma$ (σ is the length scale of the system) and shifted to avoid discontinuity in potential energy at the cut-off distance. The other non-bonded potential is Coulomb interaction potential where q_i and q_j are the charges of the i^{th} and j^{th} particle, ϵ_0 is the electric permittivity of vacuum and ϵ_r is the permittivity of the medium. The Coulomb potential is long range and can be computed with a cut-off as in case of LJ potential but $1/r$ ap-

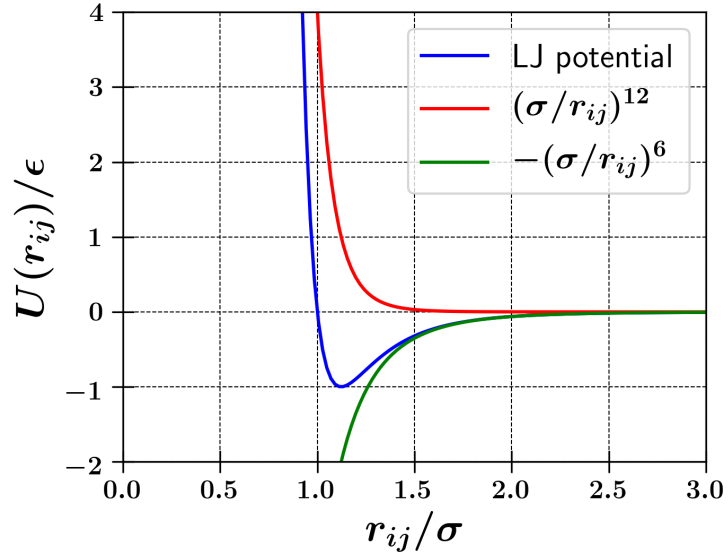


Figure 2.2: LJ interaction potential (blue) is a combination of a repulsive ($1/r^{12}$) (red) and an attractive $-(1/r^6)$ part (green).

proaches 0 slower than $1/r^6$. Hence, special techniques such as Particle Mesh Ewald (PME) [Ewald, 1921] and Fast Multipole Method (FMM) are employed to calculate it [Frenkel and Smit, 2001]. In this thesis, we explored the neutral polymers using the molecular dynamics simulation, hence no electrostatic computation is carried out in chapter 4.

Now in order to describe the motion of the system, we write down the equations of motion,

$$m_i \frac{d^2 r_i}{dt^2} = -\frac{\partial}{\partial r_i} U(r_1, r_2, \dots, r_N), \quad (2.5)$$

This is a system of N second order coupled differential equations.

2.1.4 Solution of Equation of Motion

The interaction potential function $U(r_i)$ is a function of $3N$ atomic positional coordinates. Hence, solving the equation of motion analytically is not possible and we solve it numerically along with the initial conditions. There are many algorithms available to integrate the equations of motion. Some conditions are met while choosing integration algorithm, it should conserve the energy, should be reversible, computationally efficient and allow for a long integration time step. Some of the commonly used algorithms are discussed below.

Euler Algorithm

This is, perhaps, the most simple algorithm to integrate the equations of motion. The trajectory is calculated as following,

$$\mathbf{r}(t + \delta t) = \mathbf{r}(t) + \dot{\mathbf{r}}(t)\delta t + \frac{1}{2}\ddot{\mathbf{r}}(t)\delta t^2 + \mathcal{O}(\delta t^3), \quad (2.6)$$

$$\mathbf{v}(t + \delta t) = \mathbf{v}(t) + \dot{\mathbf{v}}(t)\delta t + \mathcal{O}(\delta t^2), \quad (2.7)$$

The Euler algorithm is neither time-reversible nor phase-space preserving and hence not preferred.

Verlet Algorithm

This is one of the most commonly used integration algorithm which was introduced by Verlet 1967 [Verlet, 1967]. We write two Taylor series expansions for $\mathbf{r}(t)$, one forward in time and other backward in time.

$$\mathbf{r}(t + \delta t) = \mathbf{r}(t) + \dot{\mathbf{r}}(t)\delta t + \frac{1}{2}\ddot{\mathbf{r}}(t)\delta t^2 + \frac{1}{3!}\dddot{\mathbf{r}}(t)\delta t^3 + \mathcal{O}(\delta t^4), \quad (2.8)$$

$$\mathbf{r}(t - \delta t) = \mathbf{r}(t) - \dot{\mathbf{r}}(t)\delta t + \frac{1}{2}\ddot{\mathbf{r}}(t)\delta t^2 - \frac{1}{3!}\dddot{\mathbf{r}}(t)\delta t^3 + \mathcal{O}(\delta t^4). \quad (2.9)$$

Adding Eq. 2.8 and Eq. 2.9 together yields,

$$\mathbf{r}(t + \delta t) = 2\mathbf{r}(t) - \mathbf{r}(t - \delta t) + \ddot{\mathbf{r}}(t)\delta t^2 + \mathcal{O}(\delta t^4). \quad (2.10)$$

It is to note that this position at time $t + \delta t$ depends upon the position at two previous time steps t and $t - \delta t$. The error associated with the $\mathbf{r}(t)$ is of the order of δt^4 . The Verlet algorithm does not use velocity to update the position of particles, however it can be derived from the knowledge of position co-ordinates of the particles. From central difference, the velocity at time t can be written as,

$$\mathbf{v}(t) = \frac{\mathbf{r}(t + \delta t) - \mathbf{r}(t - \delta t)}{2\delta t} + \mathcal{O}(\delta t^2). \quad (2.11)$$

We see from Eq. 2.11 that the error associated with the $\mathbf{v}(t)$ is of the order of δt^2 rather than δt^4 . The velocity of a particle at time t is computed only when we know its position at time $t + \delta t$. The velocity does not appear explicitly in the Verlet algorithm which makes it inaccurate to implement e.g. temperature control. In order to start a calculation, we generally know the position of the particle and the velocity it has but knowing these two values is not enough to start this algorithm. The problem of accuracy and need to store positions of two previous time steps can be solved using other modified algorithms such as Leap-Frog Verlet [Frenkel and Smit, 2001] and Velocity-Verlet Algorithms.

Leap-Frog Algorithm

The slope of a function between two points is a much better approximation of the derivative at the midpoint, than at either end. In this method, we use the following approximation,

$$\mathbf{r}(t + \delta t) = \mathbf{r}(t) + \dot{\mathbf{r}}(t + \delta t/2)\delta t, \quad (2.12)$$

$$\mathbf{v}(t + 3\delta t/2) = \mathbf{v}(t + \delta t/2) + \dot{\mathbf{v}}(t + \delta t)\delta t. \quad (2.13)$$

The velocities are updated at half time steps and leap ahead the position coordinates. The current velocities can be written as,

$$\mathbf{v}(t + \delta t) = \frac{(\mathbf{v}(t + \delta t/2) + \mathbf{v}(t + 3\delta t/2))}{2}. \quad (2.14)$$

The error in Leap-Frog method are of the order of δt^2 .

Velocity-Verlet Algorithm

Velocity-Verlet algorithm [Swope et al., 1982] has improved accuracy compared to Verlet algorithm. To derive the velocity-Verlet algorithm, the Taylor expansion of the position co-ordinates as well as velocity and the first derivative is written as,

$$\mathbf{r}(t + \delta t) = \mathbf{r}(t) + \dot{\mathbf{r}}(t)\delta t + \frac{1}{2}\ddot{\mathbf{r}}(t)\delta t^2 + \mathcal{O}(\delta t^3), \quad (2.15)$$

$$\mathbf{v}(t + \delta t) = \mathbf{v}(t) + \dot{\mathbf{v}}(t)\delta t + \frac{1}{2}\ddot{\mathbf{v}}(t)\delta t^2 + \mathcal{O}(\delta t^3), \quad (2.16)$$

$$\dot{\mathbf{v}}(t + \delta t) = \dot{\mathbf{v}}(t) + \ddot{\mathbf{v}}(t)\delta t + \mathcal{O}(\delta t^2), \quad (2.17)$$

Rearranging Eq. 2.17 and multiplying both sides by $\delta t/2$ yields,

$$\ddot{\mathbf{v}}(t) \frac{\delta t^2}{2} = \frac{\delta t}{2} [\dot{\mathbf{v}}(t + \delta t) - \dot{\mathbf{v}}(t)] \quad (2.18)$$

Substituting the value of $\ddot{\mathbf{v}}(t) \frac{\delta t^2}{2}$ in Eq. 2.16 gives,

$$\mathbf{v}(t + \delta t) = \mathbf{v}(t) + \frac{\delta t}{2} [\dot{\mathbf{v}}(t + \delta t) + \dot{\mathbf{v}}(t)] + \mathcal{O}(\delta t^3) \quad (2.19)$$

Replacing $\dot{\mathbf{r}} = \mathbf{v}$ and $\dot{\mathbf{v}} = \mathbf{a}$ in Eq. 2.15 and 2.19 leads to the final velocity-Verlet algorithm,

$$\begin{aligned} \mathbf{r}(t + \delta t) &= \mathbf{r}(t) + \delta t \mathbf{v}(t) + \frac{\delta t^2}{2} \mathbf{a}(t) \\ \mathbf{v}(t + \delta t) &= \mathbf{v}(t) + \frac{\delta t}{2} [\mathbf{a}(t) + \mathbf{a}(t + \delta t)]. \end{aligned} \quad (2.20)$$

This algorithm has an error of the order of δt^3 in position as well as velocity. As the equations in this algorithm computes both the position and velocity, it is self starting unlike Verlet algorithm which yielded only the position from two previous steps.

2.2 Ensembles

An ensemble is a collection of a large number of microscopically different replicas of a system having statistically similar macroscopic properties. The ensemble formalises the idea that experiments may give similar macroscopic outcomes even if the microscopic details are not same. There are different types of ensembles and what ensemble to choose for the simulation depends upon the system specifics and the quantities of interest. Three most important ones are microcanonical, canonical and grand canonical ensembles.

The microcanonical ensemble, also known as NVE ensemble has the number of particles N , the volume V and the energy E of the system constant. This ensemble is useful for a system which is isolated from its environment (heat bath). When the system is not isolated and is in contact with its environment, it can exchange energy and keep the temperature constant. In this case, the canonical ensemble is used. In this ensemble, systems have number of particles N , volume V and temperature T constant. On the other hand, a grand canonical ensemble is used when a system is open (free to exchange particles) and in contact with the environment, it will have the chemical potential μ , volume V and temperature T constant.

2.3 Thermostats and Barostats

In molecular dynamics simulation, only integrating the equations of motion yields microcanonical ensemble as the energy is conserved. In order to perform simulations under the conditions of constant temperature and/or constant pressure, modifications are done to the Newton's equations of motion. A brief introduction to such methods is following,

Andersen Thermostat

Andersen proposed this thermostat in 1980 [[Andersen, 1980](#)] which allowed the simulations under constant temperature for the first time. This thermostat couples the system with a heat bath and a randomly chosen particle is imparted a momentum which is chosen from Boltzmann distribution at temperature T . The time between the collision is decided randomly following Poisson's distribution. This thermostat cannot be used for calculating diffusion coefficients as it destroys the momentum transport because of random velocities.

Thermostat using velocity rescaling

In this method, the velocities are rescaled to keep temperature constant without allowing for any fluctuation in temperature.

$$v_i \rightarrow \sqrt{\frac{T_0}{T}} v_i, \quad (2.21)$$

where T_0 is the desired temperature and T is the instantaneous temperature calculated from the velocities of the particles. This method leads to discontinuities in the momentum of the particles due to rescaling.

Berendsen Thermostat

In canonical ensemble, the instantaneous temperature of the system fluctuates about the desired temperature which Gaussian thermostat does not allow. In order to overcome this problem arising from the rescaling method, Berendsen Thermostat [Berendsen et al., 1984] was introduced. The velocities are rescaled such that the rate of change of temperature depends upon the difference between the instantaneous temperature of the system and the desired temperature.

$$\frac{dT}{dt} = \frac{1}{\tau}(T_0 - T), \quad (2.22)$$

where τ is coupling parameter determining how tightly the heat bath and the system is coupled.

Lagrangian Thermostat

In this method, the particle is assumed to be moving in a sea of fictional smaller particles. The smaller particles create a damping force $-\gamma p_i$ on the particle, where γ is frictional coefficient and p_i is the momentum of the particle. Also, the smaller parti-

cles have their own kinetic energy and they collide and randomly impart momentum to the particle. Hence, the equation of motion is,

$$m \frac{d^2 r_i}{dt^2} = -\nabla U(r_i) - m\gamma \frac{dr_i}{dt} - R_i(t), \quad (2.23)$$

where $R_i(t)$ is the random force due to the collision of the smaller particles. As this thermostat mimics the viscous aspect of the solvent, it is used in such solute-solvent systems where the behavior of solvent is non-interesting and the behavior of solute is desired (such as proteins, DNA in a solvent etc.).

Nosé–Hoover Thermostat

It is one of the most accurate and efficient method to perform constant temperature molecular dynamics simulations. It was developed by Nosé [Nosé, 1984] and further modified by Hoover [Hoover, 1985]. Nosé–Hoover Thermostat uses a deterministic algorithm where it adds an additional degree of freedom (s) which gives an effect of heat bath. The Lagrangian of the extended system is given by,

$$L = \sum_{i=1}^N \frac{m_i}{2} s^2 \dot{q}_i^2 - U(q) + \frac{Q}{2} \dot{s}^2 - g k_B T \ln s, \quad (2.24)$$

where m_i is the mass, q_i is the coordinate of i^{th} particle, Q is the mass associated with s , and g is the number of degrees of freedom of the system. Using the Lagrangian of the system, the equation of motion can be written down as below,

$$\begin{aligned} \frac{dq_i}{dt} &= \frac{p_i}{m_i s^2}, \\ \frac{dp_i}{dt} &= -\frac{\partial U}{\partial q_i}, \end{aligned}$$

$$\begin{aligned}\frac{ds}{dt} &= \frac{p_s}{Q}, \\ \frac{dp_s}{dt} &= \frac{\sum \frac{p_i}{m_i s^2} - gk_B T}{s},\end{aligned}$$

where p_i and p_s are momenta conjugate to q_i and s .

Berendsen Barostat

Most experiments are done under constant pressure rather than constant volume. Thus in order to mimic the experimental conditions, simulations need to have a constant pressure as well which is achieved using a suitable barostat. The Berendsen barostat [Berendsen et al., 1984] is very similar to Berendsen thermostat. The instantaneous pressure P of the system is rescaled in such a way that,

$$\frac{dP}{dt} = \frac{1}{\tau}(P_0 - P), \quad (2.25)$$

where P_0 is the desired pressure and τ is the coupling constant similar to what was used in Berendsen thermostat. This rescaling of pressure leads to the change in cell dimension which is corrected by a factor η ,

$$\eta = 1 - \frac{\Delta t}{\tau} \gamma (P_0 - P), \quad (2.26)$$

where Δt is integration time step and γ is the isothermal compressibility of the system.

2.4 Ergodic Hypothesis

With MD simulations, one calculates the time averages of an observable, but experiments are supposed to provide ensemble average of the observable. The ergodic hypothesis states that the time average of an observable is equal to its ensemble average with probability one.

$$\langle A \rangle_{time} = \langle A \rangle_{ensemble}. \quad (2.27)$$

The assumption behind this is that if we let the system evolve in time, it will cover all the phase space and take all the conformations. As the simulations are carried out for a finite time, the systems do not have enough time to cover all the possibilities and do not obey ergodicity. In molecular dynamics, for the calculation purposes, systems are assumed to be ergodic [Calvo et al., 2002].

2.5 All Atom vs Coarse Grained Model

The most fundamental and accurate model of the matter is which invokes quantum mechanics. In this approach, Schrödinger equation is needed to be solved for all the sub-atomic particles in the system. Computationally, many approximations are made in order to solve it, even then it is limited to a small number of particles. Solving a larger system with such great detail is neither computationally practical nor needed as often the phenomenon we are interested in are manifested on a larger length and time scales. As the length and time scales of the different systems differ orders of magnitude, the details we need to input in the simulations vary significantly. When one moves to the larger scales, a coarse-grained model is used to describe the system. In these models pseudo-atoms are defined which are group of atoms. The number of atoms in a pseudo-atom depends upon the length scale of the system

we are interested in. These coarse-grained models are derived from the atomistic models and are computationally much less expensive.

2.6 Software Packages

In order to make implementation of various algorithms used in the integration of Newton's equations and thermostats/barostats, easier and faster, various software packages are available. The suitability of a package depends on the problem and the features of the package. For example, for all atom simulations, NAMD package [Phillips et al., 2005] can be used and for coarse grained system LAMMPS [Plimpton, 1995] or GROMACS [Van Der Spoel et al., 2005] can be utilized. For the results presented in chapter 4, LAMMPS package is utilized for the coarse grained simulations. LAMMPS stands for Large-scale Atomic/Molecular Massively Parallel Simulator and is distributed by Sandia National Laboratories, a US Department of Energy laboratory. It is an open-source code written in C++/Python under the terms of the GPL. It runs on single processors or in parallel using message-passing techniques and a spatial-decomposition of the simulation domain. In this thesis, LAMMPS was used to perform all the simulation presented in chapter 4.

There are various tools available for the visualization of the trajectory generated at the end of the simulations. For example OVITO [Stukowski, 2010], VMD [Humphrey et al., 1996] and PIZZA.PY. Some of the packages have analytical capabilities along with the visualization capability. I used VMD package in the visualization and also some of the analysis was done using custom tcl scripts in VMD.

Chapter 3

Chromatin Compaction, Auxeticity and the Epigenetic Landscape of Stem Cells

Measurements of the deformability of cell nuclei in the transitional state that intervenes between the embryonic stem cell state and the differentiation primed state of mouse stem cells indicate that such nuclei are *auxetic i.e.* have a negative Poisson's ratio. We show, using a theoretical model, how this remarkable mechanical behaviour results from the coupling between chromatin compaction states and nuclear shape. Our model yields a biophysical interpretation of the epigenetic landscape of stem cells, also suggesting how this landscape might be probed experimentally. This chapter is based on the work presented in Ref. [[Tripathi et al., 2019](#)].

3.1 Introduction

Embryonic stem cells (ES cells) occupy the apex of a hierarchy of cellular states [[Young, 2011](#)]. They can self-renew, maintaining their "stemness", but also differentiate into

varied cellular lineages when supplied with appropriate biochemical or mechanical cues. This is the property of pluripotency [Suda et al., 1987, Heo et al., 2018]. Cell lineage choice results from shifts in patterns of gene expression, controlled by the rewiring of gene regulatory networks. Such rewiring can arise because the transcription factors that control the production of RNA are present at different levels in different cell types. But such shifts can also occur through biochemical changes at the DNA level, such as the methylation of cytosine residues, as well as through modifications in histone and other architectural proteins that bind DNA [Berger, 2007, Hawkins et al., 2010]. Such epigenetic modifications, termed thus because they do not affect DNA sequence, alter the local structure and biophysical properties of chromatin, the term applied to DNA in its natural state in the nuclei of living cells.

Changes in patterns of gene expression should have biophysical correlates, since they require actively transcribed genes to be more accessible than silenced genes [Rando and Chang, 2009]. Regions of chromatin which see higher levels of transcriptional activity are typically more loosely packed (euchromatin) than gene poor and relatively more compact (heterochromatin) regions. These regions can be identified through local epigenetic marks [Narlikar et al., 2002]. The local state of chromatin compaction is clearly relevant to the biophysics of chromatin. It may assume added importance in the highly dynamic stem cell state since ES cells are known to be transcriptionally hyperactive [McNally, 2011, Efroni et al., 2008]. In addition, ES cell chromatin is “hyperdynamic”, with histones binding and unbinding locally at an enhanced rate compared to differentiated cells [Meshorer et al., 2006]. This increased rate of binding and unbinding leads to larger fluctuations in chromatin packaging. Stem cell chromatin is thus more fluid-like than the chromatin of differentiated cells. Such fluidity likely contributes to the maintenance of pluripotency [Gaspar-Maia et al., 2011].

Before lineage commitment, ES cells exhibit decondensed chromatin and soft nuclei. A slowing down of histone dynamics, a stiffening of the nuclear envelope and global chromatin remodelling all accompany differentiation. This results in a transition between a more open chromatin configuration to a more compact state [Engler et al., 2006, Justin and Engler, 2011, Evans et al., 2009, Chen and Dent, 2014, Ugarte et al., 2015]. The interplay of chromatin packaging with fluctuations of the relatively pliable chromatin-enclosing nuclear envelope might reasonably be expected to underly the special biophysical properties of the stem cell nucleus [Bošković et al., 2014, Dado et al., 2012]. Purely mechanical cues, such as substrate stiffness or substrate structure, are sufficient to drive stem cell differentiation into preferred lineages [Engler et al., 2006, Yim and Sheetz, 2012, Hwang et al., 2013]. This suggests a biophysical link between nuclear mechanics, chromatin packaging and lineage choice.

Waddington originally visualised the differentiation of stem cells in terms of a set of branching tracks representing different cell fate choices [Waddington, 1947]. A subsequent, more pictorial version of this idea used the analogy of a ball rolling along an "epigenetic landscape" with minima chosen to represent stable differentiated states [Gilbert, 2000, Waddington, 2014]. Stable positions in this landscape have been argued to correspond to attractors of a high-dimensional nonlinear dynamical system controlled by feedback [Huang, 2012]. This provides a particularly appealing and pictorial way of understanding how stem cell differentiation into specific cell lineages can be visualized. Such ideas connect naturally to other landscape descriptions of biophysical states and phenomena [Kauffman, 1992, Onuchic et al., 1997]. However, the experimental corollaries of an epigenetic landscape and how, in particular, nuclear mechanics might enter its description, are little understood.

We ask whether recent biophysical measurements of the mechanical properties of stem cell nuclei can provide insights into these broader questions [Miroshnikova

et al., 2017, Chalut et al., 2012, Swift and Discher, 2014]. We first note that almost all materials have a positive Poisson’s ratio, becoming wider in the transverse direction when compressed uniaxially along a longitudinal dimension [Landau and Lifshitz, 1986, Chaikin et al., 1995]. Materials with a negative Poisson’s ratio, among them foams, are termed auxetics [Evans and Alderson, 2000, Grima et al., 2006]. Pagliara *et al.* [Pagliara et al., 2014] report results from atomic force microscopy (AFM) measurements of the reduced modulus $K = E/(1 - \nu^2)$, with E the uniaxial stiffness and ν the Poisson’s ratio, of naive mouse embryonic stem cell (N-ESC) nuclei exiting the pluripotent state *en route* to differentiation via a transitional state (T-ESC) and a differentiation primed (P) state. In the transitional state, obtained when specific inhibitors preventing the transition to a differentiation primed state are removed, the cell nuclei were noticed to become smaller by about 5-10% in cross section when compressed to the level of about $2 \mu\text{m}$ with the AFM probe [Pagliara et al., 2014]. Similar results were obtained by observing changes in nuclear dimensions when cells in the T-ESC state were set in flow along a microchannel. Whereas both the N-ESC as well as the P states exhibit a positive Poisson’s ratio, the T-ESC state that intervenes between them is thus auxetic, with a *negative* Poisson’s ratio. Pagliara *et al.* suggest that the auxetic phenotype might be connected to chromatin de-condensation, since chromatin in the transitional state is less condensed than in either the embryonic stem cell state or the differentiation primed state [Pagliara et al., 2014]. Disrupting the actin cytoskeleton through Cytochalasin D treatment did not remove auxeticity, indicating that it might naturally originate in the biophysical properties of the nucleus itself and not of the extranuclear environment.

The model we describe here [Tripathi and Menon, 2019] addresses these experiments, placing them in a wider context of our understanding of the epigenetic landscape of stem cells. It uses four biophysical assumptions. These follow from the experimental observations. First, the nucleus in the auxetic regime is compressible, a fundamental property of the auxetic state [Huang and Chen, 2016, Ren et al., 2018].

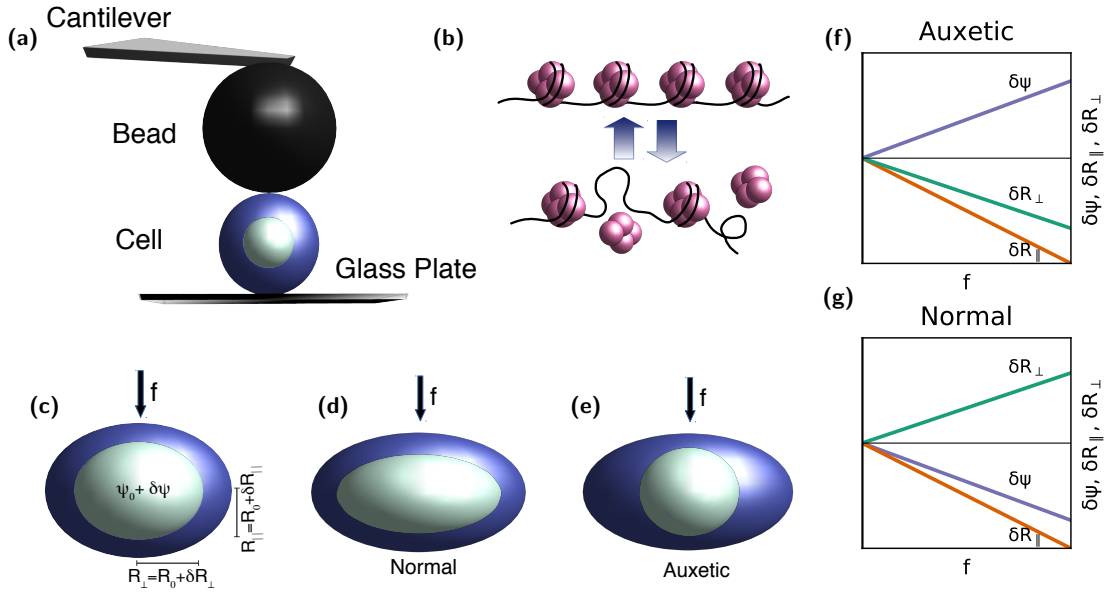


Figure 3.1: (a) Schematic of the AFM experiment of Ref. [Pagliara et al., 2014] (b) Fluctuations in chromatin compaction arising from the fast on-off dynamics of nucleosomes in the stem cell state, where histones are hyperdynamic (c) Definitions of the variables Ψ , R_{\parallel} , and R_{\perp} in the AFM-based indentation experiment, including the applied force f arising from the indentation (d) Illustration of normal *i.e.* non-auxetic behaviour in the experiments, showing how the nucleus expands in the direction perpendicular to the applied force f , while the nuclear dimension in the direction parallel to the force contracts. (e) Illustration of auxetic behaviour, showing how the nucleus contracts both in the direction perpendicular to the applied force as well as in the direction parallel to it. The schematic plots in (f) for the non-auxetic case and (g) for the auxetic case show how the variables Ψ , R_{\parallel} , and R_{\perp} behave in both limits as f is increased from zero. The unperturbed nucleus is taken to be spherical.

Second, mechanical response to a uniaxial external force in such a regime must distinguish between directions parallel to the force and perpendicular to it, although such anisotropy need not be intrinsic to isolated stem cells in the absence of an applied force [Alderson et al., 2005]. Third, a number of experiments indicating chromatin fluidity in all but terminally differentiated states argue that chromatin is best described as a confined, active polymer fluid in a semi-dilute regime [Pajeroski et al., 2007]. (Indeed, the formation of heterochromatin foci has been discussed in analogy with active phase separation in liquid-liquid mixtures [Larson et al., 2017, Strom et al., 2017].) An alternative view of auxeticity which considers the nucleoplasm to

be a gel and uses ideas from phase separation is described in Ref. [Yamamoto and Schiessel, 2017]. We will treat activity as equivalent to a (higher) effective temperature [Ganai et al., 2014, Agrawal et al., 2017, Agrawal et al., 2018]. Fourth and finally, we assume that auxetic behaviour arises from the form of the coupling of chromatin compaction states to mechanical variables, which we choose as nuclear dimensions parallel to, as well as perpendicular to, the applied force. These four assumptions, all reasonable from a biophysical standpoint, inform our mathematical model. We use them to derive a model non-linear dynamical system describing auxetic behaviour in the transitional state of stem cells.

3.2 Materials and Methods

We first identify relevant variables of interest, in particular those that are amenable to measurement. Figure 3.1(a) shows a schematic of the experiments of Ref. [Pagliara et al., 2014] while Figure 3.1(b) illustrates how the on-off dynamics of nucleosomes in the stem cell state might alter chromatin packaging. Figure 3.1(c) illustrates the definitions of the fundamental mechanical variables that enter our model. We use a single variable, labelled Ψ , to describe nucleosome-induced compaction of chromatin. The variable Ψ can be thought of as representing the number of nucleosomes bound to chromatin at a given time, with the biophysical interpretation that a larger number of bound nucleosomes yields a more compact chromatin structure. The structural variables $R_{\parallel} = R_0 + \delta R_{\parallel}$ and $R_{\perp} = R_0 + \delta R_{\perp}$ denote nuclear dimensions parallel and perpendicular to the direction of the applied force f , as shown. Figure 3.1(d)- (e) illustrate how nuclei deform under force in both the non-auxetic (d) and the auxetic (e) case. Finally. Figs. 3.1(f) and (g) supply schematics of auxetic and non-auxetic response to a force f , in the variables Ψ , R_{\parallel} , and R_{\perp} . How to derive the schematics of Figs. 3.1(f) and (g), including the behaviour of Ψ in both the auxetic and non-auxetic cases predicted by the theoretical formulation, is the

subject of this chapter.

3.2.1 Model Description

Our equations are formulated in terms of $\delta\Psi$, δR_{\parallel} and δR_{\perp} defined as in Figure 3.1 and derived below. The equations describing how these quantities change in time take the form

$$\frac{d(\delta\Psi)}{dt} = -\frac{dV(\delta\Psi)}{d\delta\Psi} + B\left(\frac{1}{2}\delta R_{\parallel} + \delta R_{\perp}\right) + \eta_{\Psi}, \quad (3.1a)$$

$$\frac{d(\delta R_{\parallel})}{dt} = -C\delta R_{\parallel} - D\delta\Psi - f_{\parallel} + \eta_R, \quad (3.1b)$$

$$\frac{d(\delta R_{\perp})}{dt} = -C\delta R_{\perp} - D\delta\Psi + f_{\perp} + \eta'_R. \quad (3.1c)$$

We have used our freedom to choose units suitably to "de-dimensionalize" the coefficients that appear in these equations. The first term on the right-hand side of each of these equations represents the independent relaxation of fluctuations away from $\{\Psi_0, R_0\}$. We assume that the $\delta\Psi$ variable relaxes subject to an effective potential $V(\delta\Psi)$. The interpretation of this term will become clearer as we proceed. The second term couples $\delta\Psi$ to the mechanical variables $R_{\parallel} = R_0 + \delta R_{\parallel}$ and $R_{\perp} = R_0 + \delta R_{\perp}$, with coefficient B ; the relative factor of 2 accounts for the 3-d geometry. This coupling appears to lowest order in the fluctuations δR_{\parallel} and δR_{\perp} . This is the simplest form that these equations could take. Their biophysical content lies in the estimates of the numerical values associated with the coefficients. More subtly, the coupling between chromatin compaction and nuclear dimensions is to be found in the cross-terms in Eq. 3.1.

In the absence of a force, R_{\parallel} and R_{\perp} are equivalent. The symmetry between them is broken only by f_{\parallel} and f_{\perp} . These forces represent both external forces as well as forces that arise from the remodelling of the extranuclear actin cytoskeleton, which can be assumed to be uniform if $f_{\parallel} = 0$. We can assume that f_{\parallel} couples primarily to

δR_{\parallel} whereas f_{\perp} couples to δR_{\perp} . In the absence of external forces, the two equations reduce to a single one. The quantity C represents a ratio of time-scales for the relaxation of the Ψ and the R variables. If Ψ_0 represents a stable state, or at least a state that evolves slowly on the time-scale of the fluctuations $\delta\Psi$, we can expand in these fluctuations. At the simplest level then, these fluctuations are subject to a harmonic potential. The case where $\delta R_{\parallel} = \delta R_{\perp} \equiv \delta R$, with $f_{\perp} = f_{\parallel} = 0$ and the $V(\delta\Psi)$ term chosen to be bistable, was studied in Ref. [Talwar et al., 2013], in the context of nuclear size oscillations in the ES state of mouse stem cells. We will use this more specific form of these equations when we identify signals of auxetic behaviour in fluctuations within the undeformed steady state. Our results suggest that signatures of the transition between auxetic and non-auxetic behaviour might be most easily seen in these fluctuations.

In Ref. [Talwar et al., 2013], in a description of enhanced fluctuations in mouse N-ESCs, $B > 0$ was assumed. The physical interpretation there was that *increasing* the size of the nucleus would expose binding sites for histones. This leads to a concomitant *increase* in Ψ which would then drive the nucleus to shrink [Talwar et al., 2013]. The coupled dynamics of the fast histone on-off rates in the hyperdynamic case with the slower fluctuations in nuclear size leads to interesting fluctuation behaviour. Such a choice of sign leads inevitably to non-auxetic behavior; see below.

Experiments show that chromatin is most decondensed in the transitional state, as opposed to either the ES state or the differentiation primed states between which it intervenes [Pagliara et al., 2014]. A further expansion of nuclear dimensions might then be expected to result in the expulsion of nucleosomes, rather than their accumulation, in this intermediate state. Incorporating this into the modelling requires that we consider the case where $B < 0$. Indeed, treating the naive pluripotent ESC state with trichostatin A, an HDAC inhibitor that globally decondenses chromatin, made the N-ESC auxetic, arguing for the connection to our modelling. We can thus

view the transition between the naive stem cell, the transitional state and the differentiation primed state in terms of a re-entrant behaviour in the sign of B . This is an experimentally testable prediction.

The on-off dynamics of histones is inherently noisy. Our equations account for such stochastic effects, represented as additive noise with standard properties, with terms represented by η_Ψ, η_R and η'_R . In general, the effects of the noise should be most significant for the fast fluctuating Ψ variable. We thus choose to retain only the Gaussian-distributed, delta-correlated η_Ψ term in our equations, setting $\eta_R = \eta'_R = 0$.

3.2.2 Derivation of model equations: R equation

Our equations are motivated in the following way, illustrated, for simplicity, in the isotropic case: Assume first that the nucleus is a sphere of radius R , prestressed by chromatin polymer pressure. Given compressibility, assume that the dominant modes of fluctuations are breathing modes, associated with an elastic energy $E_{el} = \frac{K_a}{2a_0} [(a - a_0)^2]$, which penalises changes in area a from an unstressed or even prestressed state where the area is a_0 . This term also accounts for the contribution of the actin cytoskeleton, which enters as a modified area expansion modulus K_a . Fluid flow in and out of the sphere, driven by a pressure imbalance, leads to volume changes and is resisted by a cost for deviations in the surface area from its preferred value.

Describing stem-cell chromatin as a polymer solution at an effective (active) temperature T^* , the free energy of the polymer solution in units of $k_B T^*$, is of the form $f_m(\phi) = \frac{\phi}{N} \ln \phi + (1 - \phi) \ln(1 - \phi) + \chi \phi(1 - \phi) + 1/(24\pi\xi^3)$, (see Chapter 1 for details) where ϕ is the volume fraction of the polymer and $\xi \sim \phi^{-\nu/(3\nu-1)}$ is the correlation term arising from monomer density fluctuations [Doi, 1996, Muthukumar, 2012b].

Activity enters as an effective temperature T^* . More subtly, it modifies the effective Flory term χ .

The polymer osmotic pressure follows from $\Pi = \frac{k_B T^*}{\nu_c} \left[\phi \frac{\partial f_m}{\partial \phi} - f_m \right]$, which yields $\Pi = \frac{k_B T^*}{\nu_c} \left[\frac{\phi}{N} - \ln(1 - \phi) - \phi - \chi \phi^2 \right]$ (refer to Chapter 1 for detailed derivation), where k_B is the Boltzmann constant, T^* is the effective temperature, ν_c is the monomer volume, ϕ is the volume fraction of the polymer and N is the degree of polymerization [Doi, 1996]. Physically, χ alters the relative balance of chromatin-chromatin and chromatin-solvent interactions, as manifest in the compaction state of chromatin. The effective Flory parameter χ is then tuned by the fraction of bound nucleosomes, which controls Ψ : $\chi = \chi(\Psi)$. We then have,

$$\Delta \Pi = -\frac{k_B T \phi_0^2}{\nu_c} \chi' \delta \Psi, \quad (3.2)$$

where $\chi' = \frac{d\chi}{d\Psi}$. Penalising fluctuations of the nuclear envelope from its preferred area a_0 yieldings a restoring net force of the form $F = -16\pi K_a \delta R$ and thus a pressure term

$$\Delta P = \frac{4K_a}{R_0^2} \delta R. \quad (3.3)$$

Darcy's law provides an expression for the rate of change of volume $\frac{dV}{dt} = \frac{\kappa A}{\mu L} (\Delta \Pi - \Delta P)$, where κ is the permeability (m^2), A is the area of the nucleus, μ the viscosity and L the length over which the pressure drops [Whitaker, 1986]. This yields, where we use the notation $\dot{R} = dR/dt$, $\dot{\Psi} = d\Psi/dt$,

$$\begin{aligned} \dot{R} &= -\left(\frac{4\kappa K_a}{\mu L R_0^2} \right) \delta R - \left(\frac{\kappa k_B T \phi_0^2}{\mu L \nu_c} \chi' \right) \delta \Psi, \\ \implies \dot{R} &= -C \delta R - D \delta \Psi, \end{aligned}$$

where $C = \frac{4\kappa K_a}{\mu L R_0^2}$ and $D = \frac{\kappa k_B T \phi_0^2}{\mu L \nu_c} \chi'$. Note that $D > 0$ is required by the bio-physical input that the binding of histones *must* lead to a contraction in DNA. The

larger the polymer-solvent interaction, the smaller the Flory-Huggins χ parameter implying that we can interpret histone binding and the consequent compaction of DNA as an effective decrease of the polymer-solvent interaction with histone binding. This then implies that the effective Flory-Huggins parameter should *increase* with Ψ , implying that $\chi' > 0$. Here, $\Delta\Pi - \Delta P$ provides the driving force, in this case the difference between polymer and Laplace pressures relative to their unperturbed values. This holds in the absence of a force f .

This result is easily generalized to the anisotropic case.

3.2.3 Derivation of model equations: Ψ equation

We now discuss the dynamics of $\delta\Psi$. First, ignoring the coupling to R_{\perp} and R_{\parallel} , we model fluctuations in Ψ as relaxing in an over-damped manner to Ψ_0 . This dynamics explores the one-dimensional landscape defined through the effective potential $V(\delta\Psi)$, with Ψ_0 at least a local minimum. Consider N nucleosome binding sites on a piece of DNA, in equilibrium with unbound nucleosomes at chemical potential μ , with the energy gain from nucleosome binding to DNA being ϵ . The probability of the nucleosome being bound is the Fermi function $p = 1/(1 + e^{(\epsilon - \mu)/k_B T})$, since this is an effective two state-problem at each binding site. If the radius of the confining sphere is changed from R_0 to $R = R_0 + \delta R$, the DNA will stretch in place, altering ϵ . Assuming $\epsilon = \epsilon(R)$, $\epsilon(R) = \epsilon(R_0 + \delta R) \approx \epsilon(R_0) + \epsilon' \delta R$ where $\epsilon' = \frac{\partial \epsilon}{\partial \delta R}$. Expanding $e^{-\epsilon' \delta R/k_B T} \approx 1 - \epsilon' \delta R/k_B T$, yields $\delta\Psi \approx \frac{N x_0 \epsilon' \delta R}{k_B T (1 + x_0)^2}$ where $e^{-\mu/k_B T} = \zeta$ and $\epsilon(R_0) = \epsilon_0$, $x_0 = \zeta e^{-\epsilon_0/k_B T}$. Thus, changes in R also drive changes in Ψ , which evolves to its final value, given the change δR , through a kinetic coefficient which multiplies the term above. Adding to this the term in $\delta\Psi$ coming from the epigenetic potential, which can be assumed to be quadratic at lowest order in an expansion about the stable value Ψ_0 : $V(\delta\Psi) = \frac{1}{2} A (\delta\Psi)^2$, we have our final result: $\dot{\Psi} = -A \delta\Psi + B \delta R$. A is simply the inverse of the relaxation time for compaction fluctuations τ_{Ψ} , defined be-

low. The sign of B depends on the sign of ϵ' , since all other quantities that enter its definition (N , x_0 and T) are explicitly positive, reducing to the question of whether the nucleosome binding energy is *reduced* when the nucleus is expanded. In general, as is known from *in vitro* single molecule experiments, extending DNA expels bound nucleosomes, implying that their binding energy is reduced upon stretching; thus, the sign of B should be negative for the auxetic state given our interpretation above. More details of the physical arguments are provided in next section.

3.2.4 Estimation of parameters

We now estimate $C = 4\kappa K_a / \mu L R_0^2$ and $D = \kappa k_B T \phi_0^2 / \mu L \nu_c \chi'$. We take $\kappa = l_p^2$, relating the permeability κ to the pore size l_p . Assuming a nuclear pore complex size of $l_p \simeq 5nm$ [Davis, 1995], this yields $\kappa = 2.5 \times 10^{-17} m^2$. From plate theory, the area modulus K_a and the Youngs modulus E are related through $K_a \approx Et$, [Landau and Lifshitz, 1986] where t is the thickness of the plate. Thus, $C = \frac{4\kappa K_a}{\mu L R_0^2} \approx \frac{4l_p^2 \times Et}{\mu t R_0^2} = \frac{4l_p^2 E}{\mu R_0^2}$. With $E \approx 200$ Pa [Caille et al., 2002, Guilak et al., 2000, Dahl et al., 2005], the radius of the nucleus $R_0 = 5 \times 10^{-6} m$ and $\mu \approx 2 - 3$ centi-poise $\approx 2 \times 10^{-3}$ Pa-sec, [Mastro et al., 1984] $C \approx 0.4 sec^{-1}$. To calculate D , we assume that the length over which the pressure drops is the same as the membrane thickness (65 nm [Franke, 1970]). To calculate the chromatin volume fraction, we approximate DNA as a cylinder and the histone octamer as a disc and calculate the volume of all the components. The number of base pairs in the mouse genome is approximately 3×10^9 . The average size of a basepair is approximately 3.4 [Finch et al., 1981]. Thus, the length of DNA is $(3.4 \times 10^{-10}) \times (3 \times 10^9) \sim 1$ m for the haploid case. In the case of diploid nuclei, the length of DNA ~ 2 m. Now the thickness of the DNA is 20 [Schiessel, 2003]. Approximating DNA as a cylinder, the volume of DNA is $\sim \pi R^2 L \sim 3.14 \times (400 \times 10^{-20}) \times 2 \sim 25 \times 10^{-18} m^3 = 25 \mu m^3$. As the number of basepairs per nucleosome is ~ 200 [McGhee and Felsenfeld, 1980], the number of

histone octamer cores will be $\sim (3 \times 10^9)/200 = 1.5 \times 10^7$. The histone octamer can be approximated by a disc of $110 \times 110 \times 57$ [Finch et al., 1981, Luger et al., 1997, Wang et al., 1994] $\sim 5.41 \times 10^{53}$. Thus, the volume of all the histones would be $(1.5 \times 10^7) \times (5.41 \times 10^5 \times 10^{-30})m^3 \sim 81.15 \times 10^{-19}m^3 \sim 8\mu m^3$. The total volume of chromatin \sim volume of DNA + volume of histones octamers + linker proteins (which we ignore for simplicity) $\sim 25 + 8 \sim 33\mu m^3$. Taking the nucleus to be of radius $5\mu m$, the volume of the nucleus $\sim 523\mu m^3$. Using this, the volume fraction of the chromatin is $\sim 33/523 \sim 0.06$. A reasonable value to consider is then 0.1 which we have used in our calculations. This calculation is similar to that for Arabidopsis cell nuclei in Ref. [De Nooijer et al., 2009]. With $\nu_c = (10nm)^3$ [Finch et al., 1977, Luger et al., 1997, Richmond and Davey, 2003], and $T \simeq 300$ K, we obtain $D \approx 8 \times 10^{-6}\chi' m/sec$.

3.2.5 Mapping to the experimental system

In steady state, $\delta\Psi = \frac{-Bf}{(2AC+3BD)}$, $\delta R_{\parallel} = -\frac{(2AC+2BD)f}{(2AC+3BD)C}$ and $\delta R_{\perp} = \frac{BD}{(2AC+3BD)}\frac{f}{C}$. For finiteness, we require $2AC + 3BD \neq 0$. From this, the Poisson's ratio is $\nu = -\frac{\delta R_{\perp}}{\delta R_{\parallel}} = \frac{BD}{2CA+2BD}$. Choosing the experimental value of $\nu = -0.25$ and rearranging the above expression, we find that $\frac{CA}{BD} = -3$. Making a reasonable choice for the ratio $\tau_{\Psi}/\tau_R \simeq 0.01$, yields τ_{Ψ} and the value of C obtained above yields $\tau_R = 2.5$ sec and $\tau_{\Psi} = 2.5 \times 10^{-2}$ sec, with $A = 40sec^{-1}$. From $B = -\frac{CA}{3D}$, $B = -\frac{7 \times 10^5 \times 5 \times 10^7}{3\chi'} = -\frac{7 \times 10^5}{\chi'}m^{-1}sec^{-1}$. Our final set of parameter values is then $C = 0.4sec^{-1}$, $\tau_R = 2.5sec$, $D = 8 \times 10^{-6}\chi' m-sec^{-1}$, $A = 40sec^{-1}$, $\tau_{\Psi} = 2.5 \times 10^{-2}sec$, $B = -\frac{7 \times 10^5}{\chi'}m^{-1}sec^{-1}$. In dimensionless units, taking $\tau_{\Psi} = 2.5 \times 10^{-2}sec$ and measuring length in units of R_0 , yields: $A = 1.0$, $C = 0.01$, $D = 0.04\chi'$ and $B = -0.09/\chi'$. If we assume $\frac{d\chi}{d\Psi}|_{\Psi=\Psi_0} \simeq \frac{\chi}{\Psi_0}$, $\chi \approx 0.5$ and $\Psi_0 = 1$, this yields $\chi' = 0.5$.

3.2.6 Numerical simulations

Our numerical simulations implement Langevin dynamics in solving the stochastic Eqns. 3.1. We use both a simple Euler discretization as well as a fourth order Runge-Kutta method, checking that both gave essentially similar results.

3.3 Results

3.3.1 Auxetic and normal mechanical behaviour in a model description of nuclear indentation

The AFM indentation experiment corresponds to taking $f = f_{\parallel} \neq 0$, setting $f_{\perp} = 0$. The set of model equations, Eqns. 3.1 have a number of parameters, which we fix using experimental and theoretical input. The choice of parameters and the range of values they can take are discussed in Methods. The solutions of these equations are provided in Appendix A.1.

Figure 3.2 shows plots of $\delta\Psi$, δR_{\parallel} and δR_{\perp} (Figure 3.2, panels (e) - (h)) for small f , as obtained from our model equations. The quantities $\delta\Psi$, δR_{\parallel} and δR_{\perp} vary linearly with f , a consequence of the fact that we assume that $V(\delta\Psi)$ increases quadratically about its stable value. This is across the parameter values shown in Figure 3.2, panels (a) - (d), for the state points (B,C) marked on the figures with the filled black circle. These plots are for a choice of parameters corresponding to non-auxetic *i.e.* regular behaviour. For the normal *i.e.*, non-auxetic state, the slope of δR_{\parallel} and δR_{\perp} *vs.* f should have opposite signs.

Our model predicts that the slope of $\delta\Psi$ *vs.* f is negative *i.e.* the compaction decreases with the applied force in the non-auxetic state; see Figure 3.2, panels (e) and (h).

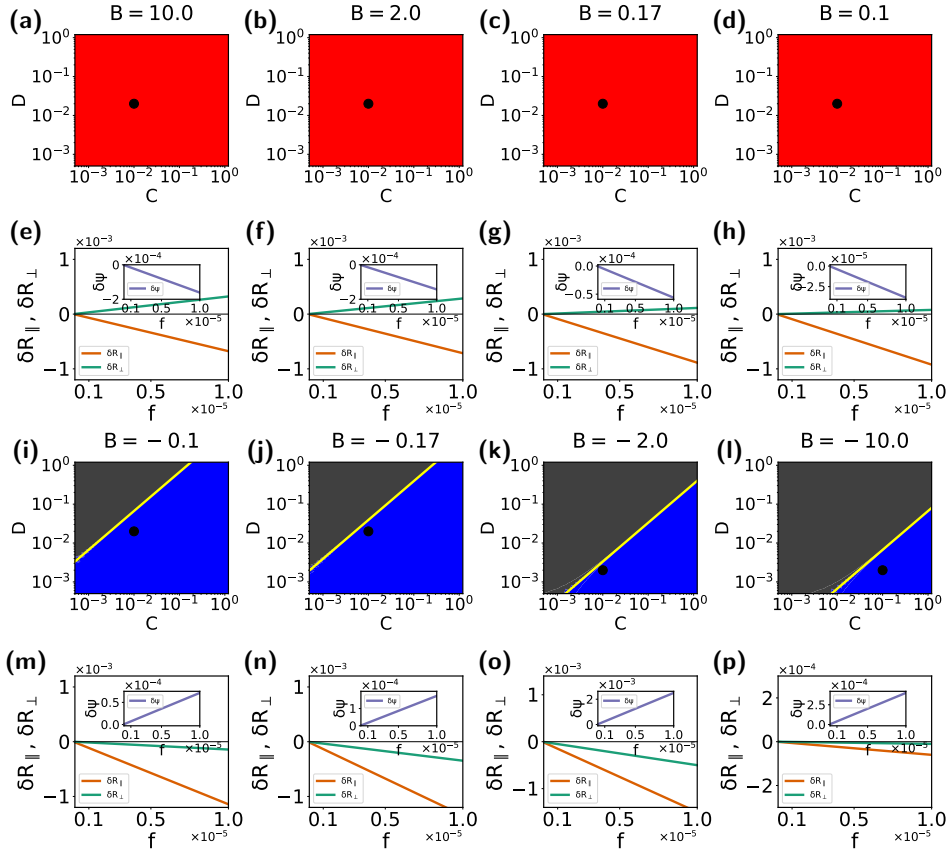


Figure 3.2: Parameter choices for C and D and : **(a)** $B = 10.0$, **(b)** $B = 2.0$ **(c)** $B = 0.17$ **(d)** $B = 0.1$, all in the regime of non-auxetic (regular) behavior . The behaviour of the dynamical variable with the increase in force for the parameter values **(e)** $C = 0.01, D = 0.02, B = 10.0$. **(f)** $C = 0.01, D = 0.02, B = 2.0$. **(g)** $C = 0.01, D = 0.02, B = 0.17$. **(h)** $C = 0.01, D = 0.02, B = 0.1$. Parameter choices for C and D , in the auxetic regime with **(i)** $B = -0.1$, **(j)** $B = -0.17$ **(k)** $B = -2.0$ **(l)** $B = -10.0$. The line separating blue and gray regions marks the stable-unstable boundary. The behaviour of the dynamical variable with the increase in force for the parameter values **(m)** $C = 0.01, D = 0.02, B = -0.1$. **(n)** $C = 0.01, D = 0.02, B = -0.17$. **(o)** $C = 0.01, D = 0.02, B = -2.0$. **(p)** $C = 0.1, D = 0.02, B = -10.0$. (Red and blue colours in the colour plots show the regions where a stable solution is obtained (red = normal, blue = auxetic) while the grey colour shows where solutions become unstable).

In Figure 3.2, panels (m) - (p), we also show results for the auxetic case, where the slope of δR_{\parallel} and δR_{\perp} vs f have the same sign. Note that δR_{\parallel} and δR_{\perp} now both decrease with f . This indicates auxetic behaviour. This behaviour is seen across the parameter values shown in Figure 3.2, panels (i) - (l), for the state points marked on the figures with the filled black circle. These parameter values are chosen in the

regime where the fixed point is stable, shown in blue. (The grey region shows the regime in which the equations have unstable solutions.) In the auxetic case, the slope of $\delta\Psi$ *vs.* f is positive.

Thus, the solutions of our model equations yield both auxetic and non-auxetic behaviour, controlled by the sign of B in Eqs. 3.1. The results are consistent with the schematics of Figure 3.1 (f) and (g), which show how chromatin compaction varies upon the application of an external force. The additional information they provide relates to the behaviour of the compaction variable. As shown in Methods, the parameter values we derive are consistent with experimental measures of auxeticity in transitional stem cell nuclei.

3.3.2 Describing nuclear shape changes in micro-channel flow

Nuclear indentation through the AFM method described in Ref. [Pagliara et al., 2014] provides a direct way of accessing the auxetic mechanical behaviour of the nucleus. Here, a fixed force is applied along the longitudinal (\parallel) direction and a transverse (\perp) deformation measured. An alternative method involves an optofluidic assay, in which cells are passed through narrow micro-channels of controlled width. These cells are then imaged through fluorescence microscopy of Syto13 labeled cells. When the width of the channel is comparable to the cell size, this constrains cell dimensions. A further complication is the role of stretching stresses caused by cytoskeletal strain acting when cells are confined to the micro-channel. Given our model assumptions, we may model the confined case by accounting both for f_{\parallel} and f_{\perp} in the governing equations, Eqs. 3.1. Whereas f_{\parallel} is primarily controlled by the size of the constriction through which these cells pass, f_{\perp} derives from the anisotropic remodelling of the actin cytoskeleton.

The geometry of the micro-channel experiments is shown in Figure 3.3(a), where

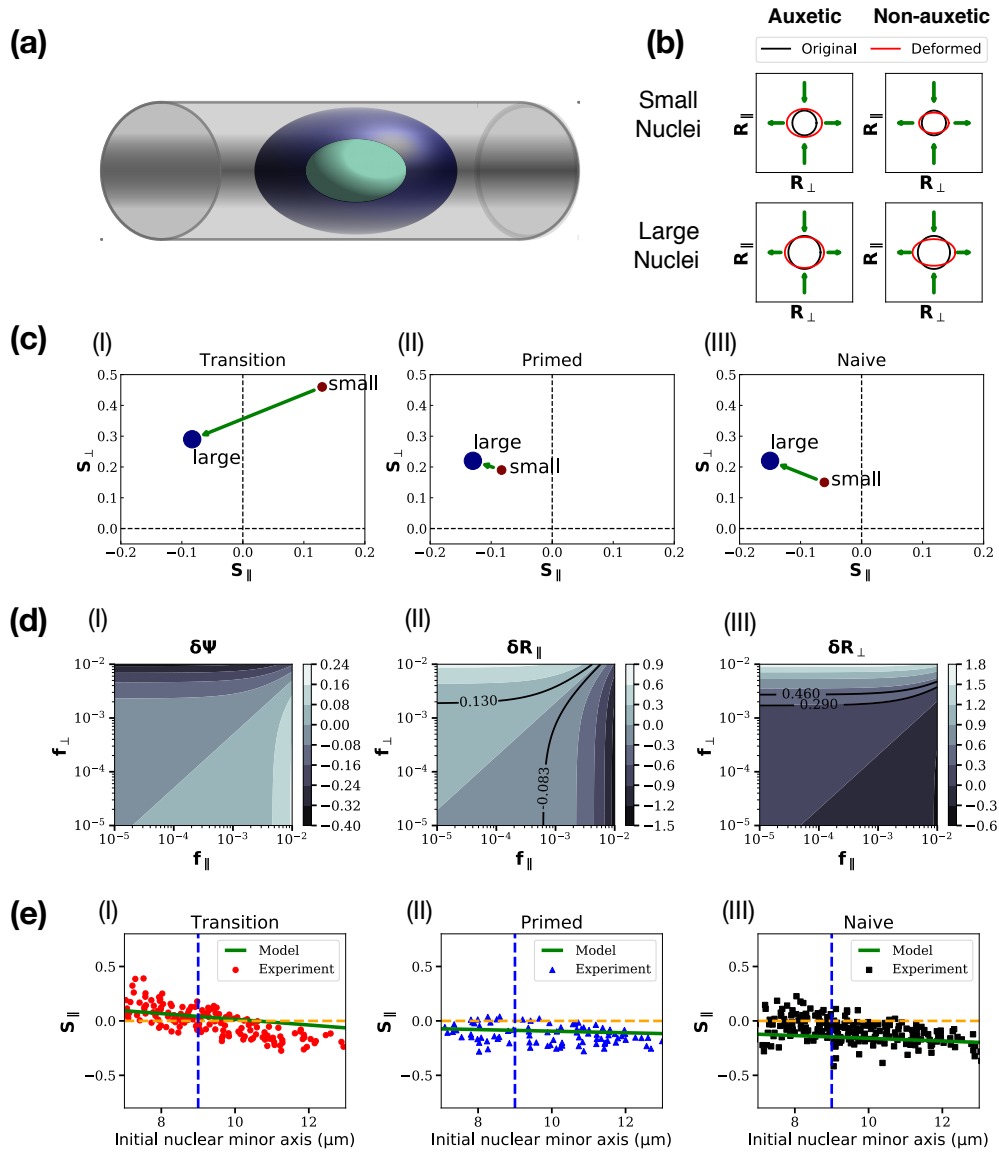


Figure 3.3: **(a)**: Schematic of a cell confined to a microchannel with width comparable to cell dimensions, **(b)** schematic of the effects of the combination of longitudinal and transverse forces applied to cells of different sizes. These follow from our calculations and are consistent with the results of Ref. [Pagliara et al., 2014], **(c)** Plots of S_{\parallel} and S_{\perp} extracted from experiments, for the transitional, primed and naive ES cell states. The arrow connects the two terminal points. **(d)** Contour plots for $\delta\Psi$, δR_{\perp} and δR_{\parallel} , against $(f_{\parallel}, f_{\perp})$, with solid lines showing loci of constant strain **(e)** Predictions for transitional, primed and naive ES cell states, of S_{\parallel} and S_{\perp} . The straight line represents experimental predictions for intermediate cell sizes. Experimental data are digitized from the scatter plot of Figure S10 of Ref. [Pagliara et al., 2014] and shown on the same figure

we show a cell confined to a channel whose width is comparable to cell dimensions. In the experiments the channel width is $12 \mu\text{m}$ while cell sizes range from $6 \mu\text{m}$

to 14 μm . Figure 3.3(b) shows a schematic of the effects of the combination of longitudinal and transverse forces applied to cells of different sizes, as obtained in our calculations; see below. For small cells in the auxetic case, if they have unconfined dimensions much smaller than the channel width, their longitudinal and transverse dimensions *increase* when they are confined to the channel. For larger cells in the same limit, both dimensions *decrease*. These are consistent with expectations from auxetic behaviour. On the other hand, irrespective of cell sizes in the non-auxetic case, the longitudinal dimension *decreases* while the transverse dimension *increases*. These are consistent with the behaviour shown in Figure 3.3(b). These schematic results recapitulate the results of Ref. [Pagliara et al., 2014].

To extend this to the mechanical response of stem cells of various sizes in a micro-channel, our modelling strategy is the following. The experiments, performed on a range of cell sizes at a fixed micro-channel width, obtain longitudinal and transverse strains for an ensemble of cells of different sizes. At the extreme limits of cell sizes, Figure S10 of Ref. [Pagliara et al., 2014] shows averaged strains in the parallel and perpendicular directions. These are proportional to R_{\parallel} and R_{\perp} in our definitions in Eq. 3.1, and using R_0 as our unit of length converts this proportionality to an equality. We label these strains as S_{\parallel} and S_{\perp} and display them in Figure 3.3(c) (I) - (III), for the transitional, primed and naive ES cell states. Starting with these results, we can invert the relationship between strains and forces, finding the effective f_{\parallel} and f_{\perp} that produce these strains.

We can now explore the space of values of $(f_{\parallel}, f_{\perp})$, constructing contour plots of $\delta\Psi$, δR_{\perp} and δR_{\parallel} , as shown in Figure 3.3 (d) (I) - (III). The parameters chosen are for the smallest and the largest cells, using the data shown in Figure 3.3(c) (I). The solid lines in Figure 3.3 (d) (II) - (III) represent a choice of a few lines of constant strain in each case, as a function of f_{\parallel} and f_{\perp} . These lines then *predict* the forces $(f_{\parallel}, f_{\perp})$ required to create a fixed strain across cells of different sizes.

The extremal points of Figure 3.3(b) (I) - (III) are now associated to points on the $(f_{\parallel}, f_{\perp})$ surface. We can then model the data for cells of sizes intermediate from these by supposing that f_{\parallel} and f_{\perp} vary independently and linearly between their terminal values. We ask if these results can fit data for intermediate cell sizes, shown in the scatterplot illustrated in Figure 3.3 of Ref. [Pagliara et al., 2014]. These results are shown in Figure 3.3(e) (I) - (III), for transitional, primed and naive ES cell states. The experimental data are shown as points while the theoretical prediction that follows from our analysis is shown as the green line. In all three cases, there is an approximate linear relationship between S_{\parallel} and S_{\perp} that our calculation captures. The magnitude of the strains at intermediate values of cell size is correctly rendered. Our model thus, despite its simplicity, captures all essential features of the data of Ref. [Pagliara et al., 2014]. As we have pointed out, the model can then be used to provide specific predictions for mechanical response in cells of different sizes. Also, even though the chromatin compaction variable $\delta\Psi$ was not measured in those experiments, our model provides specific predictions for how this quantity varies across different cell sizes in comparison to the width of the microchannel. This prediction is experimentally testable and we discuss possible ways of doing so in the concluding section.

3.3.3 Autocorrelations and cross-correlations of chromatin compaction and nuclear dimensions in the auxetic regime

The previous sections explored the use of an external force, either applied directly using an AFM tip or indirectly by confining cells to a narrow microchannel, in understanding auxetic and non-auxetic behaviour. However, our general model formulation suggests how less invasive ways of probing the coupled mechanical response of chromatin compaction and nuclear dimensions might provide useful information. Let us assume that we can measure both chromatin compaction as well as the di-

mensions of the nucleus simultaneously as a function of time - possible ways of doing this are discussed later. Assuming an initially spherical nucleus, R_{\parallel} and R_{\perp} coincide, since now there is no externally imposed direction that leads to an anisotropic mechanical response. The only relevant mechanical variable is then $R(t)$, the radius of the spherical nucleus as a function of time. Our equations are now simpler, since they involve only the two variables, Ψ and R . The solution to the full set of equations is provided in Appendix A.1.

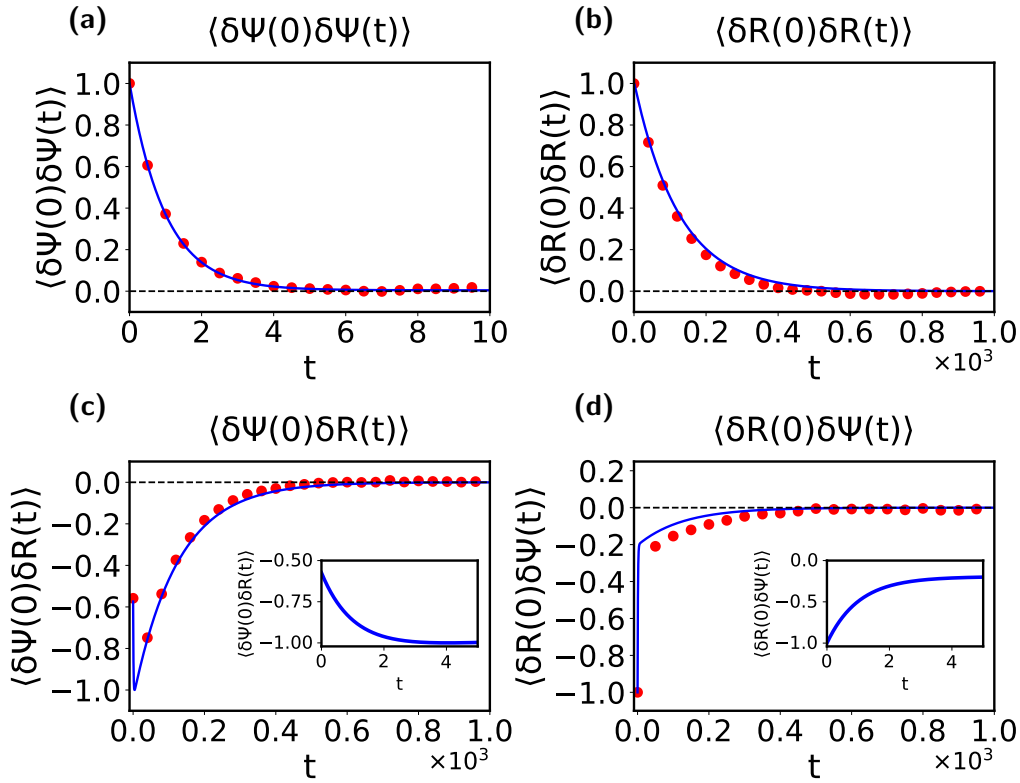


Figure 3.4: Computations of autocorrelations and cross-correlations in the simplified 2-component model, in the auxetic regime, with $C = 0.01$, $D = 0.02$ and $B = -0.17$. We illustrate the calculation of the following correlation functions: **(a)** The autocorrelation of the $\delta\Psi$ variable $\langle \delta\Psi(0)\delta\Psi(t) \rangle$, **(b)** The autocorrelation of the δR variable, $\langle \delta R(0)\delta R(t) \rangle$, **(c)** The cross-correlation between $\delta\Psi$ and δR , $\langle \delta\Psi(0)\delta R(t) \rangle$, **(d)** The cross-correlation of δR and $\delta\Psi$, $\langle \delta R(0)\delta\Psi(t) \rangle$. The insets show the behaviour close to the origin in two special cases where there is a competition between the two time-scales for relaxation. Points represent the numerical solution of the Langevin equations while lines represent the analytic formulae.

Given measurements of $\Psi(t)$ and $R(t) = R_0 + \delta R(t)$, we can ask whether signatures

of auxetic and non-auxetic behaviour might be visible in such measurements. Since such measurements provide data in time, we can compute autocorrelations of these variables as well as their cross-correlations. The solutions to these equations can be computed explicitly and are provided in Appendix A.2. Figure 3.4 shows our computation (lines: exact calculations; points: numerical solutions of the Langevin equation) of autocorrelations and cross-correlations in the model, with parameters chosen within the auxetic regime.

The autocorrelations $\langle \delta\Psi(0)\delta\Psi(t) \rangle$ and $\langle \delta R(0)\delta R(t) \rangle$ are shown in Figure 3.4(a) - (b) whereas the cross-correlations $\langle \delta\Psi(0)\delta R(t) \rangle$ and $\langle \delta R(0)\delta\Psi(t) \rangle$ are shown in Figure 3.4(c) - (d) respectively. The insets expand the behaviour of the cross-correlation functions close to the origin, where two time-scales for relaxation compete. The time-scale for the relaxation of autocorrelations in the Ψ variable is substantially smaller than for the R variable. The cross correlations $\langle \delta\Psi(0)\delta R(t) \rangle$ and $\langle \delta R(0)\delta\Psi(t) \rangle$ both relax to zero in an interesting two-step way, with a sharp initial step reflecting the relaxation of the fast variable Ψ followed by a slower relaxation, primarily driven by the R variable.

We can further investigate model predictions for the case in which a weak force is applied and allowed to vary in time in a sinusoidal fashion (see Appendix A.4). For our linear system of equations, this then implies that quantities such as Ψ , R_{\parallel} and R_{\perp} should also oscillate at the same frequency, but with a phase lag between them. This phase lag predicts the relative importance of what is termed reactive and dissipative response, with the first largely located in the elastic properties of the nuclear envelope and the second associated to dissipation connected to the flow of fluid across the nuclear envelope as well as of the friction encountered by chromatin as its fluctuations relax. These can be predicted from the theoretical formulation, and indeed are the focus of standard experiments in the physics literature that studies soft materials, but whether their experimental analogue can be probed in

biophysical measurements on stem cells is an open question.

Extracting behaviour as shown in Figure 3.4 would constitute a powerful test of model predictions.

3.3.4 Correlations across the auxetic-nonauxetic boundary as probes of the transition

Our model describes chromatin compaction states using a single variable Ψ , with larger values of Ψ representing overall more compact states of chromatin packing. We suggest that Ψ fluctuates in time about an approximately constant value, but that these fluctuations are constrained by a chromatin compaction potential defined as $V(\delta\Psi)$, that controls how large they can be. These fluctuations are also constrained by their coupling to nuclear dimensions through the variables δR_{\parallel} and δR_{\perp} . They are influenced, as well, by the inherent noisiness of nucleosome on-off dynamics in a hyperdynamic state. All these effects are included in our model.

This choice of an “chromatin compaction potential” identifies the relevant *biophysical* distinction between more open, gene-rich euchromatin and more tightly bound, gene-poor heterochromatin as broadly being one of local compaction. We project the multi-dimensional landscape of potential chromatin states that Waddington envisaged, which should be more generally describable through a spatially varying and sequence-dependant compaction field, onto a single scalar compaction variable. Our equations then provide a way of understanding how such a compaction variable couples to mechanical variables describing nuclear shape and size.

Our results suggest a simple method for determining the location of the auxetic-to-non-auxetic transition. We will work in the limit described in the previous section, where we infer the transition by monitoring the system non-invasively, measuring only the variables Ψ and R as functions of time in steady state. From these mea-

surements, we can calculate their autocorrelations and cross-correlations.

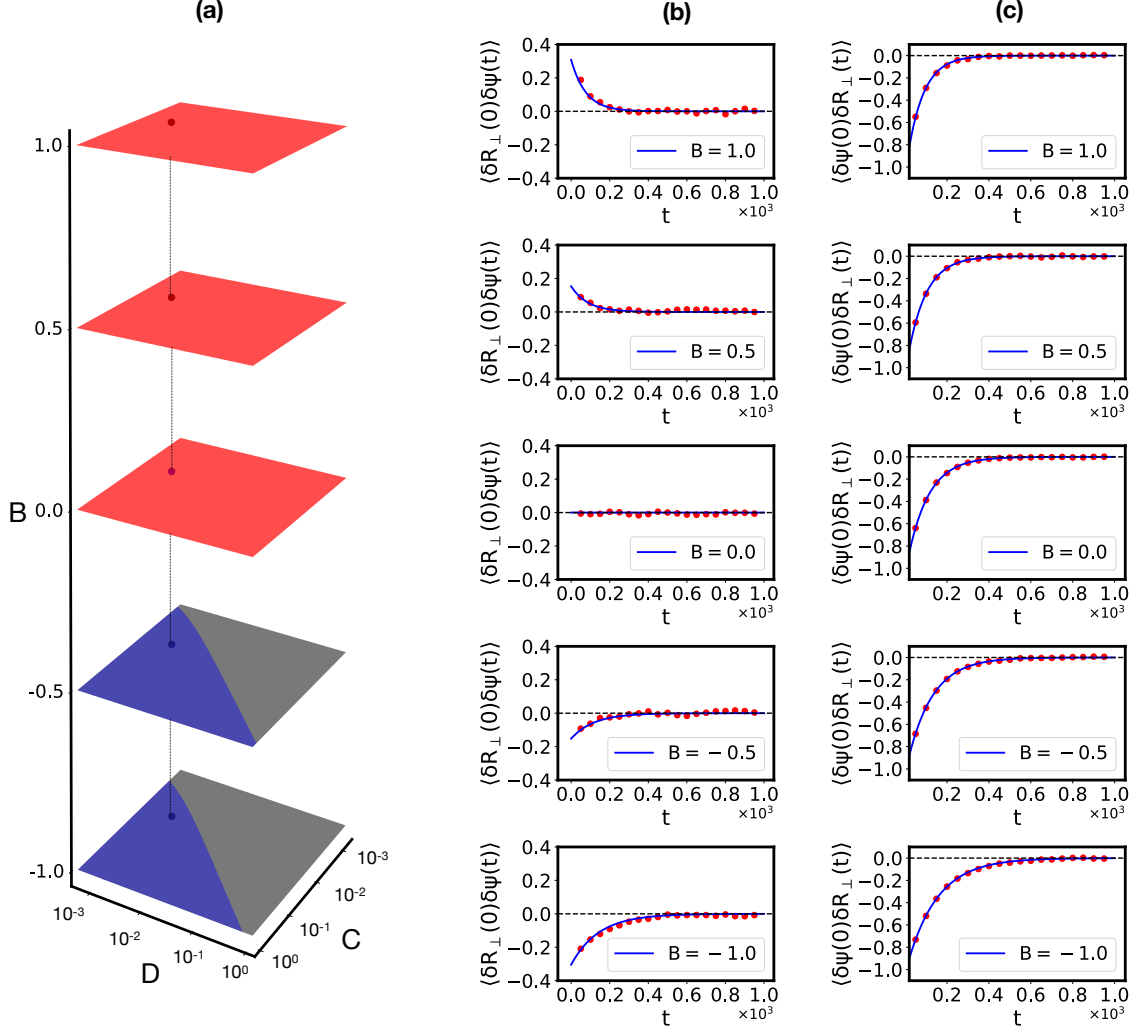


Figure 3.5: The left column (a) shows our choice of parameters in (B,C,D) space, with B, shown on the vertical axis, varied so as to cross the auxetic to non-auxetic boundary. The two columns on the right, columns (b) and (c) illustrate the correlation function $\langle \delta R(0) \delta \Psi(t) \rangle$ and $\langle \delta \Psi(0) \delta R(t) \rangle$. Across the auxetic to non-auxetic boundary, where the sign of B changes, the Ψ variable decouples, at lowest order, from the δR variable, leading to a flat behaviour of the correlation $\langle \delta R(0) \delta \Psi(t) \rangle$. In contrast, while Ψ is not influenced by δR , fluctuations in Ψ do couple to δR , leading to a non-trivial relaxation of the correlation function $\langle \delta \Psi(0) \delta R(t) \rangle$. This change of sign of $d\langle \delta R(0) \delta \Psi(t) \rangle / dt$ indicates that the auxetic to non-auxetic boundary has been crossed.

In Figure 3.5, we show plots of the correlation functions $\langle \delta R(0) \delta \Psi(t) \rangle$ and $\langle \delta \Psi(0) \delta R(t) \rangle$. These illustrate that $\langle \delta R(0) \delta \Psi(t) \rangle$ is a good indicator of the transition from auxetic to non-auxetic behaviour, with $\langle \delta R(0) \delta \Psi(t) \rangle$ changing the sign of its slope upon approaching its asymptotic value across the auxetic to non-auxetic boundary. On

the boundary, there is no correlation at all, to this order, between fluctuations in the nuclear dimension and fluctuations in chromatin compaction. Since the change from auxetic to non-auxetic behaviour is marked by the parameter B changing sign, it must cross zero at least at one point. (Since the experimental sequence encountered as ES cells differentiate is: non-auxetic \rightarrow auxetic \rightarrow non-auxetic, this suggests that B should change sign at least twice. This is a specific prediction that can be addressed in experiments, as we discuss below.)

Now note that at this special point, fluctuations in Ψ decouple from fluctuations in the nuclear size variable to linear order; fluctuations in Ψ influence fluctuations in δR but not *vice versa*. As we show below, this provides a practical way of accessing $V(\delta\Psi)$.

3.3.5 Physical argument for the transition between auxetic and non-auxetic behaviour

The values of Ψ_0 and R_0 could reasonably be expected to vary across the transition between embryonic stem cell, transitional state stem cell and the differentiation primed stem cell. The single central biophysical input we have from the experiments is that chromatin is least dense in the transitional state, where auxeticity is observed. This is in contrast to the states it borders, which behave like normal, non-auxetic materials. This is crucial, since it relates to how Ψ_0 must vary across these states. Physically, we can imagine that as we transition across the sequences N-ESC \rightarrow T-ESC \rightarrow P-cells, the value of Ψ_0 decreases till it attains its least value and then increases again. This would be consistent with experiments. We illustrate this in the figure below.

Consider the situation as shown. Starting from high values of compaction, reducing Ψ_0 exposes small sections of DNA while locally stretching it as well. This is a

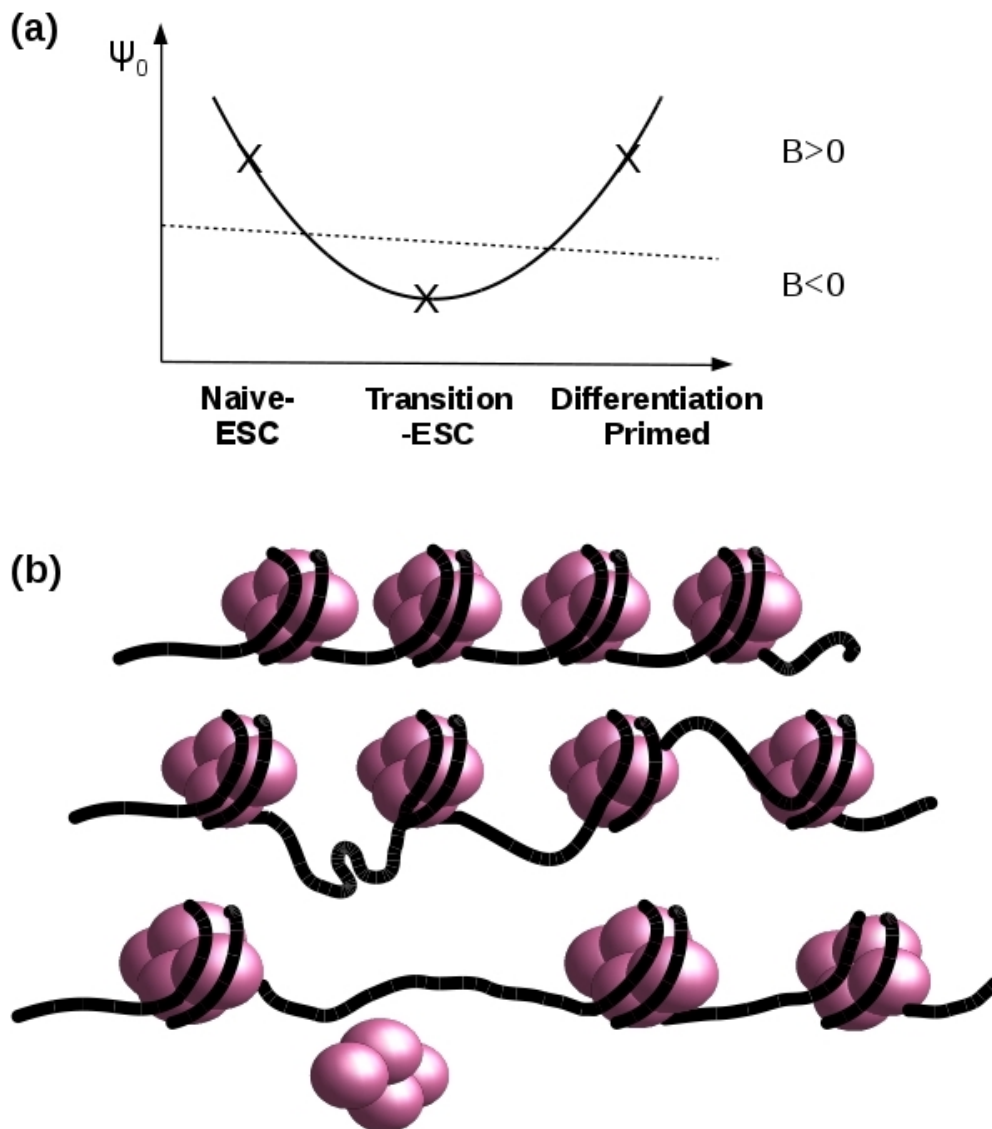


Figure 3.6: (a) Pictorial representation of values of Ψ_0 for N-ESC, T-ESC and P-cells and (b) pictorial representation of changes in chromatin compaction.

regime where we might reasonably expect that fluctuations that remove histones stretch DNA marginally further, exposing binding sites. This is the regime in which $B > 0$. Now imagine that Ψ_0 is decreased still further. Beyond a point, the physics of nucleosome ejection in stretched DNA would be expected to dominate. In this regime, we expect $B < 0$, since now extending DNA makes it less favourable for histones to bind, changing the sign of $d\epsilon/dR$. As shown in the figure, the non-monotonic structure of Ψ_0 variation across N-ESC \rightarrow T-ESC \rightarrow P-cells, implies that (a) there should be a non-trivial regime over which $B < 0$, that (b) this regime

should be bounded by two points at which $B = 0$ and that for larger values of compaction, on either side, we should have $B > 0$. These are precisely the input to our calculation and the physical intuition we provide.

3.3.6 Inferring $V(\delta\Psi)$ from experimental data

We can describe the transition between ESC, T-ESC and differentiation-primed states in terms of a trajectory in the space of the variables C, D and B . As is standard, we can assume that the parameters controlling these variables must vary smoothly, since they reflect continuous shifts in the transcriptome; indeed the assumption of smooth variation is central to landscape ideas. As the stem cell transits between these states, it encounters auxetic ($B < 0$) [Figure 3.7 (g) - (i)] and non-auxetic ($B > 0$) [Figure 3.7 (d) - (f)] states, with an intervening $B = 0$ state, [Figure 3.7 (a) - (c)].

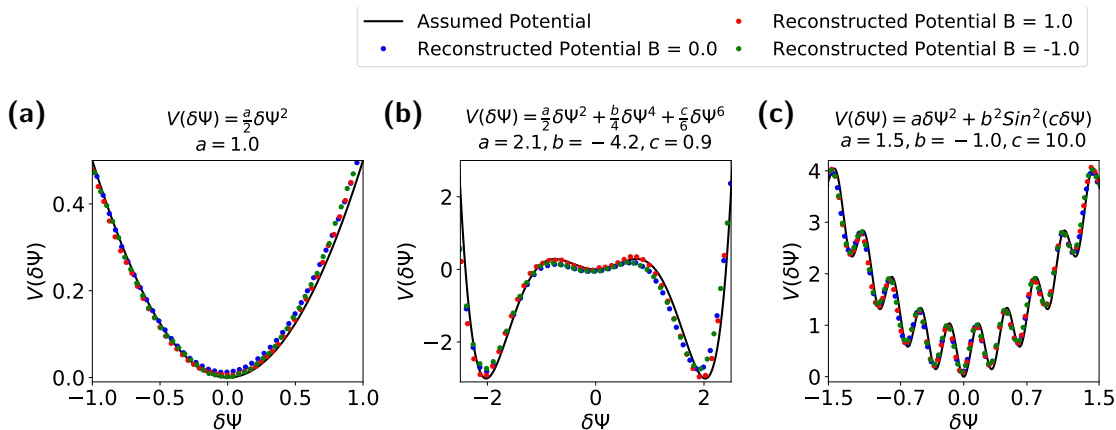


Figure 3.7: Reconstruction of the potential landscape $V(\delta\Psi)$ in the simplified 2-component model: **(a)** Assuming a quadratic potential, **(b)** Assuming a sixth-order potential, and **(c)** Assuming a quadratic potential with a superimposed sinusoid: $V(\delta\Psi) = a\delta\Psi^2 + b^2 \text{Sin}^2(c\delta\Psi)$, for $B = 0.0$ (blue), $B = 1.0$ (red) and $B = -1.0$ (green).

For each of these chosen values of B , we illustrate the choice of a specific chromatin compaction potential that we can model as a smooth function, shown via the solid lines in each sub-plot. We choose these functions to be (1) a simple quadratic

potential, (2) a quartic potential with a shallow minimum at the origin and two symmetrically placed deeper minima on either side, as well as (3), the more complex case of a quadratic potential with a superposed sinusoidal modulation that provides more intricate structure. We do not yet know what form such a potential takes in the experiments, but intend to illustrate a method by which information from the measurement of fluctuations could help in its extraction.

For $B = 0$, as shown in Figure 3.7 (a) - (c) (blue filled circles), given that $\delta\Psi(t)$ reflects its relaxation in the chromatin compaction potential, we form a histogram of $\delta\Psi$ values. Since the governing equation for the $\delta\Psi$ variable can be interpreted as a Langevin equation for a particle moving in the specified potential, the steady-state probability distribution of $\delta\Psi$ can be inferred from this histogram in a straightforward manner, as discussed later in this section. Figs. 3.7 (a) - (c) shows results from a numerical and analytic reconstruction of the assumed potential $V(\delta\Psi)$ using such a method. In this way, we thus proceed from the histogram of measured values to the potential that controls such fluctuations. While the data used in these figures is “synthetic”, the procedure for extracting the potential from them is robust.

Provided $|B| \neq 0$ is not too large and for parameter values comparable to the ones we use, this procedure reconstructs $V(\delta\Psi)$ reasonably well, a consequence of the fact that fluctuations in δR couple relatively weakly to fluctuations in $\delta\Psi$. Figs. 3.7 (a) - (c), shows $V(\delta\Psi)$, obtained from histograms of $\delta\Psi$ values for $B = -1$ (red filled circles) and $B = 1$ (green filled circles). These suggest that one need not precisely locate the region where B vanishes for this approach to be of use.

The mathematical method to extract the potential landscape from the experimental data is discussed. A simpler 2-d analog of the dynamical system 3.1 can be written

as following,

$$\delta\dot{\Psi} = -\frac{\partial V(\delta\Psi)}{\partial\delta\Psi} + B\delta R + \eta(t), \quad (3.4)$$

$$\delta\dot{R} = -C\delta R - D\delta\Psi. \quad (3.5)$$

Assuming that the dynamics of δR is much slower than that of $\delta\Psi$, we can consider δR as a constant in $\delta\dot{\Psi}$ equation. This results in,

$$\delta\dot{\Psi} = -\frac{\partial}{\partial\delta\Psi}[V(\delta\Psi) - B\delta R\delta\Psi] + \eta(t). \quad (3.6)$$

The corresponding Fokker-Planck equation can be written as,

$$\frac{\partial P(\delta\Psi, t)}{\partial t} = \frac{\partial}{\partial\delta\Psi} \left[\frac{\partial V_{eff}(\delta\Psi)}{\partial\delta\Psi} P(\delta\Psi, t) \right] + \frac{1}{2} \frac{\partial^2}{\partial^2\delta\Psi} P(\delta\Psi, t), \quad (3.7)$$

where $V_{eff}(\delta\Psi) = V(\delta\Psi) - B\delta R\delta\Psi$.

For the steady state solution $\partial P/\partial t = 0$,

$$\frac{\partial}{\partial\delta\Psi} \left[\frac{\partial V_{eff}(\delta\Psi)}{\partial\delta\Psi} P(\delta\Psi, t) \right] + \frac{1}{2} \frac{\partial^2}{\partial^2\delta\Psi} P(\delta\Psi, t) = 0, \quad (3.8)$$

or,

$$\frac{\partial}{\partial\delta\Psi} \left[\frac{\partial V_{eff}(\delta\Psi)}{\partial\delta\Psi} P_s(\delta\Psi) + \frac{1}{2} \frac{\partial}{\partial\delta\Psi} P_s(\delta\Psi) \right] = 0 = \frac{\partial}{\partial\delta\Psi} j(\delta\Psi) \quad (3.9)$$

In steady state, the flux $j(\delta\Psi)$ vanishes, thus This means,

$$\left[\frac{d}{d\delta\Psi} + 2 \frac{dV_{eff}(\delta\Psi)}{d\delta\Psi} \right] P_s(\delta\Psi) = 0. \quad (3.10)$$

The above equation can be solved for the values of $\delta\Psi$ for a constant value of δR . Once we have those values, we can obtain the distribution $P(\delta\Psi)$. Taking the

negative log of this result yields the effective potential V_{eff} , as

$$\begin{aligned}
P_s(\delta\Psi) &\sim \exp(-2V_{eff}(\delta\Psi)), \\
P_s(\delta\Psi) &\sim \exp(-2(V(\delta\Psi)) - B\delta R\delta\Psi), \\
V(\delta\Psi) &\sim -0.5 \ln[P_s(\delta\Psi)] + B\delta R\delta\Psi.
\end{aligned}
\tag{3.11}$$

For the parameter value $B = 0$, this expression relates the probability distribution $P(\delta\Psi)$ to the potential landscape $V(\delta\Psi)$.

3.4 Discussion

An "epigenetic landscape", whose lowest points represent gene expression patterns encoding specific differentiated states, is often pictorially represented in the following way [Huang, 2012, Furusawa and Kaneko, 2012]: Imagine projecting all possible gene expression states onto a two-dimensional (XY) plane. This projection is constrained by the requirement that two nearby state points represent closely related expression patterns. (Naively, the rewiring of gene-regulatory networks required to convert expression programs from one cell type to another should be smaller the more similar these cell types are [Huang, 2012].) The height of a surface (the landscape) above a point on this plane can then be assigned to the relative "energy" of the state described by that point. The shape of the surface can then be used as a qualitative way of describing barriers to accessing different gene expression patterns starting from a given initial state.

The plasticity required of gene-regulatory networks in the stem cell states implies, in this pictorial analogy, that the shape of the landscape should determine which states will become unstable - and to which other states - as biochemical and mechanical parameters are changed. Biochemical parameters here could refer to levels of protein

factors that modulate stemness while mechanical parameters could represent the stiffness and anisotropy of the substrate on which these cells are cultured [Li et al., 2012]. If one imagines, as Waddington did, a ball rolling on this landscape as representing the stem cell state choosing between terminally differentiated states, the motion of the ball should be biased by the underlying shape of the landscape, including its peaks, ridges and valleys. The resulting energy surface can be depicted as a geographical landscape, along the lines of Waddington's original picture.

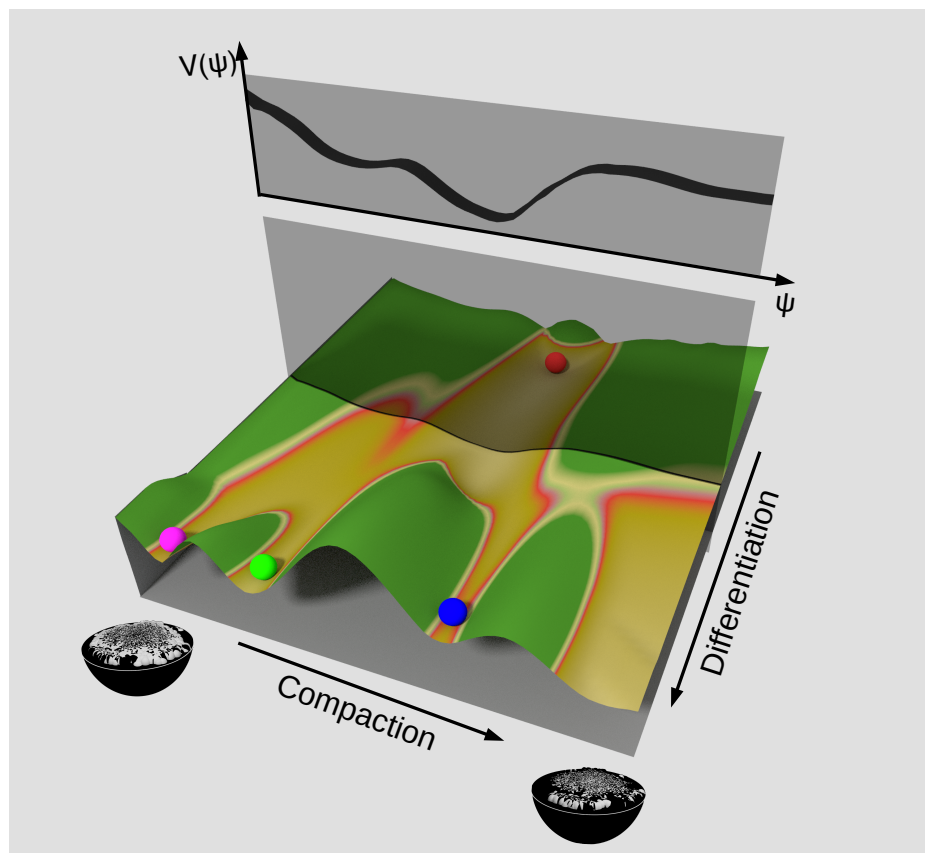


Figure 3.8: Schematic of an epigenetic landscape in the compaction variable. A pictorial representation of the epigenetic landscape, projected onto a single variable describing overall compaction. Points towards the back of the figure represented the ES cell state while points in the valleys towards the foreground represent differentiated states. As one moves from back to front, the figure describes how the effective potential governing overall compaction can be described via a cut through the landscape as shown.

Such a qualitative picture also suggests that this landscape might also be thought of as *dynamic*, tilting and deforming to favour one set of states over others. This

would then describe how an initial state might be guided to a specific cell fate as the cell integrates external environmental signals when driven to differentiate.

The description of the previous paragraph proceeded along conventional lines. Our view here emphasizes biophysical aspects of this argument. Instead of projecting states depending on their proximity in gene expression space, we imagine them to be projected according to their level of chromatin compaction; arguments concerning the proximity of closely related cell types in such a “chromatin compaction” space should parallel those in the case of the “gene expression” space. To motivate this, we note that the relative ratio of heterochromatin to euchromatin varies across differentiated cell types [Rivera and Ren, 2013]. It has been suggested that chromatin density might itself act to regulate gene expression in a stem cell population [Golkaram et al., 2017]. While the embryonic stem cell state has a chromatin organization that is best described as a highly correlated fluid, the differentiated state fluctuates far less, with condensed heterochromatin foci forming during the differentiation of pluripotent embryonic stem cells [Mao et al., 2015]. The formation of heterochromatin domains has recently been argued to be mediated by phase separation [Larson et al., 2017, Strom et al., 2017]. Together with the accumulation of silencing histone marks, this results in differential expression [Meshorer and Misteli, 2006]. Classifying the epigenetic states underlying these cell types through their levels of local chromatin compaction should provide one approximate way of connecting the theoretical ideas presented here to experimental data.

This idea is illustrated in Figure 3.8, which shows a schematic of such a landscape. The coloured balls towards the front of the figure represents stable, differentiated states. The ball at the back represents the ES cell state. As the cell differentiates, one imagines that the landscape is tilted forward so as to allow the ball to fall towards these stable states. All possible accessible intermediate states can be represented, again pictorially, in terms of a plan that intersects this landscape. The curve that

defines where these two curves intersect provides a one-dimensional surface, to be identified with the $V(\delta\Psi)$ of our discussion.

We stress that *all* projections from a high-dimensional space to a low-dimensional one, involve a loss of information. The question is whether the reduced information that results from projecting the complexity of epigenetic control into the reduced space of overall compaction, suffices for a biophysical description. Expanding the potential $V(\delta\Psi)$ about a local minimum led to the results described in this chapter. However, we should ideally think of this potential as itself evolving over some time scale and the choice of the initial point as reflecting a cell-specific initial condition, such as cellular levels of Lamin A [[Swift et al., 2013](#)].

3.5 Conclusions

In this chapter, we presented a theory of auxetic behaviour in the nuclei of stem cells in the transitional state. We began by pointing out that the unusual mechanical properties of the stem cell nucleus, as well as its fluctuations, should provide a window into the packaging and dynamic character of the chromatin states contained within it. We proposed that fluctuations in chromatin compaction should couple to fluctuations in the dimensions of the relatively soft nucleus that characterizes stem cells. We used these observations to argue that these coupled fluctuations, in chromatin packaging and nuclear shape, were most easily described in terms of a coupled, in general non-linear, dynamical system in three variables. We exploited the experimental observation that chromatin is least compact in the transitional state as compared to the pluripotent state and the differentiation primed state, to argue for a specific sign of the coupling term that connected size fluctuations to chromatin density fluctuations. We then showed how auxeticity resulted as a consequence, providing a simple and intuitive explanation for this puzzling observation. We then

went on to suggest that we could map out the normal to auxetic transition using ideas from the model. We further suggested experiments that could implement and test these ideas.

Our model could be generalized in several ways. The chromatin compaction variable is central to our discussion. Neglecting spatial variations in Ψ , as we do in this chapter, should be a valid first approximation in the relatively fluid stem cell state. However, chromatin compaction is certainly inhomogeneous in the differentiated state, while fluctuations about even the uniform state should, in principle, also be allowed for. Replacing Ψ by the field variable $\Psi(\mathbf{r}, t)$, thus allowing it to vary both in space and in time, would be the logical next step in generalizing our model. Our simple parametrization of nuclear shape and mechanics could certainly be improved upon. Finally, simulations of a suitably coarse-grained model for active confined polymers, coupled to a flexible confining nuclear envelope, are feasible. It would be interesting to see how the arguments we supply here might be tested in such simulations. In all, however, we would not expect these technical improvements to alter our basic intuition qualitatively and would argue that the simplicity of our model makes it especially attractive.

We have proposed that projecting the complex spatial-temporal distribution of chromatin compaction onto an overall compaction variable and interpreting the time-dependence of this variable in terms of motion within a simplified one-dimensional potential, should provide a particularly useful biophysical way of formalizing Waddington's intuitive picture of an "epigenetic landscape" [Gilbert, 2000]. This way of understanding landscape ideas in the differentiation of stem cells is novel. Implementing the related analysis experimentally would seem to be feasible. In particular, the fluorescence anisotropy measurements of labelled histones in the embryonic stem cells state presented in Ref. [Talwar et al., 2013], coupled to confocal microscopy measurements of the nuclear dimensions, should provide a non-invasive way of deter-

mining the coupling of chromatin compaction to mechanical variables describing the nucleus and its shape. Examining other possibilities for simultaneously characterizing chromatin compaction in addition to nuclear size and shape in a non-invasive way would be especially valuable.

Connecting microscopic, molecular-scale biochemical views of how stem cell transcriptional programs are modulated, with the averaged, larger-scale biophysical approach that we describe in this chapter, should lead to an improved understanding of the communication between stem cell nuclear mechanics and chromatin states. This improved understanding would also help to illuminate the role of the mechanical environment in biasing lineage choice.

Chapter 4

Crowding and Confinement influence polymer conformations and single particle diffusion

In this chapter, we present results from molecular dynamics simulations from two problems. One of them, presented in section [4.1](#), is of a spherically confined neutral polymer in the presence of crowding particles, studying polymer shapes and conformations as a function of the strength of the attraction to the confining wall, solvent quality and the density of crowders. The conformations of the polymer under good solvent conditions are seen to be largely independent of crowder particle density, even when the polymer is strongly confined. In contrast, under poor solvent conditions, when the polymer assumes a collapsed conformation when unconfined, it can exhibit transitions to two different adsorbed phases, when either the interaction with the wall or the density of crowder particles is changed.

In the second problem, presented in section [4.2](#), we present results for a different geometry, studying results from molecular dynamics simulations of a particle in an infinitely long cylinder grafted with neutral polymers. This chapter is partly based

on the work presented in Ref. [Tripathi et al., 2019].

4.1 Confined Crowded Polymers near Attractive Surfaces

For an unconfined neutral polymer, the nature of the solvent determines whether the polymer adopts, on average, an extended or a collapsed conformation. If confined, the polymer experiences a loss of conformational entropy. This reduces allowed configurations to a subset that depends on the shape and other properties of the confining volume [Ganai et al., 2014, Jun and Mulder, 2006, Jun and Wright, 2010, Kang et al., 2015b, Tark-Dame et al., 2011, Jeon et al., 2016, Fošnarič et al., 2013, Ruggiero et al., 2018]. A number of polymers in biological contexts encounter varying degrees of confinement. The approximately $2m$ of DNA in the nucleus of eukaryotic cells must be restricted to a nucleus that is $\sim 10\mu m$ in radius, while the packaging of viral DNA into sub-micron-sized protein capsids is often dense enough to induce local crystallinity [Boyle et al., 2001, Misteli, 2007, Lieberman-Aiden et al., 2009]. Cargo transported along axons by molecular motors typically consists of specific protein molecules encapsulated in vesicles of diameter $30 - 80nm$, comparable in dimension to the larger peptide neurotransmitters that such vesicles must accommodate [Purves et al., 2001].

Biological polymers *in vivo*, in addition to being confined in their natural contexts, also inhabit highly crowded environments. The presence of crowders can affect the compaction and higher-order organization of single biopolymer, as well as promote aggregation of such polymers in solutions [Ha and Jung, 2015, Zimmerman and Minton, 1993, Phillips et al., 2012, Zhou, 2013, Feig et al., 2017, Lim and Denton, 2014, Ellis, 2001]. At high crowder concentration, neutral polymers have been shown to undergo a continuous extended-to-collapsed transition [Shendruk et al.,

2015, van den Berg et al., 1999]. Incorporating attractive interactions between crowder particles and macromolecular polymers leads to the formation of complex aggregates which can be observed directly [Zhou et al., 2008]. Although repulsive interactions do not promote the formation of complexes, they can affect reaction rates and conformations via the Asakura Oosawa depletion interaction [Asakura and Oosawa, 1954]. Experiments show that small molecules such as polyethylene glycol (PEG) can condense DNA [Vasilevskaya et al., 1995]. Although DNA is confined and crowded within the nucleus, it is not structureless and the interplay between polymer shape, confinement and crowding can potentially accentuate certain aspects of such a structure while attenuating others. Within the cell, the presence of a heterogeneous mixture of proteins, organelles, water and ions can influence the loss of conformational entropy of the biopolymers present in ways that are particularly hard to predict [Zimmerman and Minton, 1993, Minton, 2005, Uversky et al., 2002, Cheung et al., 2005, Bokvist and Gröbner, 2007]. As regards the effects of confining polymers by surfaces, understanding polymer adsorption onto surfaces as solvent conditions are varied is relevant both to the efficiency of biosensors [Yang et al., 2015] as well as to the formulation of protein resistant coatings [Ionov et al., 2009, Haraguchi et al., 2014]. The ability to accurately describe the phase behavior of polymers in confined, crowded regimes is thus central to an improved understanding of a number of biological processes [Strulson et al., 2014, Onuchic and Wolynes, 2004, Thirumalai and Hyeon, 2005, Iborra, 2007].

Using atomistic simulations to study the structural and dynamical properties of realistic bio-polymers is computationally expensive, even without accounting for crowders. Thus, many studies use a coarse-grained, neutral polymer description of such biopolymers, even though biologically relevant polymers such as DNA are typically weakly charged in solution. (The screening of the charges through counterions, salt and the presence of other charged species around the biological polymer of relevance should render the electrostatic interactions effectively short-ranged [Nelson,

2004].) A number of coarse-grained simulation studies of neutral polymers in the presence of crowders have been performed earlier [Reddy and Yethiraj, 2006, Jeon et al., 2016, Kang et al., 2015b, Shin et al., 2015]. Several other studies have examined the interaction of both neutral and charged polymers with surfaces [Rajesh et al., 2002, Reddy and Yethiraj, 2010, Bachmann and Janke, 2005, Plascak et al., 2017, Martins et al., 2018].

The interplay between chain entropy, monomer-monomer interactions and monomer-surface interactions should determine the conformational landscape of polymers near surfaces. There appear to be four dominant "phases" that describe the behaviour of neutral polymers near attractive walls and under different solvent conditions: the desorbed-extended (DE), desorbed-collapsed (DC), adsorbed-extended (AE) and adsorbed-collapsed (AC) phases [Rajesh et al., 2002, Bachmann and Janke, 2005, Arkin and Janke, 2012a, Krawczyk et al., 2005]. Using phenomenological arguments, Rajesh *et al.* [Rajesh et al., 2002] showed that for low values of attraction between the monomers and the surface as well as between the monomers, the polymer adopts a desorbed-extended conformation (DE). Upon increasing the monomer-monomer attraction, a desorbed-collapsed (DC) phase results. If the interaction strength between monomer and surface is further increased, the polymer can assume either an adsorbed-extended (AE) or an adsorbed-collapsed (AC) conformation, depending on the monomer-monomer interaction. These authors also predicted a "surface attached globule" state (SAG), in which the number of contacts between the collapsed conformations of the polymer and the surface is much less than that in AC phase.

Monte-Carlo simulation studies of neutral and spherically confined polymers suggest that at low temperatures, where enthalpic effects dominate, the polymer adsorbs on the wall of the sphere, tending to form layer-like structures [Arkin and Janke, 2012b, Bachmann and Janke, 2005]. At higher temperatures, where entropic

effects dominate, the polymer was found to desorb, assuming an extended conformation (DE). The effect of solvent conditions on polymer conformations near the surface have also been studied using lattice models of a grafted polymer on a surface [Plascak et al., 2017]. Under good solvent conditions, a grafted polymer on a flat surface is adsorbed on the surface at low temperatures, while it assumes a desorbed conformation at higher temperatures. Under poor solvent conditions and for low temperatures, the polymer takes a globular adsorbed conformation, while for higher temperatures, the polymer desorbs from the surface. Multi-canonical Monte Carlo simulations suggest a possible phase diagram consolidating the observed behaviour [Arkin and Janke, 2012b]. In this phase diagram, for low temperatures and for a small value of monomer-surface interaction energy, the polymer assumes a desorbed collapsed conformation. With increasing surface interaction, the polymer undergoes a transition from an amorphous globular conformation to a more layered internal structure. The layering, in those simulations, covered regimes ranging between a 4-layered adsorbed structure to an adsorbed monolayer.

Although various aspects of confinement and crowding in relation to polymer conformation near attractive surfaces have been studied before, we know of no studies that examine the interplay of all three parameters on an equal footing. In addition, we note that the simulations, especially those for attractive surfaces, have largely been performed on polymers of relatively short chain length. The layered structures observed in these regimes in previous work could thus be an artefact of the small polymer size. Different structures could possibly be stabilized, or the boundaries between the states proposed earlier altered, when long chain polymers, as opposed to short ones, are adsorbed at a surface. In addition, confining polymers in three dimensions and adding crowders to the system adds further dimensions of complexity, but represent a scenario that is more relevant to biophysical situations.

To examine these questions, this part of the chapter explores how confinement, crow-

der density, solvent conditions and surface interaction combine to influence polymer conformations, using simulations of a simple model system. Our work [Tripathi et al., 2019] extends previous results through the incorporation of the effects of crowder density, specifically, in the confined case with wall interaction. We point out that solvent quality and crowder density complement each other in determining configurations, and that the resultant effects of these are most prominent in the poor solvent case. We characterize the "crumpling" of polymer conformations under the combination of high crowder density and poor solvent conditions. Although the parameter space is large, our results provide an understanding for the nature of polymer conformations in each of these different regimes, suggesting physical arguments for why they should be stabilized.

4.1.1 Methods

We study, using molecular dynamics simulations, a single, long, self-avoiding polymer chain of 400 monomers, confined to the interior of a hollow sphere. The simulated volume also contains crowdors *i.e.* particles that interact non-specifically with the monomers constituting the chain as well as with themselves. In our simulations, we vary solvent quality across the extreme limits of good and poor solvents. There are no other explicit solvent particles, aside from the crowder particles. In previous work [Kang et al., 2015a], a parameter λ was defined to compare the relative sizes of the crowder particle and the polymer ($\lambda = R_g^0/\sigma_c$, where R_g^0 is the radius of gyration of the polymer with no crowder particles present and σ_c is the size of the crowder particle). Following this definition, the sizes chosen in our present simulations correspond to the case of $\lambda \gg 1$ as the monomer and the crowder particle have the same size.

We define the crowder density as $\phi_c = N_c v_c/V$, with N_c being the number of crowdors, $v_c = 4/3\pi\sigma_c^3$ the volume of each crowder particle, σ_c the radius of the crowder,

and V the volume of the spherical confining region. We vary ϕ_c between 0.035 to 0.435 in steps of 0.05, by changing the number of crowder particles between 950 and 11750. The range of crowder densities considered in this work is similar to the range used in previous work [Kang et al., 2015a, Kang et al., 2015b, Palit et al., 2017]. We also perform simulations of a polymer in a good solvent placed in a periodic box, thus mimicking the unconfined case, so as to compare our results with results for the confined case. The crowder density range explored for such simulations is the same as for the confined case.

Pairs of all non-bonded particles (monomers and crowders) interact through the van der Waals interactions, modeled through a truncated and shifted Lennard Jones (LJ) 6-12 potential with a cutoff of r_c , where

$$V_{ij}^{LJ}(r_{ij}) = \begin{cases} 4\epsilon_{ij} \left[\left(\frac{\sigma_{ij}}{r_{ij}} \right)^{12} - \left(\frac{\sigma_{ij}}{r_{ij}} \right)^6 \right] & r < r_c \\ 0 & r \geq r_c \end{cases} \quad (4.1)$$

Here $i, j = m, c$ refers to the monomers and crowder particles respectively, and r_{ij} is the distance between two particles, (By definition, ϵ_{ij} is a symmetric matrix and the quantities ϵ_{ij} and σ_{ij} define the corresponding interaction parameters.) The size of the monomer and the crowder particles is set to be 1.0, in our reduced units. We model different solvent conditions by choosing different values for the cutoff distance r_c for the interactions among the monomers. The good and poor solvent conditions are mimicked via interactions among the monomers with different r_c (see Table 4.1). The nature of the interactions among crowder particles and between crowders and monomers is a repulsive, soft-core interaction ($r_c = 2^{1/6}$). The interaction of the monomers with the wall is also described by a Lennard-Jones potential and both repulsive and attractive wall interactions between monomers and wall are considered. The interaction of the crowder particles with the wall is set to be repulsive regardless

of solvent condition. The strength and sign of the interaction of the polymer with the wall can be varied, so that the full range between repulsive and attractive wall strengths is accessed. The parameters used in this study are given in Table 4.1.

	Good solvent			Poor solvent		
$\mathbf{i} - \mathbf{j}$	ϵ_{ij}	σ_{ij}	\mathbf{r}_c	ϵ_{ij}	σ_{ij}	\mathbf{r}_c
m-m	1.00	1.00	$(2)^{1/6}$	1.00	1.00	2.5
c-c	1.00	1.00	$(2)^{1/6}$	1.00	1.00	$(2)^{1/6}$
m-c	0.50	1.00	$(2)^{1/6}$	5.00	1.00	$(2)^{1/6}$

Table 4.1: Table of parameters for LJ potential for good and poor solvent conditions. Different values of r_c determine the solvent condition. To delineate the effect of poor solvent conditions, a higher value of ϵ_{ij} was used between monomers and crowder particles, though the potential is soft-core repulsion for good and bad solvent cases.

The polymer chain connectivity is modelled via a harmonic potential,

$$V_{ij}^{bond}(r_{ij}) = \frac{1}{2}k_{bond}(r_{ij} - r_0)^2, \quad (4.2)$$

where the bond length r_0 for the polymer is set to be 1.122. The equation of motion is integrated for 10^8 steps using a velocity-Verlet algorithm. The step size is taken to be $\delta t = 0.001\tau$, where $\tau = \sigma\sqrt{m/\epsilon}$, m , σ and ϵ are units of mass, length and energy respectively. All simulations are performed under constant volume and temperature (T) conditions ($T = 1.0$) using a Nosé–Hoover thermostat. The MD implementation is from the LAMMPS [Plimpton, 1995] software package. All visual image generation and analysis was performed using scripts developed in the VMD package [Humphrey et al., 1996]. The system’s initial configuration is constructed using the Pizza-py toolkit [Plimpton, 1995]. A harmonic wall interaction was initially used for 10^4 steps to stabilise the polymer inside the confining surface (of radius $R = 15.0$). With this starting point, several systems with the desired wall interaction potential and parameters were generated.

Different shape parameters are calculated to assess the size and shape of the polymer,

as detailed below. The radius of gyration is defined as

$$R_g^2 = \frac{1}{2N^2} \sum_{i=1}^N \sum_{j=1}^N |(\mathbf{r}_i - \mathbf{r}_j)|^2. \quad (4.3)$$

Additional shape parameters can be defined using the gyration tensor,

$$S_{mn} = \frac{1}{2N^2} \sum_{i=1}^N \sum_{j=1}^N (r_m^i - r_m^j) (r_n^i - r_n^j). \quad (4.4)$$

The gyration tensor can be diagonalised, yielding three eigenvalues $\lambda_1, \lambda_2, \lambda_3$ (where we order $\lambda_1 < \lambda_2 < \lambda_3$). The asphericity b , which describes the deviation of the average shape of the polymer from a sphere, is defined as,

$$b = \lambda_3 - \frac{1}{2}(\lambda_1 + \lambda_2). \quad (4.5)$$

The local structure of polymer conformations can be represented through contact maps. If any two monomers, say monomer i and monomer j , approach each other to within a distance of 2σ , this is counted as a contact between i and j . Contact maps are calculated over a production run ($5 \times 10^6 \tau$). An average value for the number of contacts is then computed and associated to elements of a two dimensional matrix indexed by monomer labels. For the confined, adsorbed case, we count the average fraction of monomers adsorbed on the surface. We also measure a height function that quantifies the height of the adsorbed configuration relative to the confining sphere surface. To calculate the height of the polymer stacks, we calculate the distance of each monomer from the centre of the confining sphere. We then subtract this quantity from the radius of the confinement. The largest number thus obtained, after averaging over a large number of configurations, is a measure of the height of the polymer stack, and is termed H .

To understand the effect of the curvature of the confinement on the conformation of the polymer, we performed additional simulations with a larger sphere of radius $R = 30.0$, for the same crowder densities and potential parameters. In all cases, we perform a large number of simulations starting from different initial conditions and with the same parameters to ensure good statistical averaging.

4.1.2 Results

Effect of confinement and crowders on polymer conformations in a good solvent

To understand the impact of crowder particle density and confinement on polymer conformation, we simulated the neutral polymer within a confining sphere with repulsive walls, and under good solvent conditions. A control simulation with periodic boundary conditions was also performed to compare results for confined and unconfined polymers.

We measured the radius of gyration R_g of the polymer, under both confining and non-confining conditions, varying crowder densities. Our results are shown in Figure 4.1. The radius of the confining sphere was chosen based on the typical R_g value of the polymer in the unconfined case ensuring that even at the smallest crowder particle densities, the R_g value of the polymer in the confined sphere is significantly lower than that in the unconfined case.

Earlier studies [Kang et al., 2015b, Kang et al., 2015a, Marenz et al., 2012, Hsu and Grassberger, 2005, Shendruk et al., 2014, Cacciuto and Luijten, 2006, Das and Chakraborty, 2010], both theoretical and computational, have shown that the primary effect of confinement is to reduce the conformational space available to the polymer. This can be seen in our simulations at very low crowder density. As the crowder density is increased, the conformations of confined and unconfined polymer

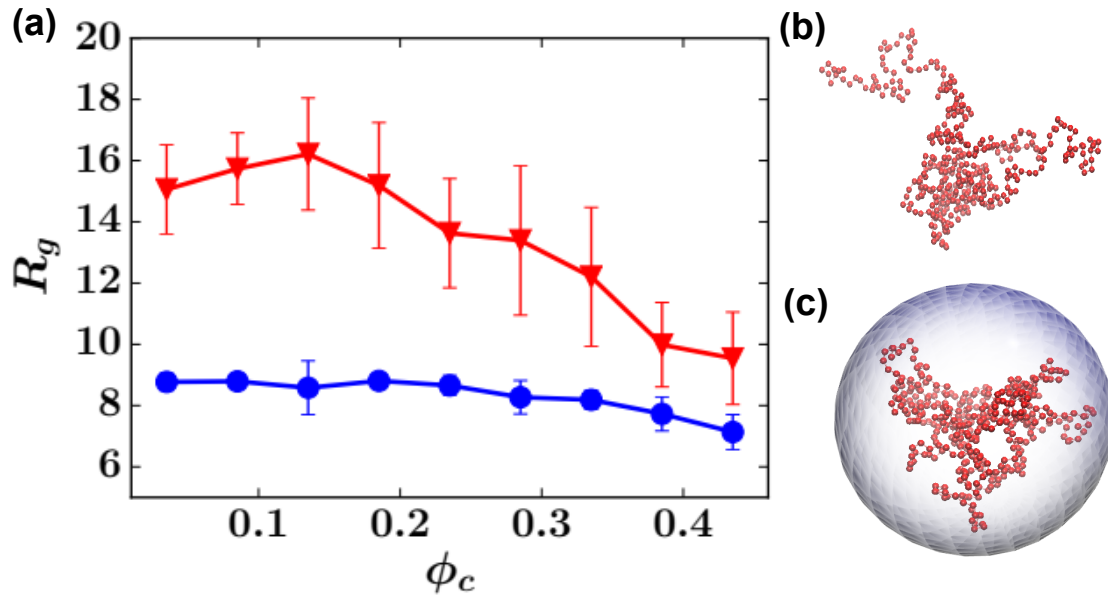


Figure 4.1: **(a)** The radius of gyration of the polymer in a good solvent condition under confinement with repulsive walls (blue) and in the absence of confinement (red) at different crowder densities. Each data point for unconfined and confined polymer is averaged over 10 and 5 simulations respectively. The corresponding error bars are also shown in the figure which represent standard deviation of the data. **(b,c)** Snapshots of the polymer at the highest crowder density are shown for periodic boundary conditions and spherical confinement.

vary differently with the crowder densities. As seen in earlier work [Kang et al., 2015a] for the unconfined case, R_g values decrease, indicating an evolution into a more compact structure, as the crowder density is increased. Figure 4.2, shows the relative change with respect to the lowest crowder density considered in this study. From both Figure 4.1 and Figure 4.2, it can be seen that for the highest crowder density simulated here, the reduction of R_g is significant, as also seen in other studies [Mao et al., 1995, Kim et al., 2015, Shendruk et al., 2014, Jeon et al., 2016]. This is a consequence of depletion forces due to the crowders. However, note that the decrease is not as dramatic as that seen in Ref. [Kang et al., 2015a], for similar values of λ . This is likely because the polymers used in the present study are significantly longer than those used in previous work.

For the confined case, the R_g values of the polymer are relatively insensitive to the crowder densities when compared to the unconfined polymer, with only a slight re-

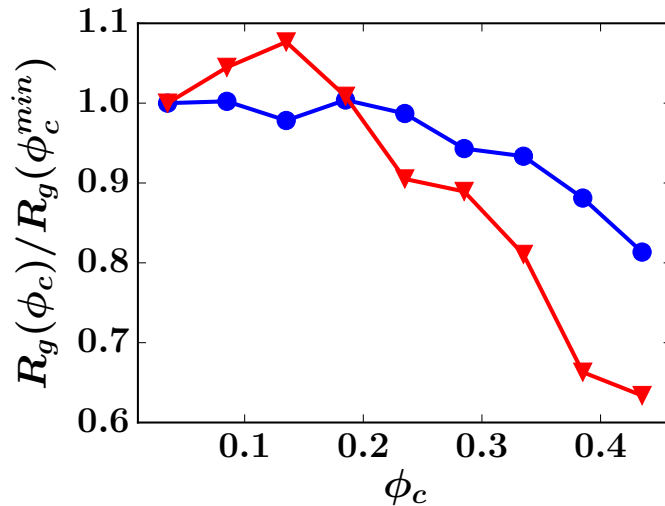


Figure 4.2: Relative change in the R_g values, as a function of crowder density, for the unconfined (red) and confined (blue) cases. The values are computed relative to the case of lowest crowder density considered in the study ($\phi_c^{min} = 0.035$). Each data point is averaged over 10 different initial conditions.

duction at highest values of crowder densities. This suggests that under confinement, the polymer conformation is already somewhat compact and that the addition of crowder particles thus does not change the global conformation significantly. At the highest crowder densities considered in the present study, R_g values of unconfined and confined polymer are comparable. However, introducing an attraction between monomers, modelling poor solvent conditions, can affect the conformational landscape of the polymer. This will be explored in later sections.

Confined polymers in a good solvent with attractive walls

In this section, we explore the conformations of a long polymer interacting with an attractive wall and under good solvent conditions. Representative snapshots of the systems for different wall attraction strengths and crowder densities are shown in Figure 4.3. In the previous section, we showed that in the confined case and for repulsive walls, the global conformation of the polymer varies little with crowder particle density. Figure 4.3(a) shows that for attractive wall interactions, there is

only a marginal change in the overall conformation of the polymer, provided a good solvent condition is maintained.

To quantify this visual observation further, we computed two shape parameters for the polymer: (i) asphericity (b) and (ii) radius of gyration R_g , both as a function of crowder density. In addition, we also compute the number of adsorbed monomers on to the confining surface also as a function of crowder density. The variation of R_g values plotted against crowder density for a range of attractive wall strengths is shown in Figure 4.3(d). This figure shows that the conformation of the polymers is largely insensitive to the crowder density, even at the highest crowder densities we consider. This is in contrast to the repulsive wall case discussed in the previous section.

This result suggests that the attractive wall interactions dominate the conformational landscape of the polymer when it is confined under good solvent conditions. A small reduction in R_g values upon increasing the crowder density is only seen when the attractive wall strength is small, for $\epsilon_{mw} = 1.0$ in the figure.

These results are mirrored in the plots of asphericity as a function of crowder density shown in Figure 4.3(e). At the largest values for the attractive wall interaction, b values are relatively insensitive to crowder densities, but appear to exhibit somewhat unusual and non-monotonic behaviour for intermediate values of crowder density and wall interaction. To further understand the adsorption of the polymer on to the confining wall surface, we measure the number of adsorbed monomers on the surface (f_{ad}) for different wall attraction strengths as a function of crowder densities. We consider a monomer to be adsorbed on the surface if it is within 1.5σ of the wall. Each point in the plot represents an average of 5 initial conditions and is averaged over 5×10^6 time steps.

For the lowest values of wall attraction strength and for a small number of crowder particles, the number of adsorbed monomers is very small, suggesting a largely

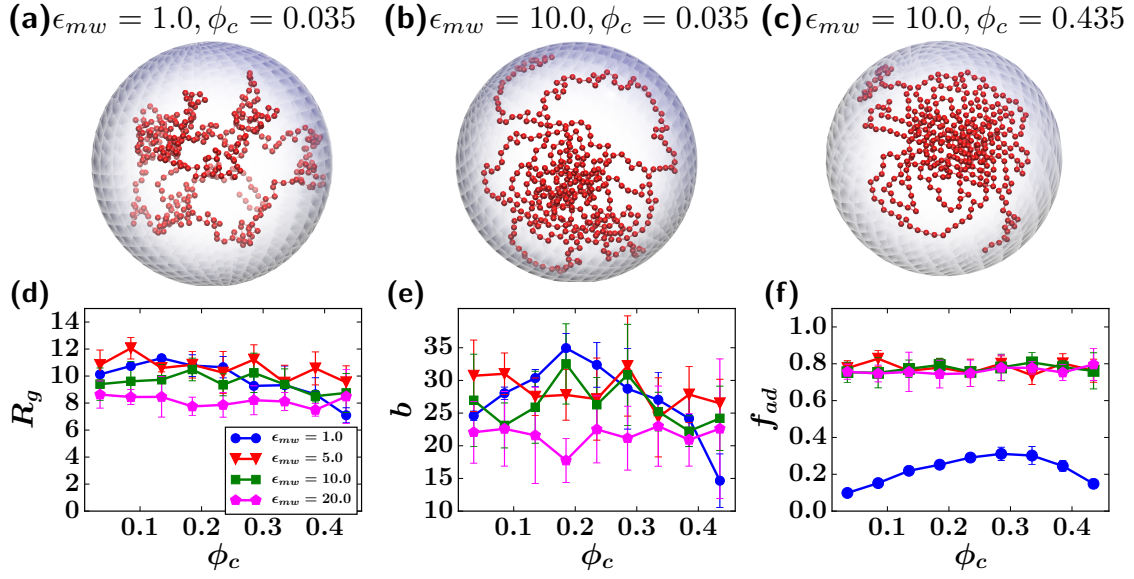


Figure 4.3: Good solvent condition: The snapshots of the polymer conformation for (a) the wall attraction $\epsilon_{mw} = 1.0$, the crowder density $\phi_c = 0.035$, (b) $\epsilon_{mw} = 10.0, \phi_c = 0.035$, (c) $\epsilon_{mw} = 10.0, \phi_c = 0.435$. The variation of (d) radius of gyration R_g , (e) asphericity b and (f) the fraction of adsorbed monomers f_{ad} with ϕ_c for different ϵ_{mw} .

desorbed-extended (DE) configuration of the polymer. However, as the crowder density is increased, there is an increase in the number of adsorbed monomers on the surface. This observation is consistent with our results for the R_g and b values of the polymer for low attractive wall strength and highest crowder density, where we noted that the polymer tends to have a more compact structure and the effects of crowder particles dominate. However, as the wall attraction strength is increased, i.e. for $\epsilon_{mw} > 1.0$, there is a substantial increase in the number of adsorbed monomers, as indicated by the adsorption of nearly 80% of monomers, in Figure 4.3(f). This does not vary much with crowder density and the polymer remains in an adsorbed-extended (AE) state under good solvent conditions for high attractive wall strengths.

We believe that the non-monotonic behaviour of the asphericity in Figure 4.3(e) is likely due to the fact that the polymer shape is considerably distorted by its interactions with the surface and its spreading. At low values of wall interaction, both Figure 4.3(d) and Figure 4.3(e) suggest that the polymer is largely detached from

the wall. At the highest values of wall interaction, the polymer is largely adhered to the wall. For values of the wall interaction that lie in-between these extremes, although most monomers are adhered to the wall on average, excursions from it are not penalized as much, especially at low crowder concentrations. As the polymer shifts between a largely three-dimensional to a largely two-dimensional conformation, the nature of the depletion interaction induced by the crowders can exhibit a non-trivial dependence on crowder density, which we suggest may be responsible for the complex behaviour we see.

Confined polymers in a poor solvent with attractive walls

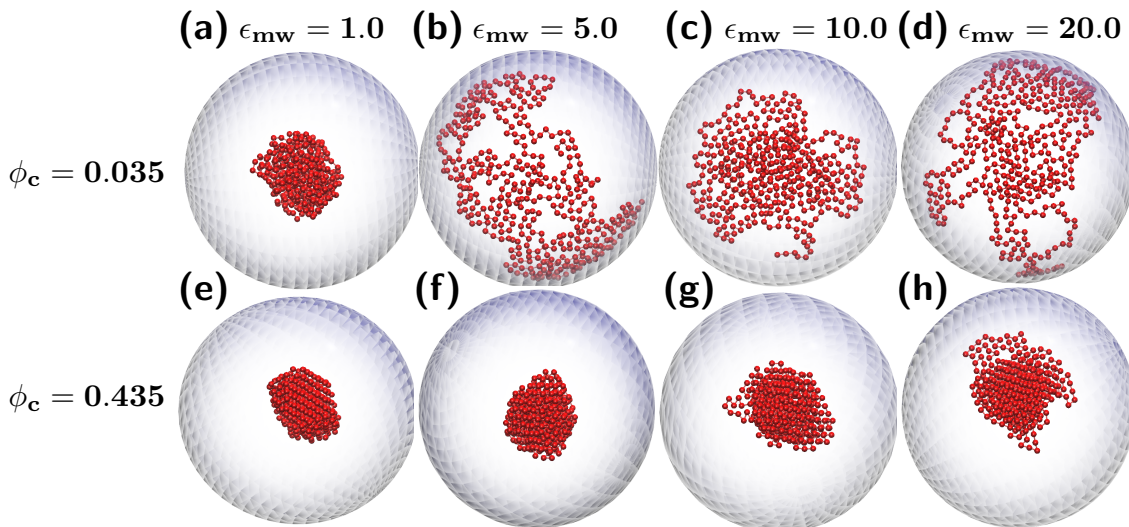


Figure 4.4: Poor solvent: The snapshots of the polymer for low crowder density $\phi_c = 0.035$ and for high density $\phi_c = 0.435$ for different wall attractive strengths.

A neutral, unconfined polymer is collapsed under poor solvent conditions. In this section, we explore confined polymer conformations under poor solvent conditions and near an attractive wall. We vary the strength of the interaction with the wall as well as the crowder particle densities, mapping out the qualitative phases obtained with these parameters.

For low crowder densities, $\phi_c = 0.035$, and for a small monomer-wall attractive

strength $\epsilon_{mw} = 1.0$, the polymer assumes a globular conformation on average. This can be seen in Figure 4.4(a). If we now increase the attraction towards the wall, keeping crowder densities the same, the polymer extends while remaining adsorbed on the wall surface (AE), as seen in Figure 4.4(b-d)). However, at high crowder densities, the polymer remains in an adsorbed collapsed conformation (AC), regardless of the wall interaction strengths, as shown in Figure 4.4(e-h). This is in contrast to what was obtained for good solvents, for which the polymer remains in an AE conformation at sufficiently large wall interaction strength, irrespective of crowder densities.

The coverage of the polymer onto the confining surface in poor solvent conditions differs significantly from that in good solvent conditions. This can be understood in terms of two opposing effects. The polymer wants to maximize its (attractive) interactions with the wall by spreading out over it, but this competes with a tendency towards compaction induced by the poor solvent and exacerbated by the presence of crowder particles. This tendency is present even for low crowder densities. To gain further insight, we calculated the conformational parameters R_g , b and f_{ad} , for different attractive wall strengths and as a function of crowder densities. These results are shown in Figure 4.5(a-c).

For an attractive wall strength of $\epsilon_{mw} = 1.0$, regardless of the crowder density, the polymer is in a collapsed conformation. At the lowest crowder density, as the attractive wall strength increases across $\epsilon_{mw} = 5.0, 10.0$ and 20.0 , the R_g values are increased, suggesting a transition from desorbed-collapsed (DC) to the adsorbed-extended(AE) structure of the polymer. At these higher attractive wall strengths, the crowder density influences the polymer conformation significantly under poor solvent conditions. This is in contrast to good solvent conditions, under which the crowder density has a far smaller effect on the polymer conformation.

In addition, under poor solvent conditions, as the crowder density increases, the

polymer makes a second transition from adsorbed-extended (AE) to adsorbed-collapsed (AC), as can be seen from the decrease of the R_g values in Figure 4.5(a) for higher crowder densities. This can also be seen in calculations of the asphericity Figure 4.5(b), where, at high crowder densities, regardless of the wall attraction, the polymer assumes a compact conformation. This contrasts to the behaviour in good solvent conditions. The number of adsorbed monomers on the wall surface also show a similar decrease at high crowder densities, as shown in Figure 4.5(c).

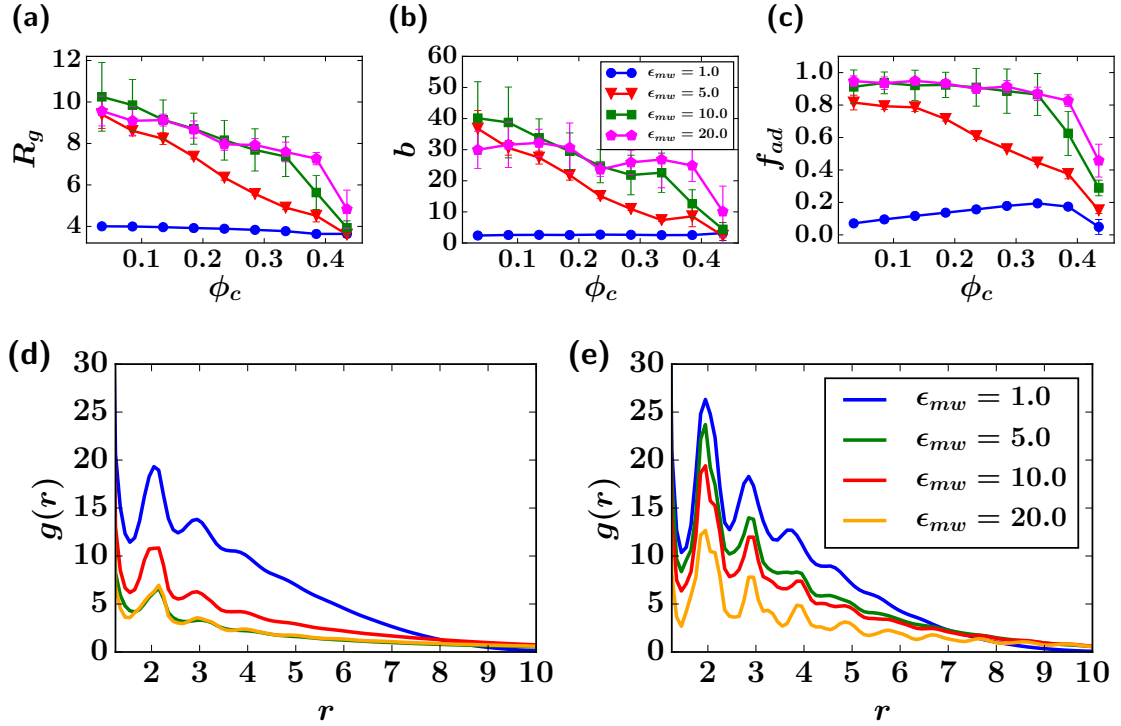


Figure 4.5: Poor solvent: **(a,b,c)** Different shape parameters of the polymer for various attractive wall strengths as a function of crowder density. The pair radial distribution functions for **(d)** low crowder density $\phi_c = 0.035$ and **(e)** high density $\phi_c = 0.335$ for different wall attractive strength ϵ_{mw} .

Though the R_g values of the polymer, under poor solvent conditions and for high attractive wall strengths, is similar to that of the polymer under good solvent conditions, the internal structure of the polymer at low and high crowder densities is very different. This is captured by radial distribution functions ($g(r)$) between monomers. Our results are shown in Figure 4.5(d-e). The $g(r)$ values of the polymer under poor solvent and at high crowder density clearly show a more ordered

internal structure when compared to low crowder density. This is seen in the increased number of peaks emerging in pair distribution function between monomers. The internal structure is more pronounced at low attractive wall strengths while the competing wall interactions at higher strengths lead to reduced structure.

Consolidating these results provides us a global picture of the possible conformations of a neutral polymer in the $\phi_c - \epsilon_{mw}$ space under poor solvent conditions and the competing effects that favour different conformations. First, a small value for the wall attraction leads to an adsorbed collapsed (AC) structure. Upon increasing the crowder density, the polymer maintains this AC structure. As the attraction of the polymer towards the wall is increased, the AC state opens up in order to maximise contact with the wall. There is then a transition towards an adsorbed-extended (AE) as well as layered structure at low crowder density. If we now increase crowder density, the polymer tries to collapse further to avoid exposure to the crowder particles. The competition between the attractive interactions between monomer and wall and the repulsive interaction between the polymer and the crowder particles now governs polymer shape and internal structure. For intermediate ϵ_{mw} values, the crowder interaction appears to be dominant while for higher values of ϵ_{mw} , the attraction wins, leading to an absence of layering even at higher crowder densities.

Confined polymers with attractive walls: The role of crowder density

In this section, we compare the conformations and internal structure of the polymer as a function of crowder densities. Some conformations of the polymer, along with R_g and f_{ad} calculations are shown in Figure 4.6. These are shown for both good and poor solvent conditions as indicated, plotted as a function of crowder densities and for a fixed wall attraction strength ($\epsilon_{mw} = 10.0$) From Figure 4.6, it can be seen that for poor solvents, the polymer adapts an extended conformation on the confining spherical surface, if the attractive wall strength is large and the crowder density low.

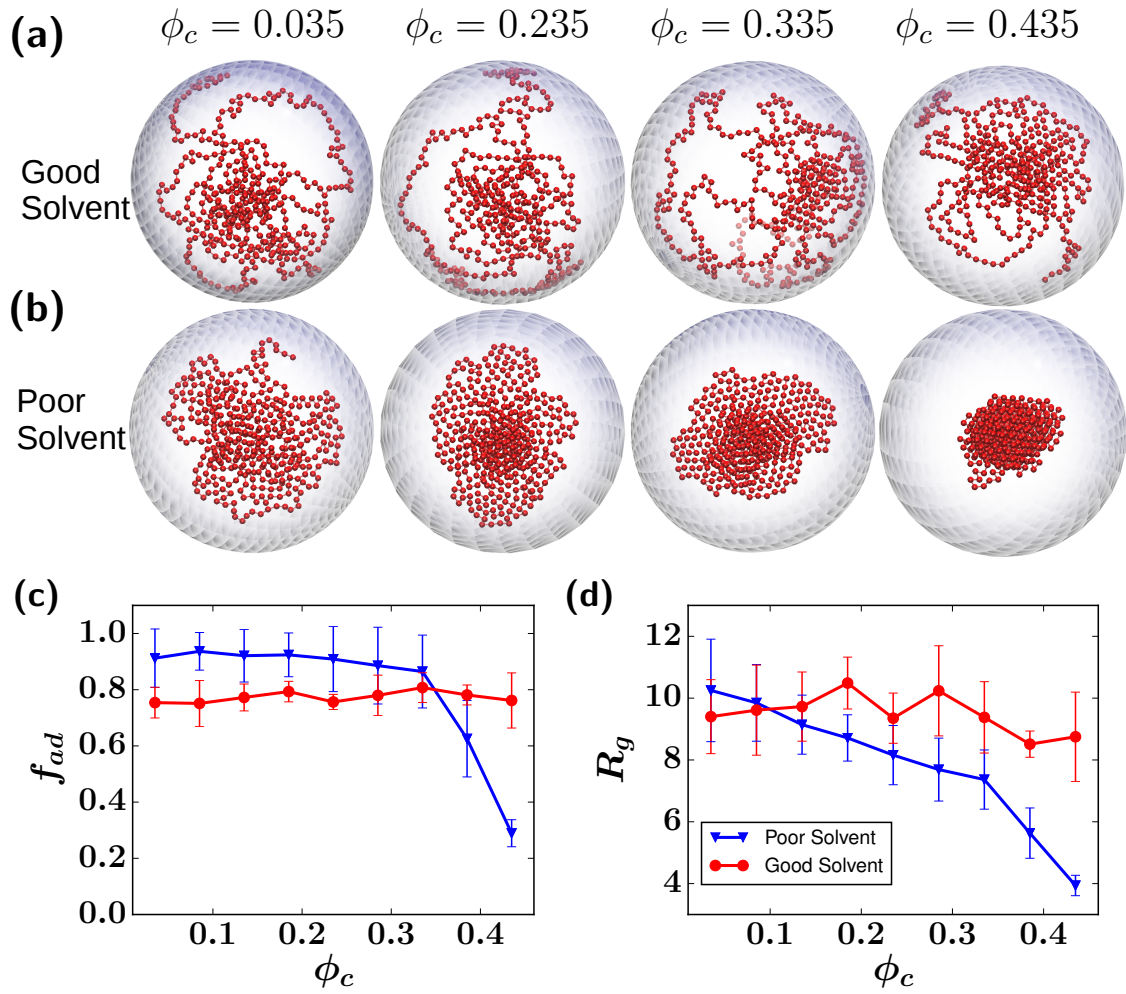


Figure 4.6: The snapshots of the polymer **(a)** for good solvent condition **(b)** for poor solvent condition at different crowder densities $\phi_c = 0.035, 0.235, 0.335, 0.435$ for attractive wall strength $\epsilon_{mw} = 10.0$, **(c)** Fraction of adsorbed monomers on the surface of confinement as a function of crowder density in good and poor solvent conditions. **(d)** The radius of gyration of polymer as a function of crowder density for $\epsilon_{mw} = 10.0$.

However, as the crowder density is increased, the polymer configurations undergoes a transition from more extended configurations to a collapsed configuration. This is in contrast to good solvent conditions, for which polymer conformations are relatively insensitive to crowder density, as shown in Figure 4.6(a).

The calculated values of R_g and f_{ad} as a function of crowder densities in Figure 4.6(c-d) quantify the transition from extended to collapsed polymer conformations in poor solvent conditions and at high crowder densities. We contrast these results to the

case for low crowder density in Figure 4.4(a) where, as the attractive wall strength is increased, a first transition from collapsed to extended conformation (AC to AE phase) in poor solvent is observed. While that transition was driven by the attractive wall strength, the transition from extended to collapsed shown in Figure 4.6 (b) in the poor solvent case is driven by crowder density.

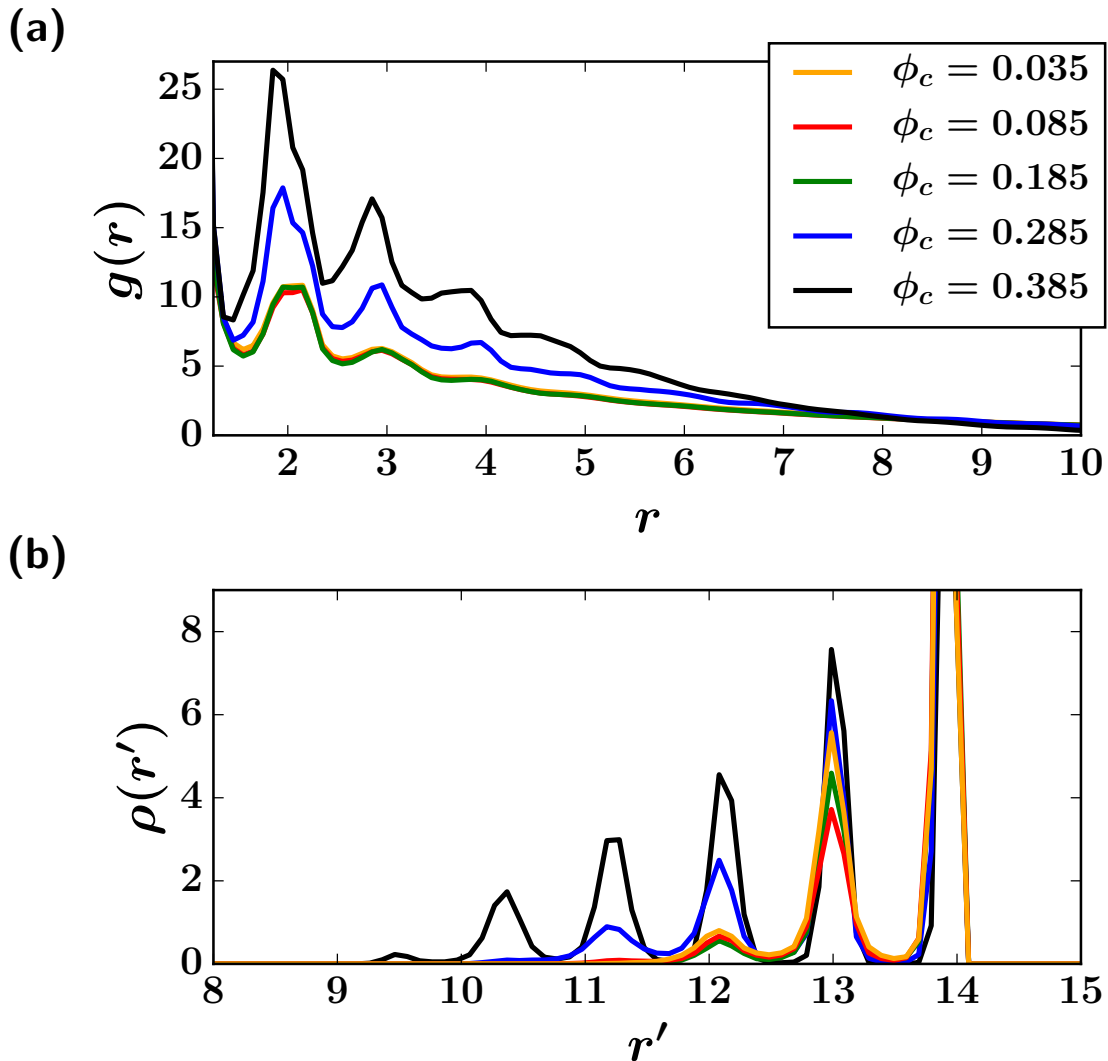


Figure 4.7: For poor solvent condition and $\epsilon_{mw} = 10.0$ (a) the radial distribution function $g(r)$, (b) the density function $\rho(r')$ for $\phi_c = 0.035, 0.085, 0.185, 0.285, 0.385$.

To investigate structure in the conformation of the extended polymer at high wall interaction strength, we calculate the radial distribution function $g(r)$. For fixed monomer-wall interaction ($\epsilon_{mw} = 10.0$), as ϕ_c is increased, the order in the structure

increases (see Figure 4.7 (a)). To understand the positioning of the polymer relative to the wall, we plot the normalized density, $\rho(r')$, of the polymer vs. the radial distance r' (see Figure 4.7 (b)) from the center of the sphere. To calculate $\rho(r')$, we split the spherical volume in a large number of thin shells and count the number of monomers in each shell, normalizing this with respect to the average density obtained if the monomers were distributed uniformly throughout the volume. This density distribution $\rho(r')$ gives us insights into the layering of the polymer upon increasing crowder density.

Our results suggest that, as the crowder density is increased, there is an emergence of layering with respect to the surface. For lower crowder density, there are fewer layers. As we increase the crowder density in the system, more layers begin to appear, as seen in Figure 4.7 (b)). This can be understood in the following way. In poor solvent conditions, as we increase the number of crowder particles in the system, the polymer tries to collapse in order to avoid the exposure to the crowder particles. However, since monomers are attracted towards the wall, a fully globular conformation cannot be sustained. This leads to a partial layering near the wall and hence to the peaks in the density plot. The emergence of internal structure can also be captured via time-averaged contact maps shown in Figure 4.8. The contact maps show that as the crowder density increases, the number of contacts increase in general, suggesting an increase in local density. There are also significant contacts between monomers which are far apart along the sequence, consistent with the visual identification of the collapse of the polymer with increasing crowder density.

A crumpling transition induced by crowders

To better characterize the "crumpling" of the polymer under the combination of poor solvent conditions and high crowder densities, we plotted the maximal height of the polymer from the surface as a function of crowder density, for all wall interaction

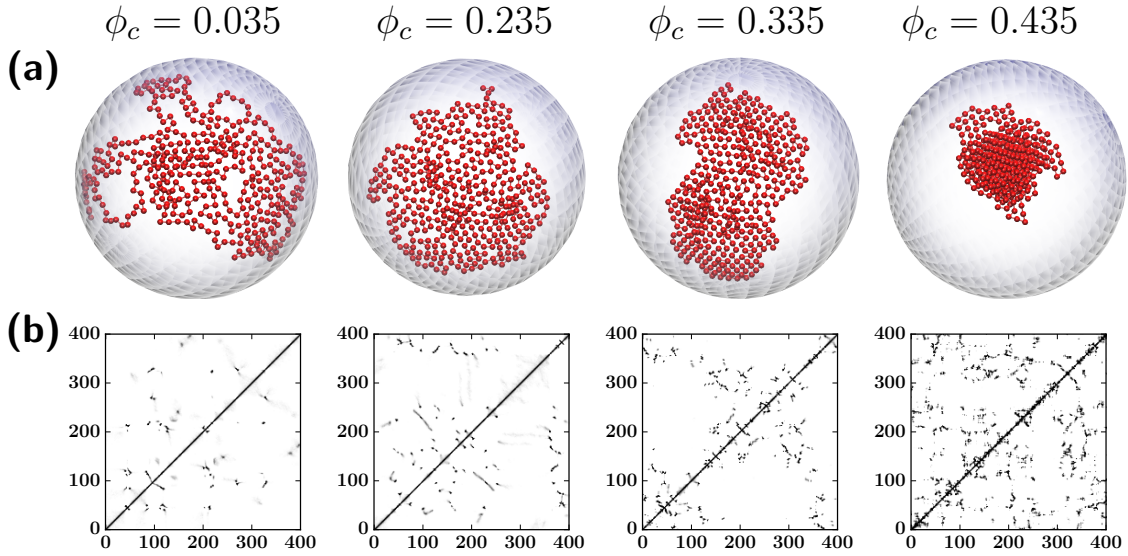


Figure 4.8: For poor solvent condition and $\epsilon_{mw} = 20.0$: **(a)** Snapshots of the system for different values of ϕ_c , and **(b)** Corresponding contact maps averaged over the final 5×10^6 time steps.

strengths (see Figure 4.9(a)).

Some intuition for the maximal height can be obtained from side-views of the system as a function of crowder density, as shown in Figure 4.9(b). At low crowder densities, increasing the strength of the attractive interactions between monomers and wall results in the polymer spreading on the surface. This is evident in the height profile at the smallest crowder density considered ($\phi_c = 0.035$). The highest height is achieved for the smallest wall attraction strength, where the polymer assumes a collapsed conformation. When the attractive strength of the wall is small ($\epsilon_{mw} = 1.0$), the height function is largely independent of the crowder density except at the largest crowder density, where the compactness of the polymer increases. However, for other attractive wall strengths, the dependence of the height function on the crowder density is more complex. For an attractive wall strength of $\epsilon_{mw} = 5.0$, the initial configuration of the polymer is more extended (as can be seen from the difference in heights even at the smallest crowder density). However, the extended-to-collapsed transition is initiated at a lower density than in the case of $\epsilon_{mw} = 1.0$. For higher wall interactions, the extended-to-collapsed transition occurs at higher

crowder densities.

Our results suggest the following: The polymer in poor solvent conditions near an attractive wall experiences two competing forces. These favour, independently, compaction and spreading on the wall. The propensity to collapse would lead to a higher height function. This is primarily driven by crowder particles. The propensity of the polymer to spread along the surface arises from its attractive interactions with the surface. The interplay between these determines the eventual conformational landscape of the polymers at the interface. For low attractive wall strength $\epsilon_{mw} = 5.0$, a smaller threshold crowder density is required for collapse (for $\phi_c < 0.235$). We thus see an increase in the height function. As the strength of the attraction towards the wall is increased, the threshold crowder density after which the polymer starts to collapse moves towards higher crowder density, as seen for $\epsilon_{mw} = 10.0, 20.0$. At the highest crowder densities ($\phi_c = 0.435$), irrespective of wall interactions, the polymer under poor solvent conditions is predominantly in a collapsed state, as evident in the height function.

Snapshots of the collapsed polymer in poor solvent conditions under lowest and highest crowder densities are shown in Figure 4.10(a,b). The figure shows two collapsed structures obtained under two very different conditions. From the visual images, we can already see internal structure in these at high crowder density. To quantify the emergence of internal structure in the collapsed conformation at high crowder densities, we calculated the pair distribution function for the two collapsed phases. These results are shown in Figure 4.10(c). The presence of strong peaks in the distribution function, for the case of high crowder density, clearly indicates increased structure in the collapsed conformations compared to the case for lower crowder density.

To further quantify local structure, we calculate the average number of neighbours for each monomer and plot it as a function of monomers in Figure 4.11. From the

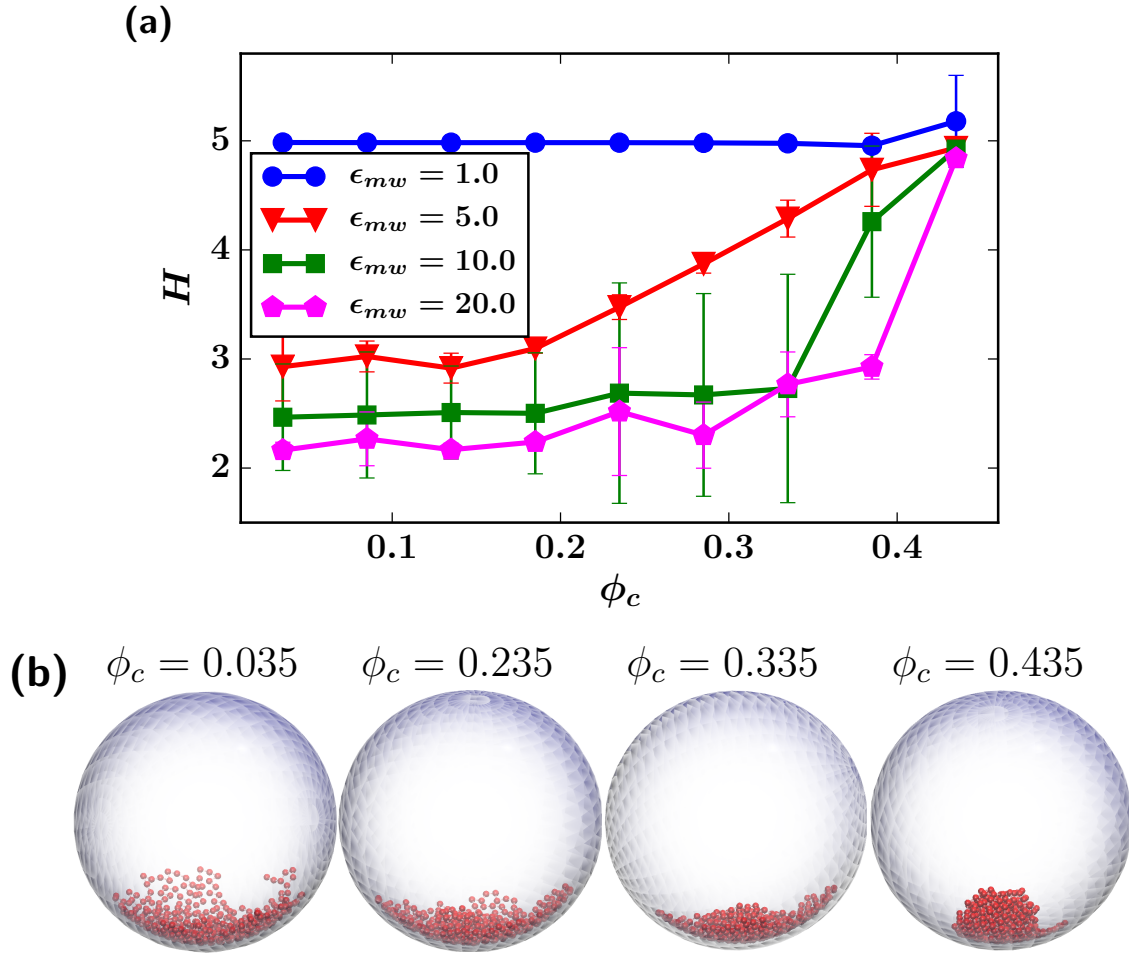


Figure 4.9: (a) The maximum height of the polymer stack along the radial direction. The height of the stack decreases as the strength of the attraction increases and more and more monomers are recruited along the wall of the confinement. (b) The snapshots of the polymer conformation in poor solvent condition for the different crowder densities.

results, it can be seen that the average number of neighbours, barring the monomers on the surface of the collapsed conformation, is around 9, which is very different from the low crowder density case. This suggests that the polymer assumes a more ordered collapsed phase at high crowder density and a more amorphous collapsed phase at low crowder density.

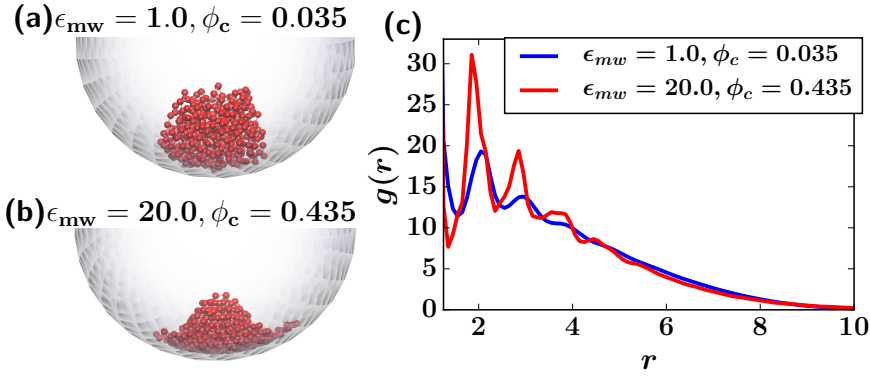


Figure 4.10: Snapshots of the system in a poor solvent for **(a)** $\epsilon_{mw} = 1.0, \phi_c = 0.035$, **(b)** $\epsilon_{mw} = 20.0, \phi_c = 0.435$ and **(c)** the pair radial distribution function of polymer for parameters of **(a)** and **(b)**. For lower wall attraction ϵ_{mw} and lower density value $\phi_c = 0.035$, the plot suggests less order while for the higher wall attraction $\epsilon_{mw} = 20.0$ and higher crowder density $\phi_c = 0.435$, $g(r)$ shows many peaks indicating more order in the system.

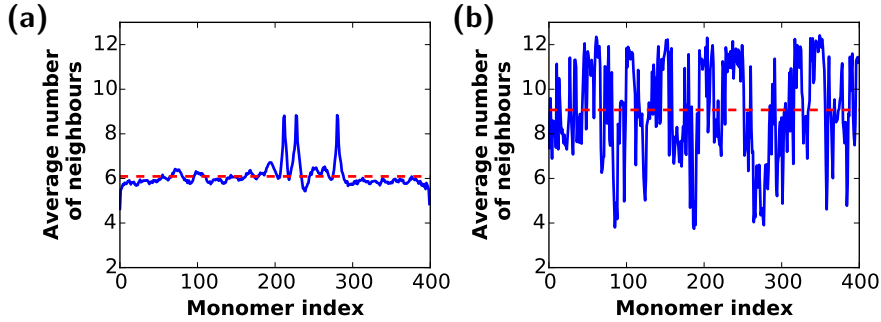


Figure 4.11: Average number of neighbours for **(a)** $\epsilon_{mw} = 1.0, \phi_c = 0.035$ and **(b)** $\epsilon_{mw} = 20.0, \phi_c = 0.435$. The average number of neighbours for higher density ($\phi_c = 0.435$) and higher wall attraction ($\epsilon_{mw} = 20.0$) system is about 9 which is higher than that for lower wall attraction ($\epsilon_{mw} = 1.0$) and lower crowder density ($\phi_c = 0.035$) system. This suggests that polymer is more ordered in the higher crowder density system than for the lower density system.

4.1.3 Discussion and Conclusion

In this part, we used molecular dynamics simulations to describe the conformational landscape of a confined polymer in the presence of attractive walls as well as crowder particles. We varied solvent quality across good and poor solvent conditions. We used a 400–monomer long polymer, exploring the parameter space of the density of crowder particles, the strength of wall interactions and the quality of the solvent.

The conformation of a polymer on a surface has been the subject of a number of earlier studies [Rajesh et al., 2002, Bachmann and Janke, 2005, Plascak et al., 2017, Martins et al., 2018]. The nature of polymer configurations depends on the curvature of the surface [Arkin and Janke, 2012b, Bachmann and Janke, 2005, Möddel et al., 2014], solvent quality [Reddy and Yethiraj, 2010], boundary conditions, and the interaction energy between the surface and the polymer.

Earlier Monte Carlo studies [Möddel et al., 2014] showed that polymers display a number of shape transitions near an attractive planar surface. This work suggested a pseudo phase-diagram in the $\epsilon_{mw} - T$ plane. In this phase diagram, at low temperatures, the polymer assumes a layered adsorbed crystalline shape. At higher temperatures, the polymer is desorbed if the surface attraction is small, while the polymer remains adsorbed for high surface attraction. Similar shape transitions are seen for polymers on curved surfaces [Arkin and Janke, 2012b].

As we show, the situation is considerably more complex when the polymer is confined, thereby reducing its allowed fluctuations. We showed that for poor solvents, as the attractive interaction strength between the wall and the polymer was increased, the polymer exhibited a shape transition from an adsorbed globule (AG) to an adsorbed layered (AL) phase. For intermediate values of ϵ_{mw} , as the number of crowder particles was increased, polymer configurations changed from the AL state to an adsorbed collapsed (AC) state. In good solvents, at low surface attraction, the polymer did not completely adsorb on the surface. As the surface attraction was increased the polymer gradually adsorbed on the attractive surface.

The curvature of the confining sphere plays an important role in the selection of conformations. In order to understand the effect of the curvature on the conformation, we simulated the system of polymer of same length in a sphere with larger radius $R = 30.0$ with the total volume fraction from 0.035 to 0.435 for $\epsilon_{mw} = 10.0$.

We observed layered structures in proximity to the wall, as seen from the difference

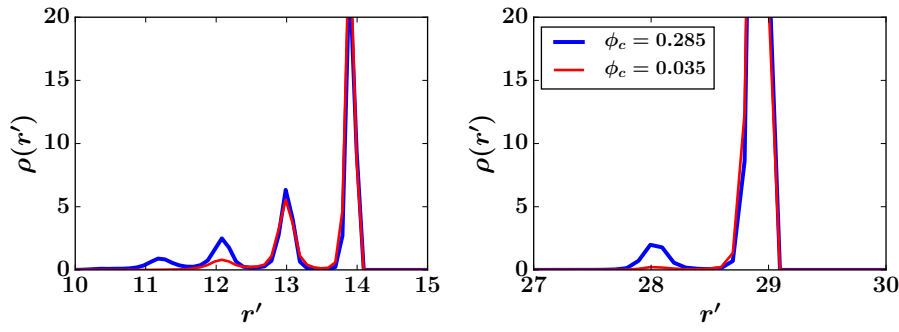


Figure 4.12: The density function of the monomers in poor solvent condition confined within attractive walls (a) for the sphere of radius $R = 15.0$ (b) for the sphere of radius $R = 30.0$.

in number of peaks (suggesting layers of stacked monomers) when the radius of confining sphere was doubled (see Figure 4.12). As the radius of the confining sphere is increased, the number of secondary peaks decreases. For the larger sphere, all the monomers are adsorbed on the surface at low ϕ_c . As the density of crowders is increased, a second layer appears. For the smaller system, there are multiple layers present even at the smaller density of crowders. These results suggest that the confinement and the relative ratio of confining sphere radius and length of the polymer can significantly alter the conformational landscape of the polymers. In particular, smaller confinement radii can lead to more substantial layering, presumably because the smaller sphere frustrates the formation of the adsorbed monolayer that is a feature of the sphere with larger radius. These features can all be tuned by the density of crowders, providing a second axis to adjust the properties of the adsorbed state. The density function describes the normalized number of particles at a given distance r' from the center of the confinement. The density function plots for monomers indicate that for the system with $R = 15.0$ and $\phi_c = 0.035$, there are two layers of monomers. Increasing the ϕ_c to 0.285 leads to multiple peaks (see Figure 4.12(a)) which is an indication of the onset of collapse of the polymer to a globular conformation. In the case of the system with larger radius $R = 30.0$ and for $\phi_c = 0.035$, all the monomers are adsorbed on the surface while increase in ϕ_c value to 0.285, some of the monomers associate to the top of the monomer layer,

indicated by the emergence of the second peak in the density function plot (see Figure 4.12(b)).

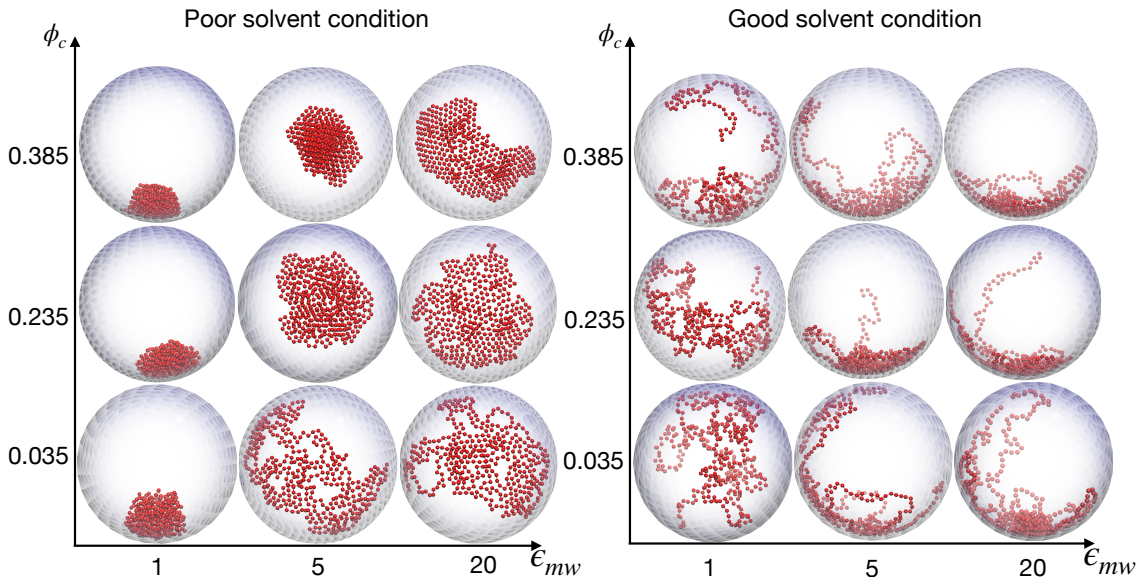


Figure 4.13: Conformations of polymer under different crowder densities and attractive wall strengths for the poor and good solvent condition in $\phi_c - \epsilon_{mw}$ space.

In this study, in addition to the interacting surfaces and solvent condition, we discussed the role of another critical variable associated to crowding of the polymer chain by other monomeric particles. The quantity ϕ_c was found to play an important role in determining the conformation of the polymer. In good solvent conditions, we found that the crowder particle density did not affect the conformations substantially. In poor solvent conditions however, for higher levels of wall attraction, an increase in number of crowder particles leads to a more ordered structure. We suggest that this may be a general feature of crowded confined polymers in a poor solvent, when attracted by a wall, and that the ability to adjust solvent quality as well as crowder concentration may be key to stabilizing a polymer in the vicinity of a confining wall.

The addition of crowder particles adds additional complexity but presumably pro-

vides a better representation of a large number of biological situations. Indeed, the combination of confinement, crowding and wall interactions should be generic to a number of polymer systems of biological and pharmacological relevance. More detailed studies of these regimes, keeping specific systems in mind, and including the size effects of the crowders under these conditions should be fruitful.

4.2 Diffusion in Crowded and Grafted Cylindrical Tube

Understanding particle mobility in confined porous channels is crucial to various processes including ion transport across membranes via ion channels, translocation of biopolymers through confined spaces, the extraction of oil etc. [Wang et al., 2019, Peteu, 2007]. Polymers that are grafted on the surface of a hollow channel-forming cylinder, especially coating the inside of such channels, are interesting systems that can be used to tailor the transport of various solutes. Such structures also play an important role in the design of microfluidic and nanofluidic devices with specified properties [Yu et al., 2003, Speyer and Pastorino, 2019, Zuo et al., 2017]. These properties can be modified by tuning the polymer-channel surface interactions, temperature, pH, crowder particle density and the nature of crowder particles also present within the channel. [de Groot et al., 2013, Conrad and Robertson, 2019, Speyer and Pastorino, 2019]. These alter the conformation of polymers lining the channel, allowing for flow through them to be controlled.

This, in turn, can influence the transport properties of particles within channels [Reznik and Landes, 2012, Adiga and Brenner, 2005]. Other factors influencing particle mobility include the length of the grafted polymers, the grafting density of the polymers on the surface, particle-surface interactions and the effective particle size itself. Many of these factors can impede the motion of the particle and contribute

to caging behavior, providing the ability to tune the diffusion of particles [Filippidi et al., 2007, Choi et al., 2014].

Polymer brushes also offer a unique porous environment to the particle motion [Zhang and Müller, 2005, Brittain and Minko, 2007, Dimitrov et al., 2006]. Most studies of particle motion through porous media use systems where the pore/cavity size is uniform and fixed in location. Determining aspects such as mean first passage times and translocation of solutes through cavities is a challenging prospect for even static cavities. Whether making pores effectively dynamic should impede or accelerate particle motion is not intuitive.

The diffusion coefficient D provides a measure of how easy it is to move a particle of fixed size in a given environment where it is only subject to thermal fluctuations [Jacobs, 1935]. The diffusion of tracer particle inside nanopores formed by lining cylindrical channels with polymer brushes depends upon the solvent condition as well as the density and length of the polymer grafts. It can also be affected by the crowder particles added to the solution. The longer the polymer grafts are, the smaller the effective diameter of the tube will be, as the radius of gyration (R_g) of the polymer in poor solvent conditions is $\sim N^{1/3}$ whereas in good solvent conditions it is $\sim N^{3/5}$, where N is degree of polymerization.

4.2.1 Methods

We study the diffusion of a tracer particle as well as the conformational structure of polymer grafts in a hollow impenetrable cylinder containing a solvent as well as crowder particles. The polymers are grafted on the interior surface of an infinitely long cylinder, which we approximate by applying periodic boundary conditions along the axis of the cylinder of length L . In our simulations, we vary the solvent quality from good solvent to poor solvent. We do not have any explicit solvent particles.

However, we allow for separate crowder molecules, varying the number of crowder particles from 0 to 12000 such that the the crowder density ϕ_c changes from 0.00 to 0.391. The crowder density $\phi_c = N_c v_c / V$, where N_c , v_c and V are the number of crowder particles, volume of a crowder particle and V is the volume of the cylinder.

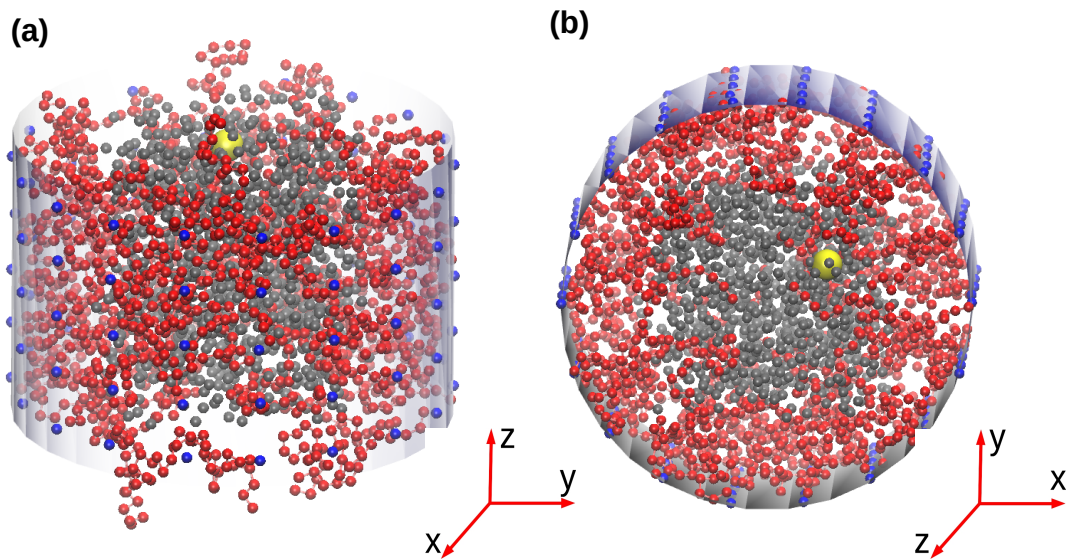


Figure 4.14: Model representation of the simulated system. **(a)** The lateral view and **(b)** the cross-sectional view of the system. The blue color particles represent the anchor monomers, red color particles are the monomers which are not fixed to the cylindrical wall, the crowder particles and the tracer particle are shown in grey and yellow respectively. (Note that tracer particle is shown bigger than the original size for better visualization.)

A bead-spring model is used to simulate polymers. A simple harmonic potential 4.2 is used for the bonded interactions between the subsequent monomers. A shifted and truncated Lennard-Jones (LJ) 6-12 potential 4.1, at a cutoff r_c , is used for pairs of non-bonded interactions between all types of particles, monomers, crowders and tracers. The interaction among the particles determines the effective solvent condition. The interaction of the monomer with the wall is described by a Lennard-Jones potential. Both repulsive and attractive wall interactions between monomers and cylindrical wall are considered. The interaction of the crowder particles to the wall is set to be repulsive regardless of solvent condition. The strength and sign of

the interaction of the polymer with the wall can be varied, so that the full range between repulsive and attractive wall strengths is accessed. The parameters used in this study are given in Table 4.2.

	Good solvent			Poor solvent		
$\mathbf{i} - \mathbf{j}$	ϵ_{ij}	σ_{ij}	\mathbf{r}_c	ϵ_{ij}	σ_{ij}	\mathbf{r}_c
m-m	1.00	1.00	$(2)^{1/6}$	1.00	1.00	2.5
c-c	1.00	1.00	$(2)^{1/6}$	1.00	1.00	$(2)^{1/6}$
m-c	1.00	1.00	$(2)^{1/6}$	1.00	1.00	$(2)^{1/6}$
m-t	1.00	1.00	$(2)^{1/6}$	1.00	1.00	$(2)^{1/6}$
c-t	1.00	1.00	$(2)^{1/6}$	1.00	1.00	$(2)^{1/6}$

Table 4.2: Table of parameters for interaction potential for good and poor solvent conditions. Different values of r_c determine the solvent condition of the system.

The equation of motion is integrated for 10^7 steps using a velocity-Verlet algorithm. The size of time step is taken to be $\delta t = 0.001\tau$. All simulations are performed under constant volume and temperature (T) conditions ($T = 1.0$) using a Nosé-Hoover thermostat. The MD algorithm is implemented using the LAMMPS software package. Snapshots of the system were taken using the VMD package and used to first qualitatively assess changes in configurations across parameter values, prior to quantitative analysis.

The system’s initial configurations is generated using a custom python code. The polymers are grafted on the interior of a cylinder of height 20 units along z -axis and radius 16 units. The degree of polymerization of grafted polymers used is 20 and the distance between the graft is 4 units along z -axis and $\pi/9$ radian radially. The average bond length r_0 for the polymer is taken to be 1.122, and the size of the tracer, monomers and crowder particles are taken to be 1.0, in the units set above.

Five independent simulations are performed at each point in parameter space, using different initial velocities and independent random configurations of tracers and polymers.

To understand the position and structure of grafted polymers, we calculate the

distribution of monomers inside the cylinder. The monomer distribution (P_{mono}) is defined as number of monomers in a cylindrical shell normalized with the number of particles in a uniform distribution. A similar quantity (P_{crow}) is defined for the crowder particles. To further analyze the spatial structure, the pair distribution function $g(r)$ is calculated. We computed different pair distribution functions such as $g_{mm}(r)$, $g_{mt}(r)$, $g_{ct}(r)$, $g_{cc}(r)$ and $g_{mc}(r)$. We also calculated the radius of gyration as a function of solvent quality, crowder density and wall interaction to understand the effective size of the cylindrical tube in which crowders and tracer particles diffuse.

To quantify the diffusive behaviour of tracer particles, we plotted the $\langle(z(t + \tau) - z(t))^2\rangle$ vs τ for them. The diffusion coefficient D was calculated by fitting the long-time linear trend of the mean square displacement (MSD) $\langle(z(t + \tau) - z(t))^2\rangle$ in z -dimension as a function of lag τ .

4.2.2 Results

We fix the grafting density of the polymer inside the cylinder for the current study and introduce a tracer particle and a number of crowder particles to the system. The number of crowder particles is increased from 0 to 12000 in steps of 2000. The interaction among monomers decide the solvent condition of the system. To simulate a good solvent condition, the interaction between the monomers is repulsive whereas for poor solvent condition, it is attractive.

To understand the effect of crowder density ϕ_c on the radius of gyration of the polymer grafts R_g , which in turn provides an approximate estimate of the effective radius of the cylindrical tube, we compute R_g for different number of crowder particles, different solvent conditions and monomer-wall interactions. In Figure 4.15, we see that as the density of crowder particles ϕ_c increases for poor solvent conditions, the average radius of gyration does not change significantly and is independent of

monomer-wall interactions, except at the highest density of crowder particles. On the other hand, for good solvent conditions, the radius of gyration shows a gradual decrease with crowder density ϕ_c . Furthermore, it is seen that the type of monomer-wall interaction, whether attractive or repulsive as well as the strength ϵ_{mw} , do not have a significant effect on the radius of gyration of the polymer grafts.

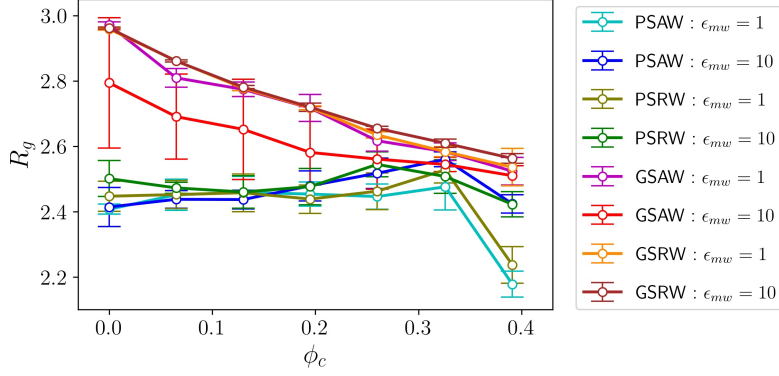


Figure 4.15: The radius of gyration of polymer grafts for poor and good solvent conditions and different monomer-wall interactions. The symbols are abbreviations for, GS: good solvent, PS: poor solvent, AW: attractive wall, RW: repulsive wall.

To investigate further the effect of crowder density on the diffusion of the tracer particle, we plot (see Figure 4.16) mean square displacement (MSD) in the z -direction (along the long axis of the cylinder) $\langle (z(t+\tau) - z(t))^2 \rangle$ against the lag τ for different solvent conditions and monomer-wall interactions. We find that $\langle (z(t+\tau) - z(t))^2 \rangle$ decreases with increasing ϕ_c regardless of solvent conditions and monomer-wall interactions. The fast growth of MSD at small times suggests super-diffusion following $\langle \Delta z(\tau) \rangle^2 \sim \tau^\alpha$ with $\alpha > 1$, where $\Delta z(\tau) = z(t+\tau) - z(t)$. At larger times, for $\phi_c = 0$, the tracer particle shows super-diffusive behaviour, while for $\phi_c > 0$, we see what resembles normal Brownian diffusion with $\Delta z(\tau)^2 \sim \tau^\alpha$ with $\alpha \sim 1$.

To understand the results of Figure 4.16 better, we calculated the values of diffusion constant D from the plots by fitting the MSD at larger time scales for $\phi_c > 0$ to a line using a least-square-fit method for all τ values. We then plotted them against ϕ_c for different solvent conditions and wall interactions. Figure 4.17 shows that the

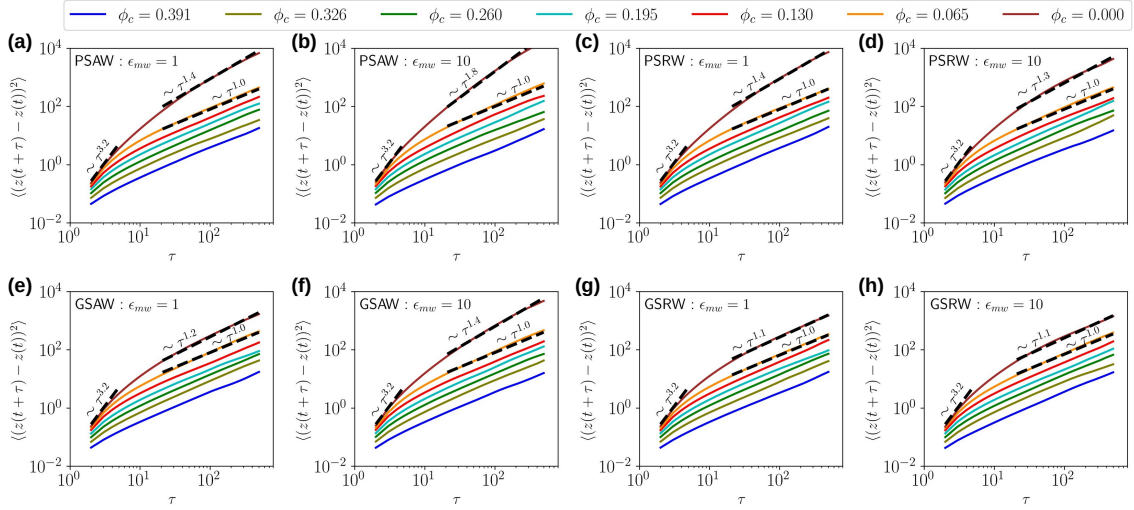


Figure 4.16: The plot shows $\langle (z(t + \tau) - z(t))^2 \rangle$ vs τ for poor and good solvent condition and different wall interactions. Super-diffusive behaviour is seen for $\phi_c = 0$, while behaviour shifts to normal Brownian motion for $\phi_c > 0$.

diffusion coefficient D decreases as the density of crowder particles is increased in the tube, explained by the observation that increasing the number of crowder particles reduces the space for the tracer particle to move.

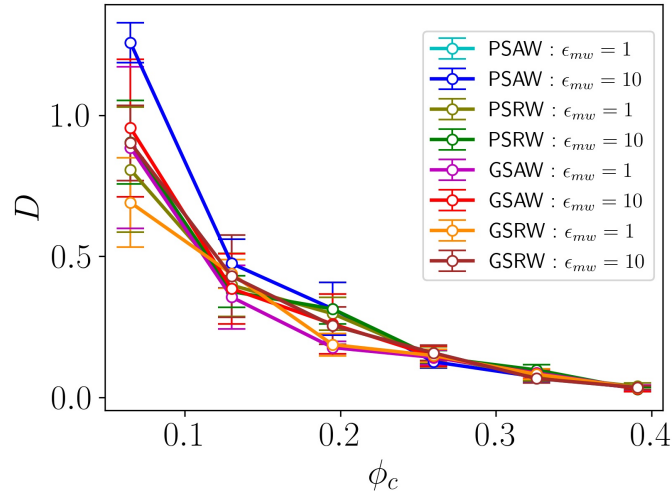


Figure 4.17: The plot shows the diffusion coefficient D vs crowder density ϕ_c for good and poor solvent conditions with different wall-monomer interactions. The diffusion coefficient decreases as more number of crowder particles are added to the system regardless of solvent condition and monomer-wall interaction.

To understand the radial distribution of the particles, we plot the average probability distribution for monomers P_{mono} and crowders P_{crow} (see Figure 4.18) over the last

5×10^5 steps of the trajectory. From Figure 4.18 (a), we see that, in the case of a poor solvent condition and for an attractive wall with monomer-wall interaction strength $\epsilon_{mw} = 1$, the monomers attach only loosely to the cylindrical wall for all ϕ_c . On the other hand as ϵ_{mw} is increased to 10, almost all the monomers attach to the wall, as seen in Figure 4.18(b) as there is one very high peak supplemented with a smaller secondary peak.

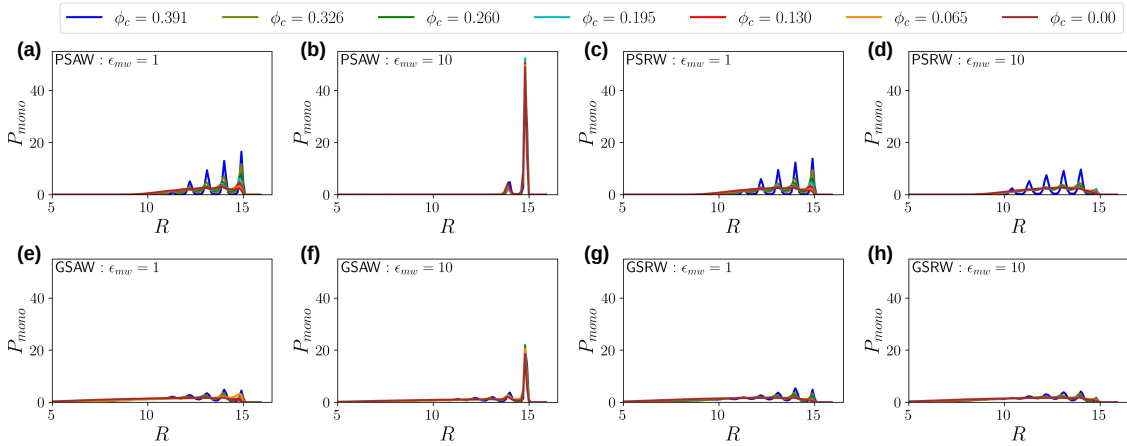


Figure 4.18: The average monomer distribution in the cylindrical confinement for different solvent conditions and monomer-wall interactions. Monomers largely avoid the contact with the wall except for the high attractive interaction strength $\epsilon_{mw} = 10$.

Figure 4.18 (c-d) shows that for poor solvent conditions with a repulsive wall, the polymers attach to the wall of the cylinder only at a single attachment point, preferring to expand out into the solution to minimize their interactions with the wall. Even for attractive walls, in the case of a good solvent condition (Figure 4.18 (e-h)), the monomers largely avoid the wall except at the highest attractions $\epsilon_{mw} = 10$.

We further see from Figure 4.19 that the crowders are uniformly distributed in the volume near the axis of the cylindrical tube ($R = 0$) and exhibit some layering structure regardless of solvent conditions and monomer-wall interactions as they penetrated close to the wall of the tube ($R = 15$). The layering becomes more prominent as the number of crowder particles increases in the system.

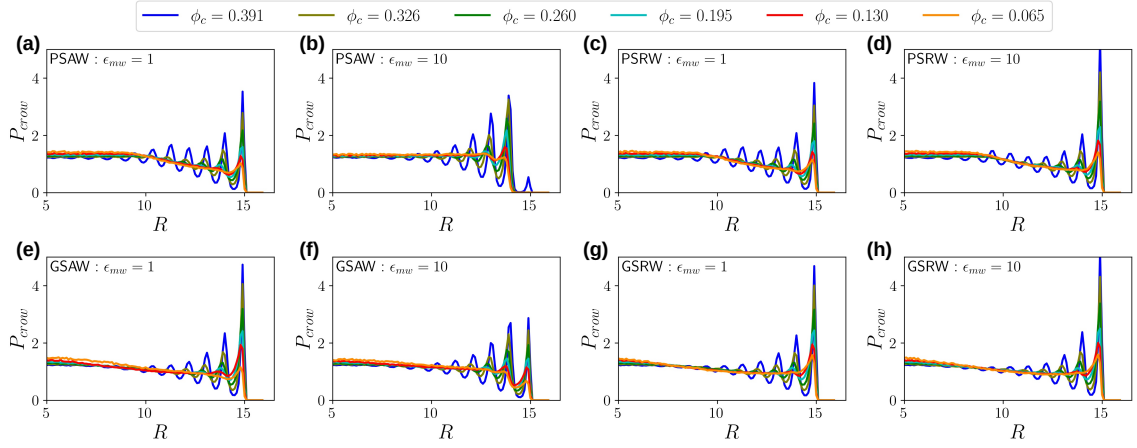


Figure 4.19: The crowder particle distributions for different solvent conditions and monomer-wall interactions. The crowders are uniformly distributed in the middle of the tube while show layering for higher crowder density near the wall of the tube.

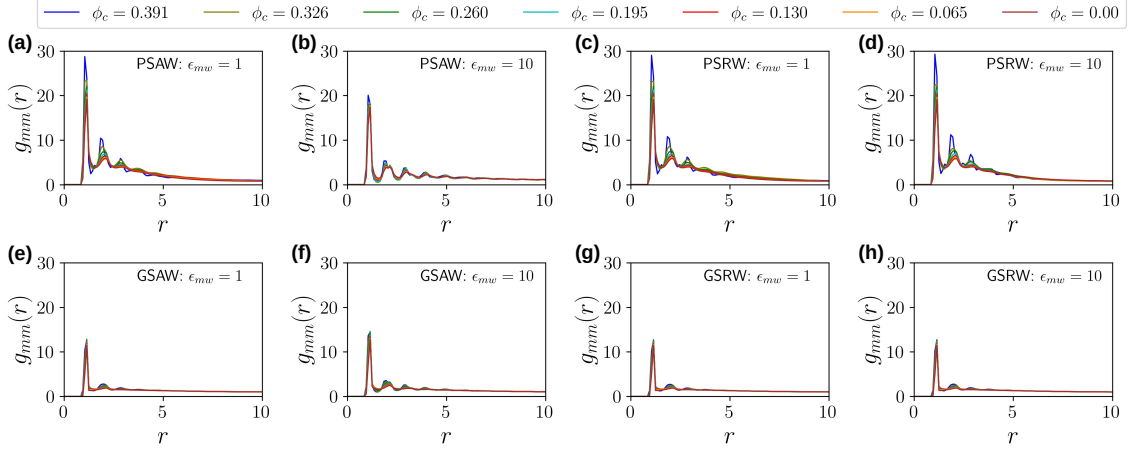


Figure 4.20: The pair distribution function for monomer-monomer pairs. Enhanced ordering is seen in poor solvent conditions whereas for good solvent conditions, this order reduces.

To investigate the structural organization of the system, we also calculate pair distribution functions $g(r)$. Figure 4.20 shows plots of the pair distribution function $g_{mm}(r)$ for monomer-monomer pairs. In the top panel, Figure 4.20(a-d), shows $g_{mm}(r)$ for the poor solvent condition with attractive and repulsive wall for $\epsilon_{mw} = 1, 10$. It is seen that the structure is enhanced with the crowder density ϕ_c . For good solvent condition, the effect of crowder density is to increase the organization, although the effect of ϕ_c is reduced in this case as can be seen from the height of the primary peak (see Figure 4.20 (e-h)).

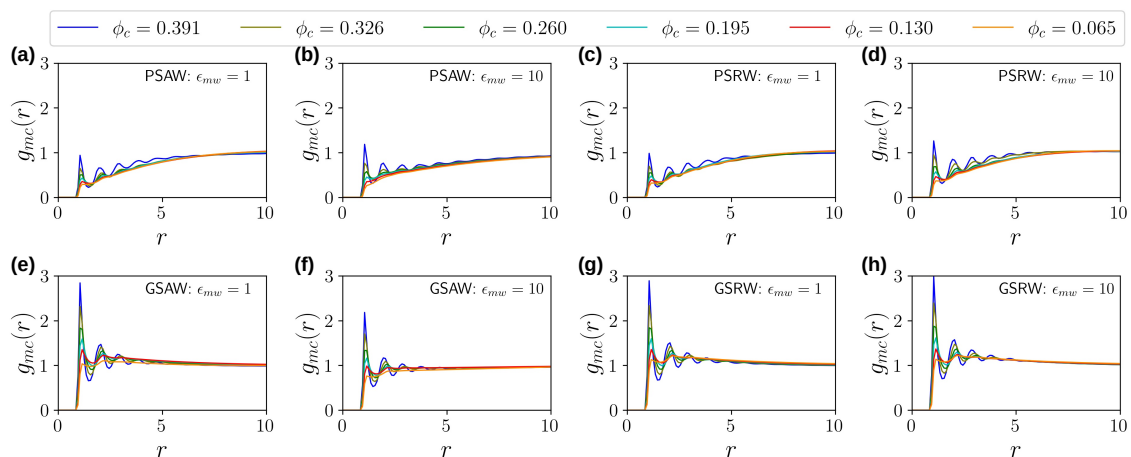


Figure 4.21: The pair distribution function for monomer-crowder pairs. The monomer-crowder pairs are less ordered for poor solvent conditions as compared in the good solvent conditions.

Figure 4.21 shows the pair distribution function for monomer-crowder pairs. For poor solvent conditions, the polymers seem to interact less with the crowder, as the polymer is in a collapsed conformation (see Figure 4.21 (a-d)), but Figure 4.21 (e-h) shows a single peak indicating enhanced monomer-crowder pair structural ordering.

4.2.3 Discussion and Conclusion

In this section, we used molecular dynamics simulations to understand the diffusion of a tracer particle in q cylindrical geometry. This was observed to vary as a function of the conformation of polymer grafts when the cylindrical tube had its internal surface grafted with by a uniform density of polymers. We varied solvent quality across good and poor solvent quality. We varied the number of crowder particles, solvent quality and the monomer-wall interaction to understand their effects on the diffusion of the tracer particles.

We showed that the diffusion of the tracer particle reduces with an increase in the number of crowder particles. We noticed a regime of superdiffusive behaviour in the case where crowder particles were absent. As the size of the tracer becomes compara-

ble to the size of the tube's diameter, we can expect diffusion to become increasingly difficult. We can also expect tracer particle to exhibit caging behaviour [[Schneider et al., 2016](#)] at moderate to higher crowder densities, similar to behaviour seen in tracer-obstacle systems [[Ghosh et al., 2015](#), [Scalliet et al., 2015](#)].

Here, we considered the case where the polymer graft density is kept constant. In experimental systems, however, the polymer graft density plays a significant role in determining the conformations of each grafted polymer. Hence, it would be a natural next step to study the effects of grafting density on the diffusivity of the tracer.

Chapter 5

Conclusion

This thesis studied the properties of confined polymers in biophysical and bioengineering contexts. It studied models of the coupling of stem cell chromatin, modelled as an active polymer solution, with a soft confining nucleus. It then went on to explore the problem of polymers confined within a hollow sphere or cylinder, where the solvent quality, the interaction with the wall and the density of crowders could be tuned separately. This set of models is appropriate in a number of industrial as well as biophysical contexts.

The first of the problems studied dealt with the understanding of auxetic behaviour observed in the nuclei of mouse stem cells. The mechanical properties of stem cells change as they differentiate to specific cell types. In experiments [[Pagliara et al., 2014](#)], it is seen that the nucleus of mouse embryonic stem cell exhibits auxetic behavior in a transition state that intervenes between the pluripotent and differentiation primed state. We developed a simple model which described this auxetic behavior while also providing a broader biophysical perspective on the implications of model results for Waddington's idea of an epigenetic landscape. The main results from the model are summarized below,

- The Poisson's ratio of the nucleus depends upon a coupling parameter B which describes the lowest order coupling of a variable describing the level of chromatin compaction Ψ with the nuclear size R . For positive values of B , the nucleus behaves as normal material with positive Poisson's ratio, whereas for negative values of B , the nucleus exhibits auxetic behavior with a negative Poisson's ratio.
- We can interpret the experimental data in the following way: The value of the parameter B goes from being positive in embryonic stem cell state to negative in transition state to being positive again in differentiation primed state. The nucleus thus transitions from being non-auxetic to auxetic to again nonauxetic states as the cell differentiates. We propose that the auxetic-nonauxetic boundary can be determined by studying time correlation functions of coarse-grained variables. We show that the cross-correlation function $\langle \delta R_{\perp}(0) \delta \Psi(t) \rangle$ should change the sign of its slope as B changes sign.
- We model the dynamics of chromatin compaction variable Ψ constrained by a potential $V(\delta\Psi)$. The chromatin compaction potential can be expected to be complex, possessing multiple minima. It is known that different cell types have different levels of chromatin compaction. We connect Waddington's complex epigenetic landscape to a simple one dimensional potential $V(\delta\Psi)$ by projecting the compaction which should be a function of both space and time to an overall chromatin compaction variable Ψ that depends only on time.

Our model can be generalized in many ways. In chapter 3, we considered Ψ as a function of time t only while neglecting its spatial dependence. This is a good approximation for a relatively fluid stem cell state, although chromatin compaction should really be thought of as spatially inhomogeneous in differentiated states. Hence, including a spatial dependence $\Psi(\mathbf{r}, t)$ should be a first step towards generalization. Also, a coarse-grained simulation of an active polymer in a flexible confinement is

feasible. It will be interesting to see how the arguments of chapter 3 translate to simulations.

In the second problem examined in the thesis, we studied the conformational behaviour of polymers in crowded and confined environment using molecular dynamics. The main results are summarized below,

- To understand the effect of confinement on the conformations of polymer, we compared the results from the simulation of polymer under spherical confinement and periodic boundary condition under the same set of parameters. Under good solvent condition, the polymer assumes a desorbed extended conformations in both the cases but the radius of gyration R_g of the polymer is smaller in case of confinement compared to that in unconfined case.
- To understand the effect of crowder density ϕ_c on the conformations of polymer, simulations of the polymer were carried out varying the number of crowder particles. Under good solvent conditions and confinement by an attractive surface, the polymer is extended and completely adsorbed onto the surface of confinement. Changing ϕ_c does not further change the conformations of the polymer. In case of poor solvent conditions, the polymer collapses and is adsorbed on the surface for moderate value of ϕ_c . It becomes more ordered and compact for higher values of ϕ_c .
- To understand the effect of monomer-wall interaction, the polymer is simulated in good and poor solvent condition with varying monomer-wall interaction strength ϵ_{mw} . The polymer gets adsorbed for all the values of ϵ_{mw} , but the degree of adsorption depends upon the magnitude ϵ_{mw} .
- We establish from the simulation that the interplay among the solvent condition, ϵ_{mw} and ϕ_c are all relevant to understanding the conformational landscape of the polymer.

Adding crowder particles to the system adds one more layer of complexity and takes the system one more step closer to a realistic system. In future, more detailed studies taking into accounts of more system-specific details should be fruitful as confinement, wall-interaction and crowders are very general in biological systems.

In the third problem, we employ molecular dynamics simulation to study the diffusivity of a tracer particle in an infinitely long cylindrical tube with its internal surface grafted with polymers under different solvent conditions, crowder densities and monomer-wall interactions. we found that

- For poor solvent condition, the radius of gyration of the graft polymers does not change significantly with the crowder density except for the highest density case. In case of a good solvent condition, the radius of gyration decreases with an increase in number of crowder particles.
- The diffusion of tracer particle slows down as tube becomes more crowded. This slow down happens regardless of solvent condition and wall interaction.
- The crowder particles are uniformly distributed in the middle of the tube, while near the tube's wall they form layered structure for both solvent conditions and different monomer-wall interactions. On the other hand, the monomers stick to the wall in layered fashion in poor solvent condition, however, the degree of adsorption and the number of layers depend upon the monomer-wall interaction. For good solvent condition, the polymers tend to assume extended structure for repulsive wall. For high attractive interaction, polymers gets adsorbed to the cylindrical wall and form a layered structure even for the good solvent condition.

In second part of the chapter 4, we presented preliminary results from the molecular dynamics simulations. We studied diffusion of the tracer particle and concluded that as the crowder density increases, particle shifts the behaviour from super-diffusive

behaviour to normal Brownian motion. The density of polymer grafts affects the shape and other properties of the cylindrical tube which also needs further probing. Also, we have chosen the tracer particle of fixed size, while we might find interesting results if we can use an extended object such as a polymer as a tracer. This is important as there are many biological scenarios where a polymer diffuses through a porous medium.

Appendix

A.1 Exact solution of the anisotropic case for a harmonic epigenetic potential in the absence of noise

Our governing equations represent a three-dimensional, coupled and, in general, non-linear dynamical system. The choice of a harmonic epigenetic potential $\delta\Psi^2/2$ and a constant force f yields a linear system of equations that can be written as,

$$\begin{aligned}\delta\dot{\Psi} &= -A\delta\Psi + B\left(\frac{1}{2}\delta R_{\parallel} + \delta R_{\perp}\right), \\ \delta\dot{R}_{\parallel} &= -C\delta R_{\parallel} - D\delta\Psi - f, \\ \delta\dot{R}_{\perp} &= -C\delta R_{\perp} - D\delta\Psi.\end{aligned}\tag{A.1}$$

We define the Laplace transform and its inverse as,

$$\begin{aligned}X(s) &= \int_0^{\infty} x(t)e^{-st} dt, \\ x(t) &= \frac{1}{2\pi i} \lim_{T \rightarrow \infty} \int_{\gamma-iT}^{\gamma+iT} X(s)e^{st} ds,\end{aligned}\tag{A.2}$$

where the integration is done along the vertical line $Re(s) = \gamma$ in complex plane so

that γ is greater than the real part of all singularities of $X(s)$.

Using the definition in Eq A.2, we take the Laplace transform of Eqs A.1,

$$\begin{aligned}
s\delta\Psi(s) - \delta\Psi(0) &= -A\delta\Psi(s) + \frac{B}{2}\delta R_{\parallel}(s) + B\delta R_{\perp}(s), \\
s\delta R_{\parallel}(s) - \delta R_{\parallel}(0) &= -C\delta R_{\parallel}(s) - D\delta\Psi(s) - \frac{f}{s}, \\
s\delta R_{\perp}(s) - \delta R_{\perp}(0) &= -C\delta R_{\perp}(s) - D\delta\Psi(s).
\end{aligned} \tag{A.3}$$

For the simplest initial condition, with $\delta\Psi(0) = \delta R_{\parallel}(0) = \delta R_{\perp}(0) = 0$, taking the inverse Laplace transform yields the solution.

$$\begin{aligned}
\delta\Psi(t) &= -\frac{Bf}{2}(a + be^{c_{11}t} + ce^{c_{22}t}), \\
\delta R_{\parallel}(t) &= \frac{BDf}{2}(a_1 - b_1e^{-Ct} + c_1e^{c_{11}t} + d_1e^{c_{22}t}) - f, \\
\delta R_{\perp}(t) &= \frac{BDf}{2}(a_1 - b_1e^{-Ct} + c_1e^{c_{11}t} + d_1e^{c_{22}t}),
\end{aligned}$$

where the constants are given by the following,

$$\begin{aligned}
a &= \frac{1}{c_{11}c_{22}}, \\
b &= \frac{1}{c_{11}(c_{11} - c_{22})}, \\
c &= \frac{1}{c_{22}(c_{22} - c_{11})}, \\
a_1 &= \frac{a}{C}, \\
b_1 &= \frac{1}{C(C + c_{11})(C + c_{22})}, \\
c_1 &= \frac{b}{(C + c_{11})}, \\
d_1 &= \frac{c}{(C + c_{22})},
\end{aligned}$$

and

$$c_{11,22} = \frac{-(A + C) \pm \sqrt{(C - A)^2 - 6BD}}{2}.$$

At long times, these solutions attain steady state values that vary linearly with the applied force f .

A.2 Correlation functions for the case of a harmonic chromatin compaction potential

For the system of equations which incorporates noise in the chromatin compaction variable, we can compute correlation functions analytically. We define Fourier and inverse Fourier transforms as,

$$\begin{aligned} X(\omega) &= \int_{-\infty}^{\infty} x(t)e^{i\omega t} dt, \\ x(t) &= \frac{1}{2\pi} \int_{-\infty}^{\infty} X(s)e^{-i\omega t} ds. \end{aligned} \quad (\text{A.4})$$

Taking the Fourier transform of the system and rearranging gives,

$$\begin{aligned} (i\omega + A)\delta\Psi(\omega) &= \frac{B}{2}\delta R_{\parallel}(\omega) + B\delta R_{\perp}(\omega) + \alpha\eta(\omega), \\ (i\omega + C)\delta R_{\parallel}(\omega) &= -D\delta\Psi(\omega) - f\delta(\omega), \\ (i\omega + C)\delta R_{\perp}(\omega) &= -D\delta\Psi(\omega). \end{aligned} \quad (\text{A.5})$$

Solving this system of Eqs. A.5 simultaneously for $\delta\Psi(\omega)$ yields the expression,

$$\delta\Psi(\omega) = \frac{-Bf\delta(\omega) + 2\alpha(i\omega + C)\eta(\omega)}{[2(i\omega + C)(i\omega + A) + 3BD]}, \quad (\text{A.6})$$

Using the expression for $\delta\Psi(\omega)$ and the assumption that the noise is Gaussian and

delta correlated yields

$$\begin{aligned}\langle \eta(\omega) \rangle &= 0, \\ \langle \eta(\omega) \eta(\omega') \rangle &= 2\pi \delta(\omega + \omega').\end{aligned}\tag{A.7}$$

We thus obtain

$$\langle \delta\Psi(\omega) \delta\Psi(\omega') \rangle = \frac{B^2 f^2 \delta(\omega) \delta(\omega') + 8\pi \alpha^2 (i\omega + C)(i\omega' + C) \delta(\omega + \omega')}{[2(i\omega + C)(i\omega + A) + 3BD][2(i\omega' + C)(i\omega' + A) + 3BD]}.\tag{A.8}$$

The inverse Fourier transform of the expression Equation A.8 yields the correlation function $\langle \delta\Psi(t) \delta\Psi(t') \rangle$,

$$\langle \delta\Psi(t) \delta\Psi(t') \rangle = \frac{1}{(2\pi)^2} \int \int d\omega d\omega' \langle \delta\Psi(\omega) \delta\Psi(\omega') \rangle e^{-i\omega t - i\omega' t'},\tag{A.9}$$

and

$$\begin{aligned}\langle \delta\Psi(t) \delta\Psi(t') \rangle &= \frac{B^2 f^2}{4\pi^2 (2AC + 3BD)^2} + \frac{-\alpha^2}{2\omega_0 \omega_1 (\omega_0^2 - \omega_1^2)} [(\omega_0 + \omega_1)(z_3^2 + C^2) \\ &\quad e^{-(\omega_0 - \omega_1)\Delta t} - (\omega_0 - \omega_1)(z_4^2 + C^2) e^{-(\omega_0 + \omega_1)\Delta t}].\end{aligned}$$

Now, we ignore the constant part and keep the part coming from the fluctuation,

$$\begin{aligned}\langle \delta\Psi(t) \delta\Psi(t') \rangle &= \frac{-\alpha^2}{2\omega_0 \omega_1 (\omega_0^2 - \omega_1^2)} [(\omega_0 + \omega_1)(z_3^2 + C^2) e^{-(\omega_0 - \omega_1)\Delta t} \\ &\quad - (\omega_0 - \omega_1)(z_4^2 + C^2) e^{-(\omega_0 + \omega_1)\Delta t}].\end{aligned}$$

where $\Delta t = t - t'$, $z_{1,2} = i(\omega_0 \pm \omega_1)$, $z_{3,4} = i(-\omega_0 \pm \omega_1)$, ω_0 and ω_1 is given by,

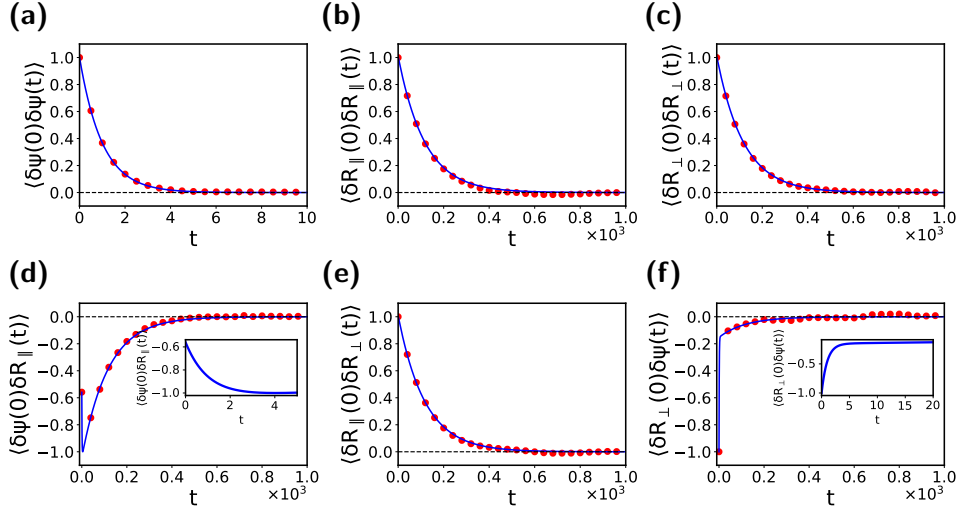


Figure A.1: Computations of autocorrelations and cross-correlations, in the auxetic regime, with $C = 0.01$, $D = 0.02$ and $B = -0.17$. **(a)** the autocorrelation function for $\delta\Psi$, $\langle\delta\Psi(0)\delta\Psi(t)\rangle$, **(b)** the autocorrelation function for δR_{\parallel} , $\langle\delta R_{\parallel}(0)\delta R_{\parallel}(t)\rangle$, **(c)** the autocorrelation function for δR_{\perp} , $\langle\delta R_{\perp}(0)\delta R_{\perp}(t)\rangle$, **(d)** the cross-correlation function for $\delta\Psi$ and δR_{\parallel} , $\langle\delta\Psi(0)\delta R_{\parallel}(t)\rangle$, **(e)** the cross-correlation function for δR_{\parallel} and δR_{\perp} , $\langle\delta R_{\parallel}(0)\delta R_{\perp}(t)\rangle$ and **(f)** the cross-correlation function for δR_{\perp} and $\delta\Psi$, $\langle\delta R_{\perp}(0)\delta\Psi(t)\rangle$. The insets show the behaviour close to the origin in two special cases where there is a competition between the two time-scales for relaxation. Points represent the numerical solution of the Langevin equations while lines represent the analytic formulae.

$$\omega_0 = \frac{A + C}{2},$$

$$\omega_1 = \frac{\sqrt{(A - C)^2 - 6BD}}{2}.$$

The other correlation functions are calculated in a similar way. The expressions are as follows,

$$\langle\delta R_{\parallel}(0)\delta R_{\parallel}(t)\rangle = \frac{\alpha^2 D^2}{2\omega_0\omega_1} \left[\frac{e^{-(\omega_0-\omega_1)\Delta t}}{(\omega_0-\omega_1)} - \frac{e^{-(\omega_0+\omega_1)\Delta t}}{(\omega_0+\omega_1)} \right], \quad (\text{A.10})$$

$$\langle\delta R_{\perp}(0)\delta R_{\perp}(t)\rangle = \frac{\alpha^2 D^2}{2\omega_0\omega_1} \left[\frac{e^{-(\omega_0-\omega_1)\Delta t}}{(\omega_0-\omega_1)} - \frac{e^{-(\omega_0+\omega_1)\Delta t}}{(\omega_0+\omega_1)} \right], \quad (\text{A.11})$$

$$\langle \delta R_{\parallel}(0) \delta R_{\perp}(t) \rangle = \frac{\alpha^2 D^2}{2\omega_0 \omega_1} \left[\frac{e^{-(\omega_0 - \omega_1)\Delta t}}{(\omega_0 - \omega_1)} - \frac{e^{-(\omega_0 + \omega_1)\Delta t}}{(\omega_0 + \omega_1)} \right], \quad (\text{A.12})$$

$$\langle \delta R_{\parallel}(0) \delta \Psi(t) \rangle = \frac{\alpha^2 D}{2\omega_0 \omega_1} \left[\frac{C - (\omega_0 - \omega_1)}{\omega_0 - \omega_1} e^{-(\omega_0 - \omega_1)\Delta t} - \frac{C - (\omega_0 + \omega_1)}{\omega_0 + \omega_1} e^{-(\omega_0 + \omega_1)\Delta t} \right], \quad (\text{A.13})$$

$$\langle \delta R_{\perp}(0) \delta \Psi(t) \rangle = \frac{\alpha^2 D}{2\omega_0 \omega_1} \left[\frac{C - (\omega_0 - \omega_1)}{\omega_0 - \omega_1} e^{-(\omega_0 - \omega_1)\Delta t} - \frac{C - (\omega_0 + \omega_1)}{\omega_0 + \omega_1} e^{-(\omega_0 + \omega_1)\Delta t} \right]. \quad (\text{A.14})$$

We display a number of autocorrelation and cross-correlation functions for the 3-dimensional auxetic system in Figure A.1.

A.3 Long time behaviour of cross-correlation functions

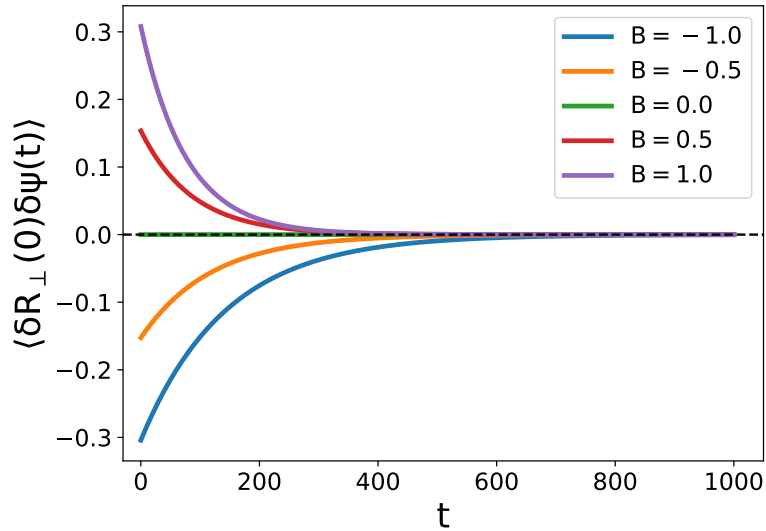


Figure A.2: The figure shows the long time cross-correlation function $\langle \delta R_{\perp}(0) \delta \Psi(t) \rangle_{t \gg 0}$ with the various values of B from $B = -1.0$ to $B = 1.0$ including the $B = 0$ case. We see that the slope of the correlation function changes as the sign of the parameter B changes from negative to positive.

The expression for the cross-correlation function $\langle \delta R_{\perp}(0)\delta\Psi(t) \rangle$ is,

$$\langle \delta R_{\perp}(0)\delta\Psi(t) \rangle = \frac{\alpha^2 D}{2\omega_0\omega_1} \left[\frac{C - (\omega_0 - \omega_1)}{\omega_0 - \omega_1} e^{-(\omega_0 - \omega_1)t} - \frac{C - (\omega_0 + \omega_1)}{\omega_0 + \omega_1} e^{-(\omega_0 + \omega_1)t} \right]. \quad (\text{A.15})$$

From Equation A.15, it is evident that there are two time scales $1/(\omega_0 - \omega_1)$ and $1/(\omega_0 + \omega_1)$. Since $1/(\omega_0 - \omega_1) > 1/(\omega_0 + \omega_1)$, for the long term behaviour, we keep the $e^{-(\omega_0 - \omega_1)t}$ term and discard the $e^{-(\omega_0 + \omega_1)t}$ term. The resulting correlation function, in the long time limit, can be written as,

$$\langle \delta R_{\perp}(0)\delta\Psi(t) \rangle_{t \gg 0} \approx \frac{\alpha^2 D}{2\omega_0\omega_1} \left(\frac{C - (\omega_0 - \omega_1)}{\omega_0 - \omega_1} \right) e^{-(\omega_0 - \omega_1)t}. \quad (\text{A.16})$$

We normalize by,

$$\delta R_{\perp}(0)\delta\Psi(t)_{t=0} = \frac{\alpha^2 D}{2\omega_0\omega_1} \left[\frac{C - (\omega_0 - \omega_1)}{\omega_0 - \omega_1} - \frac{C - (\omega_0 + \omega_1)}{\omega_0 + \omega_1} \right], \quad (\text{A.17})$$

which yields,

$$\langle \delta R_{\perp}(0)\delta\Psi(t) \rangle_{t \gg 0} \approx \frac{\left(\frac{C - (\omega_0 - \omega_1)}{\omega_0 - \omega_1} \right)}{\left(\frac{C - (\omega_0 - \omega_1)}{\omega_0 - \omega_1} - \frac{C - (\omega_0 + \omega_1)}{\omega_0 + \omega_1} \right)} e^{-(\omega_0 - \omega_1)t}. \quad (\text{A.18})$$

Equation A.18 for a choice of values of B is plotted in Figure A.2. The slope of the cross-correlation function $\langle \delta R_{\perp}(0)\delta\Psi(t) \rangle$ changes sign as the parameter B changes sign indicating the boundary of auxetic and non-auxetic regime. Similarly the slope of the cross-correlation $\langle \delta R_{\parallel}(0)\delta\Psi(t) \rangle$ changes sign at the auxetic-nonauxetic boundary, while there is no such change in the slope of cross-correlation functions $\langle \delta\Psi(0)R_{\parallel}(t) \rangle$ and $\langle \delta\Psi(0)R_{\perp}(t) \rangle$ (see Figure A.3).

The correlation functions $\langle \delta R_{\perp}(0)\delta\Psi(t) \rangle$ and $\langle \delta\Psi(0)\delta R_{\perp}(t) \rangle$ are same as $\langle \delta R_{\parallel}(0)\delta\Psi(t) \rangle$ and $\langle \delta\Psi(0)\delta R_{\parallel}(t) \rangle$. Exchanging R_{\parallel} with R_{\perp} has no effect on correlation functions.

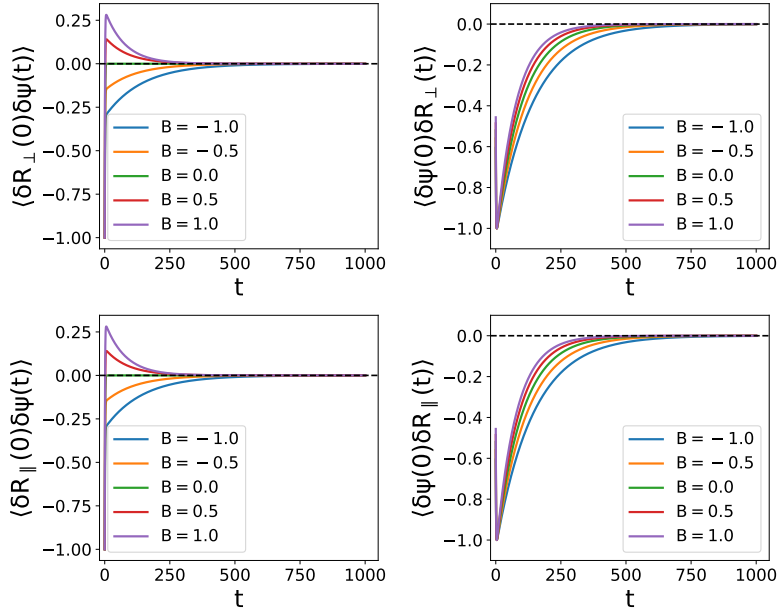


Figure A.3: The correlation functions: **(a)** the cross-correlation function for δR_{\perp} and $\delta \Psi$, $\langle \delta R_{\perp}(0) \delta \Psi(t) \rangle$ **(b)** the cross-correlation function for $\delta \Psi$ and δR_{\perp} , $\langle \delta \Psi(0) \delta R_{\perp}(t) \rangle$ **(c)** the cross-correlation function for δR_{\parallel} and $\delta \Psi$, $\langle \delta R_{\parallel}(0) \delta \Psi(t) \rangle$ **(d)** the cross-correlation function for $\delta \Psi$ and δR_{\parallel} , $\langle \delta \Psi(0) \delta R_{\parallel}(t) \rangle$ with different values of parameter B . We see that the correlation functions $\langle \delta R_{\perp}(0) \delta \Psi(t) \rangle$ and $\langle \delta R_{\parallel}(0) \delta \Psi(t) \rangle$ change the slope with the parameter B while there is no such effect on $\langle \delta \Psi(0) \delta R_{\perp}(t) \rangle$ and $\langle \delta \Psi(0) \delta R_{\parallel}(t) \rangle$.

A.4 Periodic Force

The 3-dimensional system with a harmonic potential and a periodic force can be written as,

$$\begin{aligned}
 \delta \dot{\Psi} &= -A \delta \Psi + B \left(\frac{1}{2} \delta R_{\parallel} + \delta R_{\perp} \right) + \eta_{\Psi}, \\
 \delta \dot{R}_{\parallel} &= -C \delta R_{\parallel} - D \delta \Psi - f \sin \omega t, \\
 \delta \dot{R}_{\perp} &= -C \delta R_{\perp} - D \delta \Psi.
 \end{aligned} \tag{A.19}$$

Following the procedure of section A.1,

$$\delta \Psi(t) = \frac{B f \omega}{2} \left(A_1 e^{c_{11} t} + B_1 e^{c_{22} t} + C_1 \cos(\omega t) + \frac{D_1}{\omega} \sin(\omega t) \right), \tag{A.20}$$

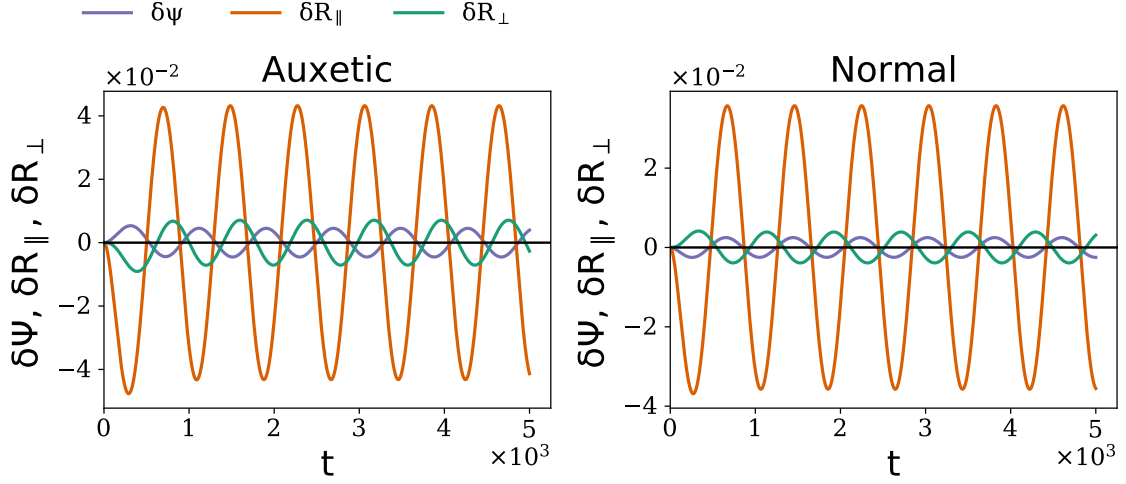


Figure A.4: The behaviour of the systems under periodic force: The figure (a) shows that how an auxetic system (b) a normal system behaves under a periodic force. It can be seen that in auxetic case, both radii δR_{\parallel} and δR_{\perp} simultaneously increase or decrease while in normal case, if one increases, the other decreases and vice-versa.

$$\delta R_{\parallel}(t) = -\frac{BDf\omega}{2} \left[A_2 e^{-Ct} + B_2 e^{c_{11}t} + C_2 e^{c_{22}t} + D_2 \cos(\omega t) + \frac{E_2}{\omega} \sin(\omega t) \right] - f\omega \left[K e^{-Ct} + L \cos(\omega t) + \frac{M}{\omega} \sin(\omega t) \right], \quad (\text{A.21})$$

$$\delta R_{\perp}(t) = -\frac{BDf\omega}{2} \left[A_2 e^{-Ct} + B_2 e^{c_{11}t} + C_2 e^{c_{22}t} + D_2 \cos(\omega t) + \frac{E_2}{\omega} \sin(\omega t) \right]. \quad (\text{A.22})$$

In order to get the steady state part of the solution, we discard the exponential terms which leads to the following expressions,

$$\begin{aligned} \delta \Psi(t) &= \frac{Bf\omega}{2} \left(C_1 \cos(\omega t) + \frac{D_1}{\omega} \sin(\omega t) \right), \\ \delta R_{\parallel}(t) &= - \left[\frac{BDD_2}{2} + L \right] f\omega \cos(\omega t) - \left[\frac{BDE_2}{2} + M \right] f \sin(\omega t), \\ \delta R_{\perp}(t) &= -\frac{BDf\omega}{2} \left[D_2 \cos(\omega t) + \frac{E_2}{\omega} \sin(\omega t) \right], \end{aligned} \quad (\text{A.23})$$

where the constants $A_1, B_1, C_1, D_1, A_2, B_2, C_2, D_2, E_2, K, L$ and M are given by

the following,

$$\begin{aligned}
A_1 &= \frac{1}{(c_{11} - c_{22})(c_{11}^2 + \omega^2)}, \\
B_1 &= -\frac{1}{(c_{11} - c_{22})(c_{22}^2 + \omega^2)}, \\
C_1 &= \frac{c_{11} - c_{22}}{(c_{11}^2 + \omega^2)(c_{22}^2 + \omega^2)}, \\
D_1 &= \frac{c_{11}c_{22} - \omega^2}{(c_{11}^2 + \omega^2)(c_{22}^2 + \omega^2)}, \\
A_2 &= \frac{1}{(C + c_{11})(C + c_{22})(C^2 + \omega^2)}, \\
B_2 &= \frac{1}{(C + c_{11})(c_{11} - c_{22})(c_{11}^2 + \omega^2)}, \\
C_2 &= \frac{1}{(C + c_{22})(c_{22} - c_{11})(c_{22}^2 + \omega^2)}, \\
D_2 &= \frac{Cc_{11} + Cc_{22} - c_{11}c_{22} + \omega^2}{(C^2 + \omega^2)(c_{11}^2 + \omega^2)(c_{22}^2 + \omega^2)}, \\
E_2 &= \frac{Cc_{11}c_{22} + C\omega^2 + c_{11}\omega^2 + c_{22}\omega^2}{(C^2 + \omega^2)(c_{11}^2 + \omega^2)(c_{22}^2 + \omega^2)}, \\
K &= \frac{1}{C^2 + \omega^2}, \\
L &= -\frac{1}{C^2 + \omega^2}, \\
M &= -\frac{C}{C^2 + \omega^2},
\end{aligned}$$

with $c_{11,22} = \frac{-(A+C) \pm \sqrt{(C-A)^2 + 6BD}}{2}$.

The variables $\delta\Psi(t)$, $\delta R_{\parallel}(t)$ and $\delta R_{\perp}(t)$ for auxetic and normal systems in steady state are plotted with time t in Figure A.4.

Bibliography

- [Adiga and Brenner, 2005] Adiga, S. P. and Brenner, D. W. (2005). Flow control through polymer-grafted smart nanofluidic channels: molecular dynamics simulations. *Nano letters*, 5(12):2509–2514.
- [Agrawal et al., 2017] Agrawal, A., Ganai, N., Sengupta, S., and Menon, G. I. (2017). Chromatin as active matter. *Journal of Statistical Mechanics: Theory and Experiment*, 2017(1):014001.
- [Agrawal et al., 2018] Agrawal, A., Ganai, N., Sengupta, S., and Menon, G. I. (2018). A first-principles approach to large-scale nuclear architecture. *bioRxiv*.
- [Alberts et al., 2013] Alberts, B., Bray, D., Hopkin, K., Johnson, A., Lewis, J., Raff, M., Roberts, K., and Walter, P. (2013). *Essential cell biology*. Garland Science.
- [Alder and Wainwright, 1957] Alder, B. J. and Wainwright, T. E. (1957). Phase transition for a hard sphere system. *The Journal of chemical physics*, 27(5):1208–1209.
- [Alder and Wainwright, 1959] Alder, B. J. and Wainwright, T. E. (1959). Studies in molecular dynamics. i. general method. *The Journal of Chemical Physics*, 31(2):459–466.
- [Alderson et al., 2005] Alderson, A., Alderson, K. L., Davies, P. J., and Smart, G. M. (2005). The effects of processing on the topology and mechanical properties of negative poisson’s ratio foams. In *ASME 2005 International Mechanical*

- Engineering Congress and Exposition*, pages 503–510. American Society of Mechanical Engineers.
- [Andersen, 1980] Andersen, H. C. (1980). Molecular dynamics simulations at constant pressure and/or temperature. *The Journal of chemical physics*, 72(4):2384–2393.
- [Arkin and Janke, 2012a] Arkin, H. and Janke, W. (2012a). Ground-state properties of a polymer chain in an attractive sphere. *The Journal of Physical Chemistry B*, 116(34):10379–10386.
- [Arkin and Janke, 2012b] Arkin, H. and Janke, W. (2012b). Structural behavior of a polymer chain inside an attractive sphere. *Physical Review E*, 85(5):051802.
- [Asakura and Oosawa, 1954] Asakura, S. and Oosawa, F. (1954). On interaction between two bodies immersed in a solution of macromolecules. *The Journal of Chemical Physics*, 22(7):1255–1256.
- [Bachmann and Janke, 2005] Bachmann, M. and Janke, W. (2005). Conformational transitions of nongrafted polymers near an absorbing substrate. *Physical review letters*, 95(5):058102.
- [Balducci et al., 2006] Balducci, A., Mao, P., Han, J., and Doyle, P. S. (2006). Double-stranded dna diffusion in slitlike nanochannels. *Macromolecules*, 39(18):6273–6281.
- [Berendsen et al., 1984] Berendsen, H. J., Postma, J. v., van Gunsteren, W. F., DiNola, A., and Haak, J. R. (1984). Molecular dynamics with coupling to an external bath. *The Journal of chemical physics*, 81(8):3684–3690.
- [Berger, 2007] Berger, S. L. (2007). The complex language of chromatin regulation during transcription. *Nature*, 447(7143):407.

- [Boal and Boal, 2012] Boal, D. and Boal, D. H. (2012). *Mechanics of the Cell*. Cambridge University Press.
- [Bokvist and Gröbner, 2007] Bokvist, M. and Gröbner, G. (2007). Misfolding of amyloidogenic proteins at membrane surfaces: the impact of macromolecular crowding. *Journal of the American Chemical Society*, 129(48):14848–14849.
- [Bošković et al., 2014] Bošković, A., Eid, A., Pontabry, J., Ishiuchi, T., Spiegelhalter, C., Ram, E. V. R., Meshorer, E., and Torres-Padilla, M.-E. (2014). Higher chromatin mobility supports totipotency and precedes pluripotency in vivo. *Genes & development*, 28(10):1042–1047.
- [Boyle et al., 2001] Boyle, S., Gilchrist, S., Bridger, J. M., Mahy, N. L., Ellis, J. A., and Bickmore, W. A. (2001). The spatial organization of human chromosomes within the nuclei of normal and emerin-mutant cells. *Human molecular genetics*, 10(3):211–220.
- [Brittain and Minko, 2007] Brittain, W. J. and Minko, S. (2007). A structural definition of polymer brushes. *Journal of Polymer Science Part A: Polymer Chemistry*, 45(16):3505–3512.
- [Butler and Crothers, 1983] Butler, P. and Crothers, D. M. (1983). The folding of chromatin. *Critical Reviews in Biochemistry*, 15(1):57–91.
- [Cacciuto and Luijten, 2006] Cacciuto, A. and Luijten, E. (2006). Self-avoiding flexible polymers under spherical confinement. *Nano Letters*, 6(5):901–905.
- [Caille et al., 2002] Caille, N., Thoumine, O., Tardy, Y., and Meister, J.-J. (2002). Contribution of the nucleus to the mechanical properties of endothelial cells. *Journal of biomechanics*, 35(2):177–187.

- [Calvo et al., 2002] Calvo, F., Galindez, J., and Gadéa, F. (2002). Sampling the configuration space of finite atomic systems: How ergodic is molecular dynamics? *The Journal of Physical Chemistry A*, 106(16):4145–4152.
- [Chaikin et al., 1995] Chaikin, P. M., Lubensky, T. C., and Witten, T. A. (1995). *Principles of condensed matter physics*, volume 1. Cambridge university press Cambridge.
- [Chalut et al., 2012] Chalut, K. J., Höpfler, M., Lautenschläger, F., Boyde, L., Chan, C. J., Ekpenyong, A., Martinez-Arias, A., and Guck, J. (2012). Chromatin decondensation and nuclear softening accompany nanog downregulation in embryonic stem cells. *Biophysical journal*, 103(10):2060–2070.
- [Chen and Dent, 2014] Chen, T. and Dent, S. Y. (2014). Chromatin modifiers and remodellers: regulators of cellular differentiation. *Nature Reviews Genetics*, 15(2):93.
- [Chen et al., 2004] Chen, Y.-L., Graham, M., De Pablo, J., Randall, G., Gupta, M., and Doyle, P. (2004). Conformation and dynamics of single dna molecules in parallel-plate slit microchannels. *Physical Review E*, 70(6):060901.
- [Cheung et al., 2005] Cheung, M. S., Klimov, D., and Thirumalai, D. (2005). Molecular crowding enhances native state stability and refolding rates of globular proteins. *Proceedings of the National Academy of Sciences*, 102(13):4753–4758.
- [Choi et al., 2014] Choi, J., Hore, M. J., Clarke, N., Winey, K. I., and Composto, R. J. (2014). Nanoparticle brush architecture controls polymer diffusion in nanocomposites. *Macromolecules*, 47(7):2404–2410.
- [Chowdhury et al., 2010] Chowdhury, F., Na, S., Li, D., Poh, Y.-C., Tanaka, T. S., Wang, F., and Wang, N. (2010). Material properties of the cell dictate stress-induced spreading and differentiation in embryonic stem cells. *Nature materials*, 9(1):82–88.

- [Conrad and Robertson, 2019] Conrad, J. C. and Robertson, M. L. (2019). Towards mimicking biological function with responsive surface-grafted polymer brushes. *Current Opinion in Solid State and Materials Science*, 23(1):1–12.
- [Dado et al., 2012] Dado, D., Sagi, M., Levenberg, S., and Zemel, A. (2012). Mechanical control of stem cell differentiation. *Regenerative medicine*, 7(1):101–116.
- [Dahl et al., 2005] Dahl, K. N., Engler, A. J., Pajerowski, J. D., and Discher, D. E. (2005). Power-law rheology of isolated nuclei with deformation mapping of nuclear substructures. *Biophysical journal*, 89(4):2855–2864.
- [Das and Chakraborty, 2010] Das, S. and Chakraborty, S. (2010). Effect of confinement on the collapsing mechanism of a flexible polymer chain. *The Journal of chemical physics*, 133(17):174904.
- [Davis, 1995] Davis, L. I. (1995). The nuclear pore complex. *Annual review of biochemistry*, 64(1):865–896.
- [de Gennes, 1979] de Gennes, P. (1979). *Scaling concepts in polymer physics*. Cornell university press.
- [de Groot et al., 2013] de Groot, G. W., Santonicola, M. G., Sugihara, K., Zambelli, T., Reimhult, E., Vörös, J., and Vancso, G. J. (2013). Switching transport through nanopores with ph-responsive polymer brushes for controlled ion permeability. *ACS applied materials & interfaces*, 5(4):1400–1407.
- [De Nooijer et al., 2009] De Nooijer, S., Wellink, J., Mulder, B., and Bisseling, T. (2009). Non-specific interactions are sufficient to explain the position of heterochromatic chromocenters and nucleoli in interphase nuclei. *Nucleic acids research*, 37(11):3558–3568.

- [Dimitrov et al., 2006] Dimitrov, D. I., Milchev, A., Binder, K., and Heermann, D. W. (2006). Structure of polymer brushes in cylindrical tubes: A molecular dynamics simulation. *Macromolecular theory and simulations*, 15(7):573–583.
- [Doi, 1996] Doi, M. (1996). *Introduction to Polymer Physics*. Oxford university press.
- [Doi and Edwards, 1988] Doi, M. and Edwards, S. F. (1988). *The theory of polymer dynamics*, volume 73. oxford university press.
- [Douville et al., 2008] Douville, N., Huh, D., and Takayama, S. (2008). Dna linearization through confinement in nanofluidic channels. *Analytical and bioanalytical chemistry*, 391(7):2395–2409.
- [Efroni et al., 2008] Efroni, S., Duttagupta, R., Cheng, J., Dehghani, H., Hoepfner, D. J., Dash, C., Bazett-Jones, D. P., Le Grice, S., McKay, R. D., Buetow, K. H., et al. (2008). Global transcription in pluripotent embryonic stem cells. *Cell stem cell*, 2(5):437–447.
- [Ellis, 2001] Ellis, R. J. (2001). Macromolecular crowding: an important but neglected aspect of the intracellular environment. *Current opinion in structural biology*, 11(1):114–119.
- [Engler et al., 2006] Engler, A. J., Sen, S., Sweeney, H. L., and Discher, D. E. (2006). Matrix elasticity directs stem cell lineage specification. *Cell*, 126(4):677–689.
- [Evans and Alderson, 2000] Evans, K. E. and Alderson, A. (2000). Auxetic materials: functional materials and structures from lateral thinking! *Advanced materials*, 12(9):617–628.
- [Evans et al., 2009] Evans, N. D., Minelli, C., Gentleman, E., LaPointe, V., Patankar, S. N., Kallivretaki, M., Chen, X., Roberts, C. J., and Stevens, M. M.

- (2009). Substrate stiffness affects early differentiation events in embryonic stem cells. *Eur cell mater*, 18(1):e13.
- [Ewald, 1921] Ewald, P. P. (1921). Die berechnung optischer und elektrostatischer gitterpotentiale. *Annalen der Physik*, 369(3):253–287.
- [Feig et al., 2017] Feig, M., Yu, I., Wang, P.-h., Nawrocki, G., and Sugita, Y. (2017). Crowding in cellular environments at an atomistic level from computer simulations. *The Journal of Physical Chemistry B*, 121(34):8009–8025.
- [Filippidi et al., 2007] Filippidi, E., Michailidou, V., Loppinet, B., R uhe, J., and Fytas, G. (2007). Brownian diffusion close to a polymer brush. *Langmuir*, 23(9):5139–5142.
- [Finch et al., 1981] Finch, J., Brown, R., Rhodes, D., Richmond, T., Rushton, B., Lutter, L., and Klug, A. (1981). X-ray diffraction study of a new crystal form of the nucleosome core showing higher resolution. *Journal of molecular biology*, 145(4):757–769.
- [Finch et al., 1977] Finch, J., Lutter, L., Rhodes, D., Brown, R., Rushton, B., Levitt, M., and Klug, A. (1977). Structure of nucleosome core particles of chromatin. *Nature*, 269(5623):29.
- [Flory, 1965] Flory, P. d. (1965). Statistical thermodynamics of liquid mixtures. *Journal of the American Chemical Society*, 87(9):1833–1838.
- [Flory, 1970] Flory, P. J. (1970). Fifteenth spiers memorial lecture. thermodynamics of polymer solutions. *Discussions of the Faraday Society*, 49:7–29.
- [Fošnarič et al., 2013] Fošnarič, M., Iglič, A., Kroll, D. M., and May, S. (2013). Monte carlo simulations of a polymer confined within a fluid vesicle. *Soft Matter*, 9(15):3976–3984.

- [Franke, 1970] Franke, W. W. (1970). On the universality of nuclear pore complex structure. *Cell and Tissue Research*, 105(3):405–429.
- [Frenkel and Smit, 2001] Frenkel, D. and Smit, B. (2001). *Understanding molecular simulation: from algorithms to applications*, volume 1. Elsevier.
- [Furusawa and Kaneko, 2012] Furusawa, C. and Kaneko, K. (2012). A dynamical-systems view of stem cell biology. *Science*, 338(6104):215–217.
- [Ganai et al., 2014] Ganai, N., Sengupta, S., and Menon, G. I. (2014). Chromosome positioning from activity-based segregation. *Nucleic acids research*, 42(7):4145–4159.
- [Gaspar-Maia et al., 2011] Gaspar-Maia, A., Alajem, A., Meshorer, E., and Ramalho-Santos, M. (2011). Open chromatin in pluripotency and reprogramming. *Nature reviews Molecular cell biology*, 12(1):36.
- [Ghosh et al., 2015] Ghosh, S. K., Cherstvy, A. G., and Metzler, R. (2015). Non-universal tracer diffusion in crowded media of non-inert obstacles. *Physical Chemistry Chemical Physics*, 17(3):1847–1858.
- [Gilbert, 2000] Gilbert, S. F. (2000). Diachronic biology meets evo-devo: Ch waddington’s approach to evolutionary developmental biology. *American Zoologist*, 40(5):729–737.
- [Golkaram et al., 2017] Golkaram, M., Jang, J., Hellander, S., Kosik, K. S., and Petzold, L. R. (2017). The role of chromatin density in cell population heterogeneity during stem cell differentiation. *Scientific Reports*, 7(1):13307.
- [Grima et al., 2006] Grima, J. N., Gatt, R., Ravirala, N., Alderson, A., and Evans, K. E. (2006). Negative poisson’s ratios in cellular foam materials. *Materials Science and Engineering: A*, 423(1-2):214–218.

- [Guilak et al., 2000] Guilak, F., Tedrow, J. R., and Burgkart, R. (2000). Viscoelastic properties of the cell nucleus. *Biochemical and biophysical research communications*, 269(3):781–786.
- [Ha and Jung, 2015] Ha, B.-Y. and Jung, Y. (2015). Polymers under confinement: single polymers, how they interact, and as model chromosomes. *Soft Matter*, 11(12):2333–2352.
- [Haraguchi et al., 2014] Haraguchi, K., Kubota, K., Takada, T., and Mahara, S. (2014). Highly protein-resistant coatings and suspension cell culture thereon from amphiphilic block copolymers prepared by raft polymerization. *Biomacromolecules*, 15(6):1992–2003.
- [Hawkins et al., 2010] Hawkins, R. D., Hon, G. C., Lee, L. K., Ngo, Q., Lister, R., Pelizzola, M., Edsall, L. E., Kuan, S., Luu, Y., Klugman, S., et al. (2010). Distinct epigenomic landscapes of pluripotent and lineage-committed human cells. *Cell stem cell*, 6(5):479–491.
- [Heo et al., 2018] Heo, S.-J., Cosgrove, B. D., Dai, E. N., and Mauck, R. L. (2018). Mechano-adaptation of the stem cell nucleus. *Nucleus*, 9(1):9–19.
- [Hill, 1986] Hill, T. L. (1986). *An introduction to statistical thermodynamics*. Courier Corporation.
- [Hoover, 1985] Hoover, W. G. (1985). Canonical dynamics: Equilibrium phase-space distributions. *Physical review A*, 31(3):1695.
- [Hospital et al., 2015] Hospital, A., Goñi, J. R., Orozco, M., and Gelpí, J. L. (2015). Molecular dynamics simulations: advances and applications. *Advances and applications in bioinformatics and chemistry: AABC*, 8:37.

- [Hsu and Grassberger, 2005] Hsu, H.-P. and Grassberger, P. (2005). The coil-globule transition of confined polymers. *Journal of Statistical Mechanics: Theory and Experiment*, 2005(01):P01007.
- [Huang and Chen, 2016] Huang, C. and Chen, L. (2016). Negative poisson's ratio in modern functional materials. *Advanced Materials*, 28(37):8079–8096.
- [Huang, 2012] Huang, S. (2012). The molecular and mathematical basis of waddington's epigenetic landscape: A framework for post-darwinian biology? *Bioessays*, 34(2):149–157.
- [Huggins, 1964] Huggins, M. L. (1964). A revised theory of high polymer solutions. *Journal of the American Chemical Society*, 86(17):3535–3540.
- [Humphrey et al., 1996] Humphrey, W., Dalke, A., and Schulten, K. (1996). VMD – Visual Molecular Dynamics. *Journal of Molecular Graphics*, 14:33–38.
- [Hwang et al., 2013] Hwang, N. S., Varghese, S., Lee, H. J., Zhang, Z., and Elisseeff, J. (2013). Biomaterials directed in vivo osteogenic differentiation of mesenchymal cells derived from human embryonic stem cells. *Tissue Engineering Part A*, 19(15-16):1723–1732.
- [Iborra, 2007] Iborra, F. J. (2007). Can visco-elastic phase separation, macromolecular crowding and colloidal physics explain nuclear organisation? *Theoretical Biology and Medical Modelling*, 4(1):15.
- [Ionov et al., 2009] Ionov, L., Synytska, A., Kaul, E., and Diez, S. (2009). Protein-resistant polymer coatings based on surface-adsorbed poly (aminoethyl methacrylate)/poly (ethylene glycol) copolymers. *Biomacromolecules*, 11(1):233–237.
- [Ionov et al., 2010] Ionov, L., Synytska, A., Kaul, E., and Diez, S. (2010). Protein-resistant polymer coatings based on surface-adsorbed poly (aminoethyl methacrylate)/poly (ethylene glycol) copolymers. *Biomacromolecules*, 11(1):233–237.

- [Jacobs, 1935] Jacobs, M. H. (1935). Diffusion processes. In *Diffusion Processes*, pages 1–145. Springer.
- [Jeon et al., 2016] Jeon, C., Jung, Y., and Ha, B.-Y. (2016). Effects of molecular crowding and confinement on the spatial organization of a biopolymer. *Soft matter*, 12(47):9436–9450.
- [Jo et al., 2007] Jo, K., Dhingra, D. M., Odijk, T., de Pablo, J. J., Graham, M. D., Runnheim, R., Forrest, D., and Schwartz, D. C. (2007). A single-molecule barcoding system using nanoslits for dna analysis. *Proceedings of the National Academy of Sciences*, 104(8):2673–2678.
- [Jun and Mulder, 2006] Jun, S. and Mulder, B. (2006). Entropy-driven spatial organization of highly confined polymers: lessons for the bacterial chromosome. *Proceedings of the National Academy of Sciences*, 103(33):12388–12393.
- [Jun and Wright, 2010] Jun, S. and Wright, A. (2010). Entropy as the driver of chromosome segregation. *Nature Reviews Microbiology*, 8(8):600.
- [Justin and Engler, 2011] Justin, R. T. and Engler, A. J. (2011). Stiffness gradients mimicking in vivo tissue variation regulate mesenchymal stem cell fate. *PloS one*, 6(1):e15978.
- [Kang et al., 2015a] Kang, H., Pincus, P. A., Hyeon, C., and Thirumalai, D. (2015a). Effects of macromolecular crowding on the collapse of biopolymers. *Physical review letters*, 114(6):068303.
- [Kang et al., 2015b] Kang, H., Yoon, Y.-G., Thirumalai, D., and Hyeon, C. (2015b). Confinement-induced glassy dynamics in a model for chromosome organization. *Physical review letters*, 115(19):198102.

- [Kauffman, 1992] Kauffman, S. A. (1992). The origins of order: Self-organization and selection in evolution. In *Spin glasses and biology*, pages 61–100. World Scientific.
- [Khokhlov et al., 2011] Khokhlov, A., de Gennes, P.-G., et al. (2011). *Giant molecules: here, there, and everywhere*. World Scientific.
- [Kim et al., 2015] Kim, J., Jeon, C., Jeong, H., Jung, Y., and Ha, B.-Y. (2015). A polymer in a crowded and confined space: effects of crowder size and polydispersity. *Soft Matter*, 11(10):1877–1888.
- [Kratky and Porod, 1949] Kratky, O. and Porod, G. (1949). Röntgenuntersuchung gelöster fadenmoleküle. *Recueil des Travaux Chimiques des Pays-Bas*, 68(12):1106–1122.
- [Krawczyk et al., 2005] Krawczyk, J., Owczarek, A., Prellberg, T., and Rechnitzer, A. (2005). Layering transitions for adsorbing polymers in poor solvents. *EPL (Europhysics Letters)*, 70(6):726.
- [Landau and Lifshitz, 1986] Landau, L. D. and Lifshitz, E. (1986). Theory of elasticity, vol. 7. *Course of Theoretical Physics*, 3:109.
- [Larson et al., 2017] Larson, A. G., Elnatan, D., Keenen, M. M., Trnka, M. J., Johnston, J. B., Burlingame, A. L., Agard, D. A., Redding, S., and Narlikar, G. J. (2017). Liquid droplet formation by hp1 α suggests a role for phase separation in heterochromatin. *Nature*, 547(7662):236.
- [Li et al., 2012] Li, M., Liu, G.-H., and Belmonte, J. C. I. (2012). Navigating the epigenetic landscape of pluripotent stem cells. *Nature Reviews Molecular Cell Biology*, 13(8):524.
- [Lieberman-Aiden et al., 2009] Lieberman-Aiden, E., Van Berkum, N. L., Williams, L., Imakaev, M., Ragooczy, T., Telling, A., Amit, I., Lajoie, B. R., Sabo, P. J.,

- Dorschner, M. O., et al. (2009). Comprehensive mapping of long-range interactions reveals folding principles of the human genome. *science*, 326(5950):289–293.
- [Lim and Denton, 2014] Lim, W. K. and Denton, A. R. (2014). Polymer crowding and shape distributions in polymer-nanoparticle mixtures. *The Journal of chemical physics*, 141(11):114909.
- [Luger et al., 1997] Luger, K., Mäder, A. W., Richmond, R. K., Sargent, D. F., and Richmond, T. J. (1997). Crystal structure of the nucleosome core particle at 2.8 Å resolution. *Nature*, 389(6648):251.
- [Mao et al., 2015] Mao, X., Gavara, N., and Song, G. (2015). Nuclear mechanics and stem cell differentiation. *Stem Cell Reviews and Reports*, 11(6):804–812.
- [Mao et al., 1995] Mao, Y., Cates, M., and Lekkerkerker, H. (1995). Depletion force in colloidal systems. *Physica A: Statistical Mechanics and its Applications*, 222(1-4):10–24.
- [Marenz et al., 2012] Marenz, M., Zierenberg, J., Arkin, H., and Janke, W. (2012). Simple flexible polymers in a spherical cage. *arXiv preprint arXiv:1212.6144*.
- [Martins et al., 2018] Martins, P., Plascak, J., and Bachmann, M. (2018). Adsorption of flexible polymer chains on a surface: Effects of different solvent conditions. *The Journal of chemical physics*, 148(20):204901.
- [Mastro et al., 1984] Mastro, A. M., Babich, M. A., Taylor, W. D., and Keith, A. D. (1984). Diffusion of a small molecule in the cytoplasm of mammalian cells. *Proceedings of the National Academy of Sciences*, 81(11):3414–3418.
- [McGhee and Felsenfeld, 1980] McGhee, J. D. and Felsenfeld, G. (1980). Nucleosome structure. *Annual review of biochemistry*, 49(1):1115–1156.
- [McNally, 2011] McNally, J. G. (2011). Foreword. biophysics in chromatin structure and nuclear dynamics. *Chromosome Research*, 19(1):1–3.

- [Meshorer and Misteli, 2006] Meshorer, E. and Misteli, T. (2006). Chromatin in pluripotent embryonic stem cells and differentiation. *Nature reviews Molecular cell biology*, 7(7):540.
- [Meshorer et al., 2006] Meshorer, E., Yellajoshula, D., George, E., Scambler, P. J., Brown, D. T., and Misteli, T. (2006). Hyperdynamic plasticity of chromatin proteins in pluripotent embryonic stem cells. *Developmental cell*, 10(1):105–116.
- [Minton, 2005] Minton, A. P. (2005). Models for excluded volume interaction between an unfolded protein and rigid macromolecular cosolutes: macromolecular crowding and protein stability revisited. *Biophysical journal*, 88(2):971–985.
- [Miroshnikova et al., 2017] Miroshnikova, Y. A., Nava, M. M., and Wickström, S. A. (2017). Emerging roles of mechanical forces in chromatin regulation. *J Cell Sci*, 2017:jcs–202192.
- [Misteli, 2007] Misteli, T. (2007). Beyond the sequence: cellular organization of genome function. *Cell*, 128(4):787–800.
- [Möddel et al., 2014] Möddel, M., Janke, W., and Bachmann, M. (2014). Adsorption and pattern recognition of polymers at complex surfaces with attractive stripelike motifs. *Physical review letters*, 112(14):148303.
- [Muthukumar, 1986] Muthukumar, M. (1986). Thermodynamics of polymer solutions. *The Journal of chemical physics*, 85(8):4722–4728.
- [Muthukumar, 2012a] Muthukumar, M. (2012a). Polymers under confinement. *Advances in Chemical Physics, Volume 149*, pages 129–196.
- [Muthukumar, 2012b] Muthukumar, M. (2012b). *Polymers under Confinement*, pages 129–196. Wiley-Blackwell.
- [Muthukumar, 2016] Muthukumar, M. (2016). *Polymer translocation*. CRC press.

- [Muthukumar and Edwards, 1982] Muthukumar, M. and Edwards, S. (1982). Extrapolation formulas for polymer solution properties. *The Journal of Chemical Physics*, 76(5):2720–2730.
- [Narlikar et al., 2002] Narlikar, G. J., Fan, H.-Y., and Kingston, R. E. (2002). Cooperation between complexes that regulate chromatin structure and transcription. *Cell*, 108(4):475–487.
- [Nelson, 2004] Nelson, P. (2004). *Biological physics*. WH Freeman New York.
- [Nosé, 1984] Nosé, S. (1984). A unified formulation of the constant temperature molecular dynamics methods. *The Journal of chemical physics*, 81(1):511–519.
- [Onuchic et al., 1997] Onuchic, J. N., Luthey-Schulten, Z., and Wolynes, P. G. (1997). Theory of protein folding: the energy landscape perspective. *Annual review of physical chemistry*, 48(1):545–600.
- [Onuchic and Wolynes, 2004] Onuchic, J. N. and Wolynes, P. G. (2004). Theory of protein folding. *Current opinion in structural biology*, 14(1):70–75.
- [Pagliara et al., 2014] Pagliara, S., Franze, K., McClain, C. R., Wylde, G. W., Fisher, C. L., Franklin, R. J. M., Kabla, A. J., Keyser, U. F., and Chalut, K. J. (2014). Auxetic nuclei in embryonic stem cells exiting pluripotency. *Nature Materials*, 13:638.
- [Pajerowski et al., 2007] Pajerowski, J. D., Dahl, K. N., Zhong, F. L., Sammak, P. J., and Discher, D. E. (2007). Physical plasticity of the nucleus in stem cell differentiation. *Proceedings of the National Academy of Sciences*, 104(40):15619–15624.
- [Palit et al., 2017] Palit, S., He, L., Hamilton, W. A., Yethiraj, A., and Yethiraj, A. (2017). The effect of crowder charge in a model polymer–colloid system for macro-

- molecular crowding: Polymer structure and dynamics. *The Journal of chemical physics*, 147(11):114902.
- [Peteu, 2007] Peteu, S. F. (2007). Responsive materials configured for micro-and nanoactuation. *Journal of intelligent material systems and structures*, 18(2):147–152.
- [Phillips et al., 2005] Phillips, J. C., Braun, R., Wang, W., Gumbart, J., Tajkhorshid, E., Villa, E., Chipot, C., Skeel, R. D., Kale, L., and Schulten, K. (2005). Scalable molecular dynamics with namd. *Journal of computational chemistry*, 26(16):1781–1802.
- [Phillips et al., 2012] Phillips, R., Theriot, J., Kondev, J., and Garcia, H. (2012). *Physical biology of the cell*. Garland Science.
- [Plascak et al., 2017] Plascak, J. A., Martins, P. H., and Bachmann, M. (2017). Solvent-dependent critical properties of polymer adsorption. *Physical Review E*, 95(5):050501.
- [Plimpton, 1995] Plimpton, S. (1995). Fast parallel algorithms for short-range molecular dynamics. *Journal of computational physics*, 117(1):1–19.
- [Purves et al., 2001] Purves, D., Augustine, G., Fitzpatrick, D., Katz, L., LaMantia, A., McNamara, J., and Williams, S. (2001). The organization of the nervous system. *Neuroscience. 2nd Edition. Sunderland, MA: Sinauer Associates Inc*, page 26.
- [Rajesh et al., 2002] Rajesh, R., Dhar, D., Giri, D., Kumar, S., and Singh, Y. (2002). Adsorption and collapse transitions in a linear polymer chain near an attractive wall. *Physical Review E*, 65(5):056124.
- [Rando and Chang, 2009] Rando, O. J. and Chang, H. Y. (2009). Genome-wide views of chromatin structure. *Annual review of biochemistry*, 78:245–271.

- [Reddy and Yethiraj, 2006] Reddy, G. and Yethiraj, A. (2006). Implicit and explicit solvent models for the simulation of dilute polymer solutions. *Macromolecules*, 39(24):8536–8542.
- [Reddy and Yethiraj, 2010] Reddy, G. and Yethiraj, A. (2010). Solvent effects in polyelectrolyte adsorption: computer simulations with explicit and implicit solvent. *The Journal of chemical physics*, 132(7):074903.
- [Reisner et al., 2007] Reisner, W., Beech, J. P., Larsen, N. B., Flyvbjerg, H., Kristensen, A., and Tegenfeldt, J. O. (2007). Nanoconfinement-enhanced conformational response of single dna molecules to changes in ionic environment. *Physical review letters*, 99(5):058302.
- [Reisner et al., 2005] Reisner, W., Morton, K. J., Riehn, R., Wang, Y. M., Yu, Z., Rosen, M., Sturm, J. C., Chou, S. Y., Frey, E., and Austin, R. H. (2005). Statics and dynamics of single dna molecules confined in nanochannels. *Physical Review Letters*, 94(19):196101.
- [Reisner et al., 2012] Reisner, W., Pedersen, J. N., and Austin, R. H. (2012). Dna confinement in nanochannels: physics and biological applications. *Reports on Progress in Physics*, 75(10):106601.
- [Ren et al., 2018] Ren, X., Das, R., Tran, P., Ngo, T. D., and Xie, Y. M. (2018). Auxetic metamaterials and structures: A review. *Smart materials and structures*, 27(2):023001.
- [Reznik and Landes, 2012] Reznik, C. and Landes, C. F. (2012). Transport in supported polyelectrolyte brushes. *Accounts of chemical research*, 45(11):1927–1935.
- [Richmond and Davey, 2003] Richmond, T. J. and Davey, C. A. (2003). The structure of dna in the nucleosome core. *Nature*, 423(6936):145.

- [Riehn et al., 2005] Riehn, R., Lu, M., Wang, Y.-M., Lim, S. F., Cox, E. C., and Austin, R. H. (2005). Restriction mapping in nanofluidic devices. *Proceedings of the National Academy of Sciences*, 102(29):10012–10016.
- [Rivera and Ren, 2013] Rivera, C. M. and Ren, B. (2013). Mapping human epigenomes. *Cell*, 155(1):39 – 55.
- [Ruggiero et al., 2018] Ruggiero, F., Aruta, R., Netti, P. A., and Torino, E. (2018). Confinement of a polymer chain: An entropic study by monte carlo method. *AIChE Journal*, 64(2):416–426.
- [Saitô et al., 1967] Saitô, N., Takahashi, K., and Yunoki, Y. (1967). The statistical mechanical theory of stiff chains. *Journal of the Physical Society of Japan*, 22(1):219–226.
- [Scalliet et al., 2015] Scalliet, C., Gnoli, A., Puglisi, A., and Vulpiani, A. (2015). Cages and anomalous diffusion in vibrated dense granular media. *Physical review letters*, 114(19):198001.
- [Schiessel, 2003] Schiessel, H. (2003). The physics of chromatin. *Journal of Physics: Condensed Matter*, 15(19):R699.
- [Schneider et al., 2016] Schneider, D., Mehlhorn, D., Zeigermann, P., Kärger, J., and Valiullin, R. (2016). Transport properties of hierarchical micro–mesoporous materials. *Chemical Society Reviews*, 45(12):3439–3467.
- [Shendruk et al., 2015] Shendruk, T. N., Bertrand, M., de Haan, H. W., Harden, J. L., and Slater, G. W. (2015). Simulating the entropic collapse of coarse-grained chromosomes. *Biophysical journal*, 108(4):810–820.
- [Shendruk et al., 2014] Shendruk, T. N., Bertrand, M., Harden, J. L., Slater, G. W., and de Haan, H. W. (2014). Coarse-grained molecular dynamics simulations of

- depletion-induced interactions for soft matter systems. *The Journal of chemical physics*, 141(24):244910.
- [Shin et al., 2015] Shin, J., Cherstvy, A. G., and Metzler, R. (2015). Kinetics of polymer looping with macromolecular crowding: effects of volume fraction and crowder size. *Soft matter*, 11(3):472–488.
- [Speyer and Pastorino, 2019] Speyer, K. and Pastorino, C. (2019). Pressure responsive gating in nanochannels coated by semiflexible polymer brushes. *Soft matter*, 15(5):937–946.
- [Strom et al., 2017] Strom, A. R., Emelyanov, A. V., Mir, M., Fyodorov, D. V., Darzacq, X., and Karpen, G. H. (2017). Phase separation drives heterochromatin domain formation. *Nature*, 547(7662):241.
- [Strulson et al., 2014] Strulson, C. A., Boyer, J. A., Whitman, E. E., and Bevilacqua, P. C. (2014). Molecular crowders and cosolutes promote folding cooperativity of rna under physiological ionic conditions. *RNA*.
- [Stukowski, 2010] Stukowski, A. (2010). Visualization and analysis of atomistic simulation data with OVITO-the Open Visualization Tool. *MODELLING AND SIMULATION IN MATERIALS SCIENCE AND ENGINEERING*, 18(1).
- [Suda et al., 1987] Suda, Y., Suzuki, M., Ikawa, Y., and Aizawa, S. (1987). Mouse embryonic stem cells exhibit indefinite proliferative potential. *Journal of cellular physiology*, 133(1):197–201.
- [Swift and Discher, 2014] Swift, J. and Discher, D. E. (2014). The nuclear lamina is mechano-responsive to ecm elasticity in mature tissue. *J Cell Sci*, 2014:jcs-149203.
- [Swift et al., 2013] Swift, J., Ivanovska, I. L., Buxboim, A., Harada, T., Dingal, P. D. P., Pinter, J., Pajerowski, J. D., Spinler, K. R., Shin, J.-W., Tewari, M., et al.

- (2013). Nuclear lamin-a scales with tissue stiffness and enhances matrix-directed differentiation. *Science*, 341(6149):1240104.
- [Swope et al., 1982] Swope, W. C., Andersen, H. C., Berens, P. H., and Wilson, K. R. (1982). A computer simulation method for the calculation of equilibrium constants for the formation of physical clusters of molecules: Application to small water clusters. *The Journal of chemical physics*, 76(1):637–649.
- [Takahashi and Yamanaka, 2006] Takahashi, K. and Yamanaka, S. (2006). Induction of pluripotent stem cells from mouse embryonic and adult fibroblast cultures by defined factors. *cell*, 126(4):663–676.
- [Talwar et al., 2013] Talwar, S., Kumar, A., Rao, M., Menon, G. I., and Shivashankar, G. (2013). Correlated spatio-temporal fluctuations in chromatin compaction states characterize stem cells. *Biophysical journal*, 104(3):553–564.
- [Tark-Dame et al., 2011] Tark-Dame, M., van Driel, R., and Heermann, D. W. (2011). Chromatin folding – from biology to polymer models and back. *Journal of Cell Science*, 124(6):839–845.
- [Tegenfeldt et al., 2004] Tegenfeldt, J. O., Prinz, C., Cao, H., Chou, S., Reisner, W. W., Riehn, R., Wang, Y. M., Cox, E. C., Sturm, J. C., Silberzan, P., et al. (2004). The dynamics of genomic-length dna molecules in 100-nm channels. *Proceedings of the National Academy of Sciences*, 101(30):10979–10983.
- [Thirumalai and Hyeon, 2005] Thirumalai, D. and Hyeon, C. (2005). Rna and protein folding: common themes and variations. *Biochemistry*, 44(13):4957–4970.
- [Tripathi and Menon, 2019] Tripathi, K. and Menon, G. I. (2019). Chromatin compaction, auxeticity, and the epigenetic landscape of stem cells. *Phys. Rev. X*, 9:041020.

- [Tripathi et al., 2019] Tripathi, K., Menon, G. I., and Vemparala, S. (2019). Confined crowded polymers near attractive surfaces. *The Journal of Chemical Physics*, 151(24):244901.
- [Ugarte et al., 2015] Ugarte, F., Sousae, R., Cinquin, B., Martin, E. W., Krietsch, J., Sanchez, G., Inman, M., Tsang, H., Warr, M., Passequé, E., et al. (2015). Progressive chromatin condensation and h3k9 methylation regulate the differentiation of embryonic and hematopoietic stem cells. *Stem cell reports*, 5(5):728–740.
- [Uversky et al., 2002] Uversky, V. N., Cooper, E. M., Bower, K. S., Li, J., and Fink, A. L. (2002). Accelerated α -synuclein fibrillation in crowded milieu. *FEBS letters*, 515(1-3):99–103.
- [van den Berg et al., 1999] van den Berg, B., Ellis, R. J., and Dobson, C. M. (1999). Effects of macromolecular crowding on protein folding and aggregation. *The EMBO journal*, 18(24):6927–6933.
- [Van Der Spoel et al., 2005] Van Der Spoel, D., Lindahl, E., Hess, B., Groenhof, G., Mark, A. E., and Berendsen, H. J. C. (2005). Gromacs: Fast, flexible, and free. *Journal of Computational Chemistry*, 26(16):1701–1718.
- [Van Holde and Zlatanova, 1996] Van Holde, K. and Zlatanova, J. (1996). What determines the folding of the chromatin fiber? *Proceedings of the National Academy of Sciences*, 93(20):10548–10555.
- [Vasilevskaya et al., 1995] Vasilevskaya, V., Khokhlov, A., Matsuzawa, Y., and Yoshikawa, K. (1995). Collapse of single dna molecule in poly (ethylene glycol) solutions. *The Journal of chemical physics*, 102(16):6595–6602.
- [Verlet, 1967] Verlet, L. (1967). Computer" experiments" on classical fluids. i. thermodynamical properties of lennard-jones molecules. *Physical review*, 159(1):98.

- [Vogt, 2018] Vogt, B. D. (2018). Mechanical and viscoelastic properties of confined amorphous polymers. *Journal of Polymer Science Part B: Polymer Physics*, 56(1):9–30.
- [Waddington, 1947] Waddington, C. H. (1947). *Organisers and genes*. University Press; Cambridge.
- [Waddington, 2014] Waddington, C. H. (2014). *The strategy of the genes*, volume 20. Routledge.
- [Wang et al., 1994] Wang, B.-C., Rose, J., Arents, G., and Moudrianakis, E. (1994). The octameric histone core of the nucleosome: structural issues resolved. *Journal of molecular biology*, 236(1):179–188.
- [Wang et al., 2019] Wang, D., Wu, H., Liu, L., Chen, J., and Schwartz, D. K. (2019). Diffusive escape of a nanoparticle from a porous cavity. *Physical Review Letters*, 123(11):118002.
- [Whitaker, 1986] Whitaker, S. (1986). Flow in porous media i: A theoretical derivation of darcy’s law. *Transport in porous media*, 1(1):3–25.
- [Yamamoto and Schiessel, 2017] Yamamoto, T. and Schiessel, H. (2017). Chromatin gels are auxetic due to cooperative nucleosome assembly and disassembly dynamics. *EPL (Europhysics Letters)*, 118(2):28003.
- [Yang et al., 2015] Yang, N., Chen, X., Ren, T., Zhang, P., and Yang, D. (2015). Carbon nanotube based biosensors. *Sensors and Actuators B: Chemical*, 207:690–715.
- [Yim and Sheetz, 2012] Yim, E. K. and Sheetz, M. P. (2012). Force-dependent cell signaling in stem cell differentiation. *Stem cell research & therapy*, 3(5):41.
- [Young, 2011] Young, R. A. (2011). Control of the embryonic stem cell state. *Cell*, 144(6):940–954.

- [Yu et al., 2003] Yu, C., Mutlu, S., Selvaganapathy, P., Mastrangelo, C. H., Svec, F., and Fréchet, J. M. (2003). Flow control valves for analytical microfluidic chips without mechanical parts based on thermally responsive monolithic polymers. *Analytical Chemistry*, 75(8):1958–1961.
- [Zhang and Müller, 2005] Zhang, M. and Müller, A. H. (2005). Cylindrical polymer brushes. *Journal of Polymer Science Part A: Polymer Chemistry*, 43(16):3461–3481.
- [Zhou, 2013] Zhou, H.-X. (2013). Influence of crowded cellular environments on protein folding, binding, and oligomerization: biological consequences and potentials of atomistic modeling. *FEBS letters*, 587(8):1053–1061.
- [Zhou et al., 2008] Zhou, H.-X., Rivas, G., and Minton, A. P. (2008). Macromolecular crowding and confinement: biochemical, biophysical, and potential physiological consequences. *Annu. Rev. Biophys.*, 37:375–397.
- [Zimmerman and Minton, 1993] Zimmerman, S. B. and Minton, A. P. (1993). Macromolecular crowding: biochemical, biophysical, and physiological consequences. *Annual review of biophysics and biomolecular structure*, 22(1):27–65.
- [Zuo et al., 2017] Zuo, Y., Wang, G., Yu, Y., Zuo, C., Shi, L., Shi, F., and Wei, J. (2017). Smart nanovalves with thermoresponsive amphiphilic triblock copolymer brushes. *Journal of Macromolecular Science, Part B*, 56(1):26–38.